FLEXIBLE PIEZOELECTRIC COMPOSITES AND CONCEPTS FOR BIO-INSPIRED DYNAMIC BENDING-TWISTING ACTUATION

A Thesis
Presented to
The Academic Faculty

by

Algan Samur

In Partial Fulfillment
of the Requirements for the Degree
Master of Science in the
School of Mechanical Engineering

Georgia Institute of Technology
May 2013

FLEXIBLE PIEZOELECTRIC COMPOSITES AND CONCEPTS FOR BIO-INSPIRED DYNAMIC BENDING-TWISTING ACTUATION

Approved by:

Dr. Alper Erturk, Advisor
School of Mechanical Engineering
Georgia Institute of Technology

Dr. Aldo A. Ferri
School of Mechanical Engineering
Georgia Institute of Technology

Dr. Alexander Alexeev
School of Mechanical Engineering
Georgia Institute of Technology

Date Approved: March 25th, 2013

ACKNOWLEDGEMENTS

I would like to express my great appreciation to my advisor, Dr. Alper Erturk for his guidance and assistance to this research project. I would like to thank Dr. Aldo A. Ferri, and Dr. Alexander Alexeev for serving on my thesis committee and providing me valuable feedback. I wish to acknowledge my colleagues from Smart Structures and Dynamical Systems Laboratory for the great atmosphere, support, and friendship.

I would like to extend my special thanks to the Fulbright Program for funding my academic program. The Fulbright Program is funded by the Department of State.

TABLE OF CONTENTS

ACKNOWLEDGEMENTS ..... **III**

LIST OF TABLES ..... **VII**

LIST OF FIGURES ..... **VIII**

SUMMARY ..... **XV**

CHAPTER 1

INTRODUCTION **1**

1.1 Motivation 1

1.2 Research objectives 4

1.3 Outline of thesis 5

CHAPTER 2

BACKGROUND AND SIGNIFICANCE **7**

2.1 Recent literature on bio-inspired aerial vehicles using smart materials 7

2.2 Recent literature on bio-inspired aquatic vehicles using smart materials 14

2.3 Significance of the current research 18

CHAPTER 3

ASYMMETRIC BIMORPH WITH WIDE 0°/45°-FIBER LAMINATES **21**

3.1 Asymmetric bimorph with wide 0°/45°-fiber laminates 21

3.2 Experimental setup and measurement procedure 23

3.3 Linear modeling of the asymmetric bimorph for low-voltage actuation 24

3.4 Stiffness identification for the asymmetric bimorph 32

3.5 High voltage characterization of the asymmetric bimorph and nonlinear response34

CHAPTER 4

DOUBLE BIMORPH WITH NARROW 0°-FIBER LAMINATES..... 46

4.1 Double bimorph with narrow 0°-fiber laminates..... 46

4.2 Linear modeling of the double bimorph for low-voltage actuation..... 47

4.3 Stiffness identification for the double bimorph 52

4.4 Active stiffness change 54

4.5 High-voltage characterization of the double bimorph and nonlinear response 59

CHAPTER 5

WIND TUNNEL EXPERIMENTS FOR BENDING-TWISTING COUPLING OF A FLEXIBLE DOUBLE BIMORPH..... 68

5.1 Structural properties of the flexible double bimorph..... 68

5.2 Experimental setup and measurements..... 69

5.3 High-voltage characterization of the nonlinear behavior 70

5.4 Wind tunnel experiments under dynamic actuation 76

CHAPTER 6

TRIPLE BIMORPH AND AQUATIC THRUST GENERATION..... 82

6.1 Triple bimorph caudal fin with narrow 0°-fiber laminates..... 82

6.2 Details of the experimental setup..... 83

6.3 Calibration for thrust measurement 84

6.4 Actuation cases: flat, cup, and rolling..... 86

6.5 Velocity and phase histories for different actuation cases 87

6.6 Thrust generation and power consumption 97

CHAPTER 7

POWER CONSUMPTION LEVELS AND ENERGY HARVESTING EXPERIMENTS 100

7.1 Power consumption in combined dynamic actuation 100

7.2 Energy harvesting from ambient vibrations 102

7.3 Solar energy harvesting using flexible solar films 105

CHAPTER 8

CONCLUSIONS AND RECOMMENDATIONS FOR FUTURE WORK 109

8.1 Conclusions 109

8.2 Recommendations for future work 111

REFERENCES 115

LIST OF TABLES

Table 1. Maximum flapping and twist angle results observed during actuation of the asymmetric bimorph. 44

Table 2. Maximum flapping and twist angle results observed during actuation of the double bimorph. 66

Table 3. Maximum flapping and twist angle (peak-to-peak) results observed during the actuation of the DB-FRS..... 76

Table 4. Voltage and phase levels for the different actuation cases applied to the TBPCF 86

Table 5. Numerical values of the velocity and phase responses at the resonant frequencies of the first and second modes observed during each of the actuation cases 95

LIST OF FIGURES

Figure 1. (a) Schematic of the MFC structure and (b) a picture from the manufacturer (Smart Material Corp.) demonstrating its flexibility. 2

Figure 2. Variable camber morphing wing actuated by MFCs [12] (Reused with permission). 7

Figure 3. Unmanned aerial vehicle with morphing wings actuated by post-buckled precompressed piezoelectric bender actuators [14] (Reused with permission). 8

Figure 4. Morphing wing with multiple MFCs: (a) core of the wing presenting MFCs (b) static loading tests on the morphing wing [15] (Reused with permission). 9

Figure 5. Electro-bonded laminates for variable stiffness applications: (a) off-state for compliant behavior and (b) on-state for stiffer behavior [40] (Reused with permission). 10

Figure 6. Micro air vehicle that uses piezoelectric bimorph cantilever as actuator [45] (Reused with permission, © 2007 IEEE). 11

Figure 7. A flapping wing design with insect inspired ring shaped driving module actuated by MFC [46] (Reused with permission, © 2010 IEEE). 11

Figure 8. An MFC actuated UAV design with a span of 297 mm [18] (Reused with permission, © 2008 IEEE). 12

Figure 9. A flapping wing design that does both flapping and twisting motions [17] (Reused with permission, © 2006 IEEE). 13

Figure 10. Hummingbird wing motion relative to its body at different flight speeds varying from 0 to 12 m/s [47] (Reused with permission). 14

Figure 11. An IPMC actuated robotic fish with a passive caudal fin [52] (Reused with permission, © 2008 IEEE). 15

Figure 12. A robotic fish actuated by lightweight piezo-composite actuators (LIPCAs) (a) overall view (b) actuation mechanism [34] (Reused with permission). 16

Figure 13. Pictures of an untethered MFC-based piezoelectric swimmer [60] (Reused with permission) showing the (a) side view and (b) top view for combined turning motion. 17

Figure 14. Motion of the caudal fin observed in biological fish [39] (Reused with permission)..... 18

Figure 15. Asymmetric bimorph architecture with wide 0°/45° MFC laminates: (a) top laminate (0° fibers) and (b) bottom laminate (45° fibers) along with the tip velocity measurement points (A, B, and C). The samples are clamped at the left end of the view. The schematics from the manufacturer (Smart Material Corp.) display the interdigitated electrode fingers which are perpendicular to the fibers. 22

Figure 16. Vacuum bonding process setup showing the vacuum pump and the curing setup in a sealed plastic bag. 23

Figure 17. Experimental setup with a close up view of 0°/45° asymmetrically laminated MFC flapping cantilever and its aluminum fixture to realize clamped-free boundary conditions. 24

Figure 18. Schematic of 0°/45°-fiber asymmetrically laminated wide bimorph cantilever showing each degree of freedom along with the actuation voltage variables..... 25

Figure 19. Peak-to-peak displacement response of the asymmetric bimorph measured at (a) point A, α_{11}, and (b) point C, α_{21}, due to the actuation of 0°-fiber laminate. 30

Figure 20. Peak-to-peak displacement response of the asymmetric bimorph measured at (a) point A, α_{12}, and (b) point C, α_{22}, due to the actuation of 45°-fiber laminate..... 31

Figure 21. Peak-to-peak displacement response of the asymmetric bimorph measured at (a) point A, and (b) point C due to out-of-phase combined actuation of 0° and 45°-fiber laminates. 32

Figure 22. Experimental data of deflection versus different cases of loading for determining the flexibility matrix of the 0°/45° asymmetrically laminated MFC flapping cantilever. (Solid lines are curve fit to the average of experimental data related to diagonal and off-diagonal terms of the flexibility matrix)..... 33

Figure 23. Peak-to-peak tip velocity frequency response curves measured at (a) point A, (b) point B, and (c) point C for actuation with different peak-to-peak voltage input levels using the 45° MFC laminate (forward frequency sweep). 36

Figure 24. Peak-to-peak tip velocity frequency response curves measured at (a) point A, (b) point B, and (c) point C for actuation with different peak-to-peak voltage input levels using the 0° MFC laminate (forward frequency sweep). 38

Figure 25. Resonant peak-to-peak displacement values for the bending and twist modes measured at points A, B, and C due to actuation using the (a) 45° and (b) 0° MFC laminates (solid lines are curve fit). 40

Figure 26. Peak-to-peak tip velocity frequency response curves measured at (a) point A, (b) point B, and (c) point C for combined actuation of the asymmetric bimorph with different peak-to-peak voltage input levels (forward frequency sweep). The top (0° MFC) and the bottom (45° MFC) laminates are actuated simultaneously 180° out of phase. 42

Figure 27. Comparison of combined (45° and 0° laminates out of phase simultaneously) and separate (45° laminate and 0° laminate separately) actuation cases with a focus on the peak-to-peak velocity response at point A for a peak-to-peak voltage input of 600 V (forward frequency sweep). 43

Figure 28. Resonant peak-to-peak displacement values for the bending and twist modes measured at points A, B, and C due to combined actuation of the asymmetric bimorph (solid lines are curve fit). 43

Figure 29. Frequency response curves of current consumption amplitude for different peak-to-peak voltage levels due to combined actuation of the asymmetric bimorph (forward frequency sweep). 44

Figure 30. Double bimorph architecture with narrow 0° MFC laminates and solar film substrate: (a) top view and (b) bottom view along with the tip velocity measurement points and labeling detail of the four laminates (top laminates: (1) and (2); bottom laminates: (3) and (4)). The samples are clamped at the left end of the view. 47

Figure 31. Schematic of the double bimorph architecture showing each degree of freedom along with the actuation voltage variables. 48

Figure 32. Peak-to-peak displacement response of the double bimorph measured at (a) point A, α_{11}, and (b) point C, α_{21} due to the actuation of (1) and (4) (Fig. 31) laminates out of phase. 50

Figure 33. Peak-to-peak displacement response of the double bimorph measured at (a) point A, α_{12}, and (b) point C, α_{22} due to the actuation of (2) and (3) (Fig. 31) laminates out of phase. 51

Figure 34. Peak-to-peak displacement response of the double bimorph measured at (a) point A, and (b) point C due to pure bending actuation case. 52

Figure 35. Peak-to-peak displacement response of the double bimorph measured at (a) point A, and (b) point C due to pure twist actuation case. 52

Figure 36. Experimental data of deflection versus different cases of loading for determining the flexibility matrix of the double bimorph cantilever. (Solid lines are curve fit to the average of experimental data related to diagonal and off-diagonal terms of the flexibility matrix). 53

Figure 37. Experimental setup for measuring stiffness variation due to different DC voltage input to the double bimorph structure. 55

Figure 38. Tip velocity – to – base acceleration FRFs for each level of DC voltage input to the double bimorph to change the stiffness. (Solid lines are model results) 57

Figure 39. Percentage change in bending stiffness of the double bimorph for varying DC voltage input..... 58

Figure 40. Extracted damping ratio values of the double bimorph for each level of DC voltage input..... 59

Figure 41. Peak-to-peak tip velocity frequency response curves measured at point B for pure bending actuation of the double bimorph (forward frequency sweep). The laminate pairs 1-2 (top) and 3-4 (bottom) in Fig. 30 are actuated 180° out of phase to create pure bending..... 60

Figure 42. Resonant peak-to-peak displacement values for the bending mode measured at point B due to pure bending actuation of the double bimorph including the actuation range with positive DC offset for increased actuation voltage without depolarization (solid lines are curve fit). 61

Figure 43. Peak-to-peak tip velocity frequency response curves measured at (a) point A, (b) point B, and (c) point C for pure twist actuation of the double bimorph (forward frequency sweep). The cross laminate pairs 1-3 and 2-4 in Fig. 30 are actuated 180° out of phase to create pure twist..... 62

Figure 44. Resonant peak-to-peak displacement values for the twist mode measured at points A, B, and C due to pure twist actuation of the double bimorph (solid lines are curve fit)..... 63

Figure 45. Peak-to-peak tip velocity frequency response curves measured at (a) point A, (b) point B, and (c) point C for combined actuation of the double bimorph with different peak-to-peak voltage input levels (forward frequency sweep). The MFCs 2, 3, and 4 are in phase while the MFC 1 is 180° out of phase during the simultaneous actuation. 64

Figure 46. Resonant peak-to-peak displacement values for the bending and twist modes measured at points A, B, and C due to combined actuation of the double bimorph (solid lines are curve fit). 65

Figure 47. Frequency response curves of current amplitude for different peak-to-peak voltage levels due to combined actuation of the double bimorph (forward frequency sweep). 65

Figure 48. The double bimorph with flexible rubber substrate: (a) top view along with the measurement points and labels for MFCs (b) bottom view showing the labels for MFCs (c) isometric view. 69

Figure 49. Experimental setup for wind tunnel experiments: (a) general view (b) close up view presenting the test section and wind speed direction. 70

Figure 50. Peak-to-peak tip velocity frequency response curves measured at (a) point A (b) point B for the pure bending actuation case of DB-FRS (forward frequency sweep). 71

Figure 51. Resonant peak-to-peak displacement values for the bending mode measured at points A and B due to pure bending actuation case of DB-FRS (solid lines are curve fit). 71

Figure 52. Peak-to-peak tip velocity frequency response curves measured at (a) point A and (b) point B for the pure twist actuation case of DB-FRS (forward frequency sweep). 72

Figure 53. Resonant peak-to-peak displacement values for the twist mode measured at points A and B for the pure twist actuation case of DB-FRS (solid lines are curve fit)... 73

Figure 54. Peak-to-peak tip velocity frequency response curves measured at (a) point A and (b) point B for the combined actuation case of DB-FRS (forward frequency sweep). 73

Figure 55. Resonant peak-to-peak displacement values for the bending and twist modes measured at the points A and B due to combined actuation case of DB-FRS (solid lines are curve fit). 74

Figure 56. Frequency response curves of current consumption amplitude for different peak-to-peak voltage levels due to combined actuation case of DB-FRS (forward frequency sweep). 75

Figure 57. Wind tunnel tests on DB-FRS for pure bending actuation case with peak-to-peak input voltage levels of (a) 200 V, (b) 400 V, (c) 600 V, and (d) 800 V (the first column refers to the measurements at point A, leading edge; and the second column refers to the measurements at point B, trailing edge). 78

Figure 58. Wind tunnel tests on DB-FRS for the twisting actuation case with peak-to-peak input voltage levels of (a) 200 V, (b) 400 V, (c) 600 V, and (d) 800 V, (the first column refers to the measurements at point A, leading edge; and the second column refers to the measurements at point B, trailing edge). 80

Figure 59. Wind tunnel tests on DB-FRS for the combined actuation case with peak-to-peak input voltage levels of (a) 200 V, (b) 400 V, (c) 600 V, and (d) 800 V (the first column refers to the measurements at point A, leading edge; and the second column refers to the measurements at point B, trailing edge). 81

Figure 60. (a) Isometric view and (b) side view (all dimensions are in mm) of the 3-D TBPCF model composed of 3 narrow MFC bimorphs sharing a rubber substrate; (c) picture of the fabricated TBPCF and its clamp along with the tip velocity measurement points (A, B, and C). 83

Figure 61. (a) Overview of the experimental setup: (1) laser vibrometer and (2) its displacement decoder used for thrust measurement, (3) laser vibrometers used for vibration of points A, B, and C (see Fig. 60c) on the TBPCF, (4) signal generation and data acquisition system, (5) high-voltage amplifiers, and (6) water tank; (b) close-up view of the water tank showing the thrust measurement point and the corresponding mirror to reflect the laser beam; (c) close-up view of the water tank showing velocity measurement points and mirrors used to reflect the laser beams. 84

Figure 62. Calibration of the thrust measurement system (a) experimental setup used for determining the stiffness of the cantilever beam for thrust measurement; (b) close-up view showing the point of applied force and the point of deflection; (c) calibration line showing the applied force versus deflection of the horizontal cantilever beam. 85

Figure 63. Underwater actuation experiments: (a) side view of the TBPCF showing labels for each bimorph; (b) schematics describing the actuation cases (rear view) for the intended motion patterns. 87

Figure 64. TBPCF dynamics under actuation case 1: (a) velocity frequency response of bimorphs A, B, and C; (b) mean thrust frequency response; (c) simultaneous velocity histories at the resonant frequency. 88

Figure 65. TBPCF dynamics under actuation case 2: (a) velocity frequency response of bimorphs A, B, and C; (b) mean thrust frequency response; (c) simultaneous velocity histories at the resonant frequencies. 90

Figure 66. TBPCF dynamics under actuation case 3: (a) velocity frequency response of bimorphs A, B, and C; (b) mean thrust frequency response; (c) simultaneous velocity histories at the resonant frequencies. 91

Figure 67. TBPCF dynamics under actuation case 4: (a) velocity frequency response of bimorphs A, B, and C; (b) mean thrust frequency response; (c) simultaneous velocity histories at the resonant frequencies. 92

Figure 68. TBPCF dynamics under actuation case 5: (a) velocity frequency response of bimorphs A, B, and C; (b) mean thrust frequency response; (c) simultaneous velocity histories at the resonant frequencies. 93

Figure 69. TBPCF dynamics under actuation case 6: (a) velocity frequency response of bimorphs A, B, and C; (b) mean thrust frequency response; (c) simultaneous velocity histories at the resonant frequencies. 94

Figure 70. Measured simultaneous displacements of points A, B, and C in different actuation cases. 96

Figure 71. Comparison of real power consumption by TBPCF for different actuation cases. 97

Figure 72. Comparison of mean thrust generated by TBPCF for different actuation cases. 98

Figure 73. Comparison of mean thrust output per power input of TBPCF for different actuation cases. 99

Figure 74. Average power consumption levels per active area of the composite architectures in combined actuation case at (a) bending mode resonant frequencies and (b) twist mode resonant frequencies (Solid lines are curve fit). 101

Figure 75. Experimental setup for characterizing the energy harvesting performance of the piezo-composite architectures. 102

Figure 76. Voltage – to – base acceleration FRFs of the (a) asymmetric bimorph (b) DB-SFS (c) DB-FRS for different levels of external load resistance ranging from short to open circuit conditions. 104

Figure 77. Power outputs (per base acceleration) of the composite architectures versus resistance. 105

Figure 78. Experimental setup employed for solar energy harvesting measurements using flexible solar films. 106

Figure 79. Solar power extracted from 8760 mm^2 solar film area versus resistance for different levels of solar irradiance (solid lines are curve fit). 107

Figure 80. Power per flexible solar film area produced for the optimal resistance value versus solar irradiance. 107

Figure 81. Velocity FRFs per actuation voltage of (a) double bimorph with solar film substrate under pure bending actuation case (at measurement point B), (b) double bimorph with solar film substrate under pure twisting actuation case (at measurement point A), and (c) asymmetric bimorph under combined actuation case (at measurement point A). 113

SUMMARY

This work investigates the use of active structures made of flexible Macro-Fiber Composite (MFC) piezoelectric materials for bio-inspired bending-twisting actuation. The focus is placed on different piezoelectric composite architectures for potential flapping-wing flight and fish-like swimming applications. The flapping-wing concept can be more advantageous than the stationary-wing counterpart in terms of higher maneuverability and agility in thrust and lift generation. Analogous to flapping-wing flight, recent research by experimental biologists has revealed that fish caudal fin incorporates complex motion patterns to adjust thrust and lift. The MFC-based architectures studied in this work are an Asymmetric Bimorph (AB) with 0°/45°-fiber laminates, a Double Bimorph (DB) with narrow 0°-fiber laminates (for flapping-wing applications), and a Triple Bimorph (TB) with narrow 0°-fiber laminates to mimic a three degree-of-freedom (DOF) bio-inspired caudal fin (for aquatic robotics). The AB architecture includes two wide MFC laminates with different fiber orientation while the DB architecture has four narrow MFC laminates forming two bimorphs sharing the same substrate with a chord-wise distance. Since flapping by pure bending is a symmetric motion, positive lift and thrust resultants can be produced by asymmetric bending-twisting coupling as well as asymmetric actuation signals. For the AB and DB architectures, a 2-DOF model is employed for representing the linear vibratory response. For the nonlinear region under high actuation voltage levels, the electroelastic dynamics of these two architectures are experimentally characterized with a focus on their frequency response curves covering the fundamental bending and twisting modes. The

power consumption levels are also recorded for each configuration, and solar energy harvesting using flexible films with dimensions similar to the AB and DB architectures is investigated toward the self-powered flapping-wing concept. Desktop wind tunnel tests are performed for further exploration of bending-twisting coupling in the presence of air flow. In addition to studying the actuation capabilities, both architectures are tested for energy harvesting under base excitation since power supply is important for unmanned aerial vehicles. Additionally, the DB architecture is studied for active stiffness change without shape change under static actuation. The TB architecture representing a 3-DOF caudal fin is studied specifically for underwater robotic fish applications. Various actuation patterns are applied with amplitude and phase differences to create flat, cupping, and rolling motions. Thrust production, velocity response, and power consumption levels are recorded for a range of actuation frequencies in an effort to identify the most efficient case.

CHAPTER 1

INTRODUCTION

1.1 Motivation

Piezoelectric actuators offer high potential to be exploited in bio-inspired aerial and underwater vehicles due to their scalable, noiseless and energy efficient characteristics for low power applications (<30W) as compared to other alternatives, such as electromagnetic actuators [1]. Various types of piezoelectric actuators ranging from stack configurations to disks have been available off the shelf for the past few decades. Although conventional piezoelectric actuators can provide large forces, they offer limited deformation, which is not suitable for bio-inspired systems unless the actuator is combined with a displacement magnifier mechanism.

The Macro-Fiber Composite (MFC) piezoelectric technology developed at the NASA Langley Research Center [2, 3] in the last decade is a light-weight piezoelectric composite that consists of piezoelectric fibers (employing the effective 33-mode of piezoelectricity), interdigitated electrodes, epoxy, and Kapton layers (Fig. 1). Over the last decade, MFCs have been researched for various applications including sensing [4, 5], energy harvesting [6], actuation [7, 8], and vibration control [9]. In addition to the inherent advantages that comes with the piezoelectric actuators, MFC technology provides high strain and stress performance, flexibility, endurance and they are manufactured in various sizes [2]. Therefore MFC actuators can be effectively employed for bio-inspired aerial and aquatic structure applications.

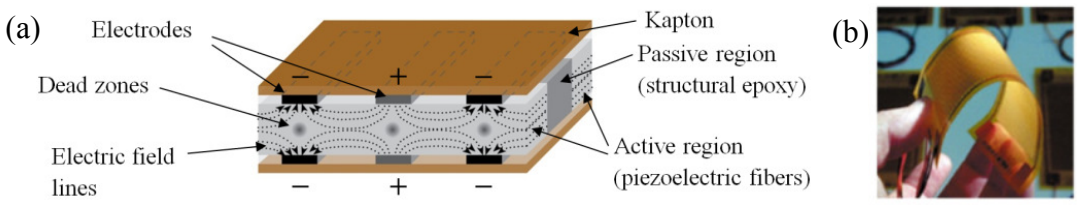

Figure 1. (a) Schematic of the MFC structure and (b) a picture from the manufacturer (Smart Material Corp.) demonstrating its flexibility.

Bio-inspired unmanned aerial vehicles (UAV) exploiting electroactive materials have received growing interest in the last few years. Morphing-wing [10] and flapping-wing [11] UAVs have been widely researched since they offer enhanced adaptive performance for different flight conditions as compared to conventional UAVs with stationary wings. Morphing-wing aircraft (based on static/quasistatic change of wing structure) maximizes efficiency by changing angle of attack, lift and drag coefficients for possible different conditions during the flight. Flapping-wing aircraft, on the other hand, offers higher maneuverability and agility. Recently, researchers applied MFC piezoelectric laminates to morphing-wing and flapping-wing UAVs. Employing MFCs for morphing-wing applications have been proven to be fairly successful [12-16]; however, research on using MFCs for flapping-wing aircraft [17-19] has been rather limited and requires further effort for performance enhancement toward successful results. In particular, further research is needed to exploit the combination of bending and twisting motions as well as asymmetric actuation. Improved and independent actuation authority over bending and twisting motions might potentially enhance the asymmetry of flapping toward increasing the lift and thrust resultants. Additionally, recent research has also investigated varying-stiffness wings to improve energy efficiency [20] in morphing-

wing UAVs. Properly combined MFCs can also serve to alter the stiffness with/without shape change. Another advantage of using the MFC technology in UAVs is the direct piezoelectric effect to harvest ambient vibrational energy [21-23] with the same interface to power small electronic components of the aircraft.

Bio-inspired underwater vehicles have also received growing interest over the last few years. As an alternative to conventional underwater vehicles with propeller-based propulsion systems, the motivation for using bio-inspired structures in aquatic locomotion is to enable enhanced low-speed maneuverability, silent operation, signature reduction, lower weight, and reduced power consumption [24]. Fish-like locomotion can be embedded into underwater vehicles to be used in the surveillance and exploration of the ocean for military purposes or sustainable ecology [24-26]. In addition to commonly used smart material actuators for the locomotion of bio-inspired underwater vehicles, which are ionic polymer metal composite (IPMC), shape memory alloy (SMA) and lead zirconate titanate (PZT) [26], MFC actuators can be successfully utilized as well. Although most of the research on this area include locomotion by applying undulatory or oscillatory motion at the tail with or without an attached passive caudal fin [27-36], biological investigation on bluegill sunfish has revealed that caudal fin is actively controlled, and it incorporates many different motions for different swimming regimes [37-39]. Therefore, developing an MFC actuated caudal fin that is capable of morphing based on bio-inspired motions might improve the efficiency and maneuverability of locomotion.

1.2 Research objectives

The objective of this research is to investigate various flexible piezoelectric structure architectures and concepts exploiting bending-twisting motions under dynamic actuation for bio-inspired aerial and underwater locomotion applications. Further objectives are also to explore the potential of energy harvesting and active stiffness change capabilities. To this end, the goals in this thesis can be summarized as follows:

- Establishment of alternative laminated piezoelectric composite architectures (namely the asymmetric bimorph and double bimorph configurations) for independent/combined bending-twisting motions using flexible MFC actuators;
- Descriptive lumped-parameter electromechanical modeling of these configurations under low-voltage actuation with a focus on independent/combined bending-twisting motions;
- Experimental characterization of dynamic electroeleastic response of the proposed composite architectures to create pure bending, pure twisting, and combined bending-twisting motions under high-voltage actuation;
- Exploring the effect of the wind speed on the electroeleastic response of the flexible double bimorph configuration for coupling of bending and twisting modes with increasing flow speed;
- Investigating power consumption levels of the established configurations, and comparing these with the energy harvesting opportunities by using ambient vibrations through direct piezoelectric effect and solar energy via flexible structural solar films of similar dimensions;

- Investigating the capacity of adaptive stiffness change without a shape change by static actuation;
- Establishing a triple bimorph caudal fin to form complex dynamic bending-twisting motions as in biological fish and comparing various fin motions in terms of hydrodynamic thrust generation and actuation power consumption.

1.3 Outline of thesis

Following a literature review, throughout the following chapters, three piezoelectric composite architectures are investigated in detail: (1) an Asymmetric Bimorph (AB) with 0°/45°-fiber laminates, (2) a Double Bimorph (DB) with narrow 0°-fiber laminates (for flapping-wing applications), and (3) a Triple Bimorph (TB) with narrow 0°-fiber laminates (for aquatic robotics). Chapter 2 provides background on recent unmanned aerial vehicle and unmanned underwater vehicle research using smart actuators along with significance of the present research. Chapter 3 investigates the experimental characterization of dynamic electroelastic behavior of the first bending-twisting architecture in this study, the asymmetric bimorph. Chapter 4 is focused on the second bending-twisting architecture, namely the double bimorph, by providing characterization of the dynamic electroelastic response and active stiffness change capacity. Chapter 5 investigates the effect of wind speed on the dynamic electroelastic behavior of a flexible double bimorph for coupling of bending and twisting modes. In Chapter 6, a novel bio-inspired caudal fin (the triple bimorph) is introduced, and its hydrodynamic thrust generation capacity is studied under different actuation cases. Chapter 7 compares the power consumption levels of the flexible piezoelectric composite architectures explored in this thesis as well as the energy harvesting opportunities from

vibrations and solar insolation. Chapter 8 draws conclusions from this thesis research and presents recommendations for future work.

CHAPTER 2

BACKGROUND AND SIGNIFICANCE

2.1 Recent literature on bio-inspired aerial vehicles using smart materials

This section reviews the recent efforts on bio-inspired aerial vehicles using smart materials with an emphasis on piezoelectric transduction. Researchers have investigated the use of piezoelectric actuators on morphing wings. Kim and Han [12] showed lift can be increased by 20 % via camber variation at the morphing wing actuated by MFCs (Fig. 2). Kim et al. [13] made wind tunnel tests on MFC-actuated variable camber and reported an increase in the lift coefficient up to 24.4 % and 20.8 % for their static and dynamic tests, respectively. They managed to change the camber of the wing from -2.6 % to 4.4 % of the maximum chord length.

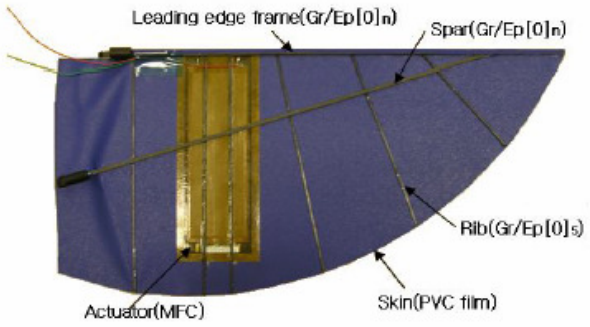

Figure 2. Variable camber morphing wing actuated by MFCs [12] (Reused with permission).

Vos et al. [14] suggested that using post-buckled pre-compressed piezoelectric bender actuators on the unmanned aerial vehicle presented in Fig. 3, instead of conventional servo-actuated ailerons increased the roll control authority by 38 %, reduced

the power required from 24 W to 100 mW, and reduced the actuator weight from 59g to only 3g.

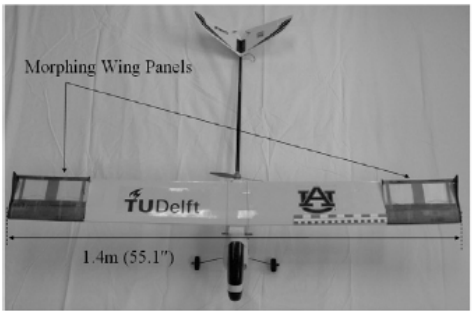

Figure 3. Unmanned aerial vehicle with morphing wings actuated by post-buckled precompressed piezoelectric bender actuators [14] (Reused with permission).

Paradies and Ciresa [15] tested the reliability of MFC actuation by both static and dynamic tests. They used multiple MFCs on the wing presented in Fig. 4a, and they measured a 4.35 mm displacement on the trailing edge due to MFC actuation although a load of 1.2 kg was placed on the trailing edge (Fig. 4b). They dynamically tested the wing under airflow with a speed of 10 m/s. At peak voltage of 1.5 kV, the wing gave a 0.17 Nm roll moment which was sufficient for a planned UAV. Bilgen et al. [16] worked on the effects of changing camber by using a bimorph MFC actuator with a thickness that is 1.0 % of the chord length where the camber was varied from -5.67% to 4.71% with changing voltage. A broad range of lift-to-drag ratio (from -17.3 to 17.8) was realized.

(a) 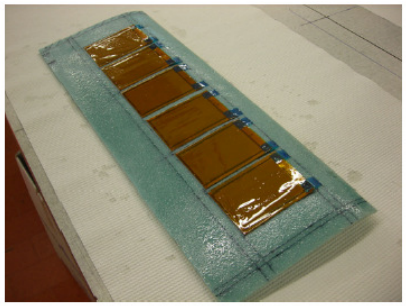 (b) 

Figure 4. Morphing wing with multiple MFCs: (a) core of the wing presenting MFCs (b) static loading tests on the morphing wing [15] (Reused with permission).

Additionally, active stiffness change have been suggested to improve energy efficiency in morphing wing applications [20]. Although high stiffness is favorable during most of the operational conditions, adapting to lower stiffness at the time of morphing would ease the morphing process thus improving energy efficiency. Electro-bonded laminates were investigated in [40, 41] for active stiffness change applications. At the off-state (Fig. 5a), when there is no electric field applied, coulomb attraction between the laminates vanishes causing the material to be compliant. In contrast, for the on state (Fig. 5b), the polymer layers are polarized which causes Maxwell stress to occur between the laminates along the thickness direction so that the material become stiffer. Another way of active stiffness change is presented by Raither et al [42]. They built a composite which includes elastomers (Soundcoat Dyad 609) as adaptive layers sandwiched between the carbon fiber reinforced polymer laminates. Exploiting the change in elastic modulus due to temperature variation, they modified the internal shear stress transfer which changed the stiffness of the material. The MFC technology can be used for active stiffness change as well because MFC actuators provide high stresses due to static actuation (DC voltage).

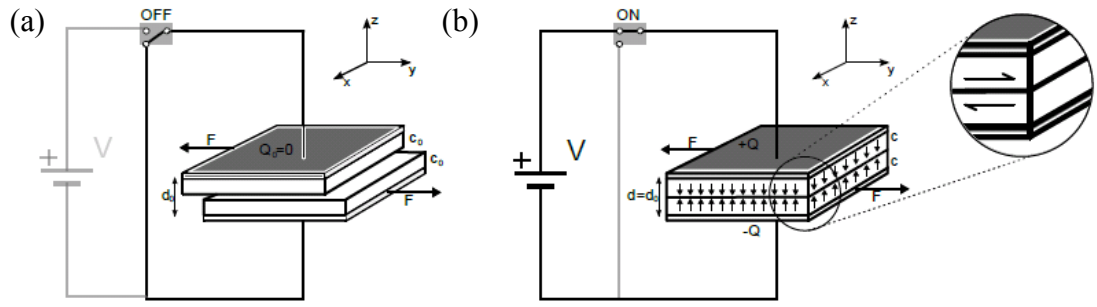

Figure 5. Electro-bonded laminates for variable stiffness applications: (a) off-state for compliant behavior and (b) on-state for stiffer behavior [40] (Reused with permission).

Although using piezoelectric actuators on morphing wing applications is shown to be feasible [12-16], further research is needed for flapping wing applications. Due to the complex motion of the wings and unsteady aerodynamic mechanisms, imitation of biological flyers (birds and insects) that employ flapping wings is non-trivial. For instance, insects both flap and rotate their wings during flight, and unsteady aerodynamic forces, which are clap and fling, rotational circulation, wake capture, and delayed stall, play a vital role on insect flight [43]. Sane et al. [44] investigated the effects of different parameters on insect flight, such as stroke amplitude, angle of attack, and flip duration. Birds do various motions such as flapping, twisting, sweeping, folding, and plunging in addition to moving their wings forward relative to air; and larger birds usually fold their wings during upstroke to reduce negative lift force [11]. In order to imitate biological flapping-wing flyers, researchers have built ornithopters which are capable of flapping and twisting. Typical ornithopters twist due to the inertial effects of the flexible wing, and they usually have an oriented flapping axis [12]. Piezoelectric actuators were employed on various ornithopters at different scales. Wood [45] designed a 3-cm-wingspan micro

air vehicle by using a bimorph piezoelectric cantilever actuator (Fig. 6). He measured the average lift force as 1.14 mN.

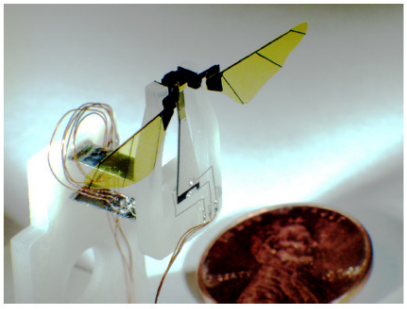

Figure 6. Micro air vehicle that uses piezoelectric bimorph cantilever as actuator [45] (Reused with permission, © 2007 IEEE).

Fukushima et al. [46] designed a ring shaped driving module with MFC actuation for a biologically inspired flapping insect (Fig. 7). The morphing of the ring module is transmitted to the flapping wing via hinges between the driving module and the wings. Insufficient lift and thrust levels were reported.

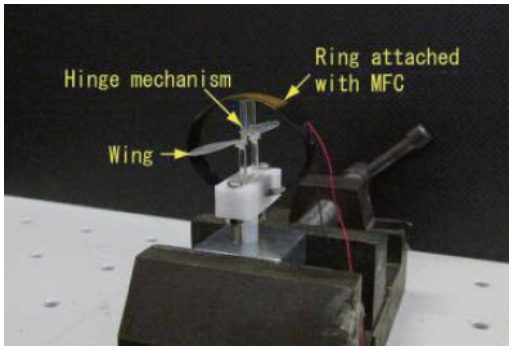

Figure 7. A flapping wing design with insect inspired ring shaped driving module actuated by MFC [46] (Reused with permission, © 2010 IEEE).

Ming et al. [18] tried an MFC actuated flapping wing with a span of 297 mm (Fig. 8). To have a stiffer wing, they added resin structural supports to the airfoil. For the stroke angle 60° they measured the maximum lift is 28.5 mN.

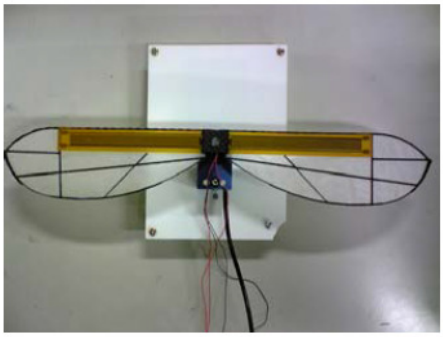

Figure 8. An MFC actuated UAV design with a span of 297 mm [18] (Reused with permission, © 2008 IEEE).

Ha et al. [17] made a flapping wing (Fig. 9) capable of doing flapping and twisting actuated by MFCs. The maximum flapping angle was found to be 23.2° whereas maximum twisting angle was 38.4°. Insufficient to propel the wing, the maximum thrust was measured to be 4.8 mN for a 90° phase difference between flapping and twisting actuators.

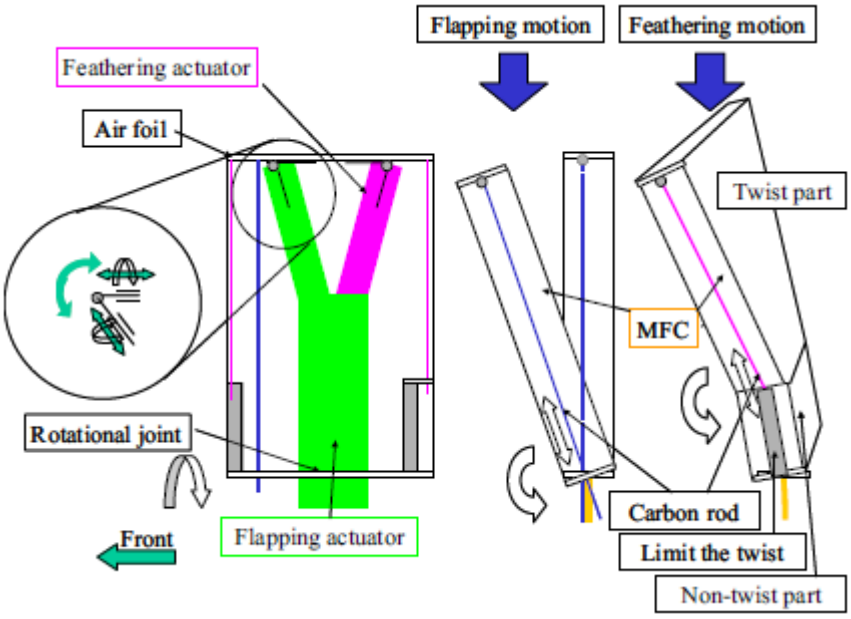

Figure 9. A flapping wing design that does both flapping and twisting motions [17] (Reused with permission, © 2006 IEEE).

Although there have been significant efforts on the use of piezoelectric actuators for flapping wing UAVs, further research is required for increasing lift and thrust resultants. Most of the ornithopter wing designs in literature do twist motion due to the inertial effects of the flexible wing. However, increased authority on twist and flapping motions can increase the lift and thrust resultants. For instance, hummingbird wings follow "figure 8 path" during hovering [47] (see Fig. 10 for zero flight speed). This motion is the combination of flapping and twisting. On the other hand, as the flight speed increases, the motion of the wing relative to the body follows an elliptical path, and the angle of attack changes. Hence, effective biomimetic flapping wing design requires high control on the bending and twisting motions.

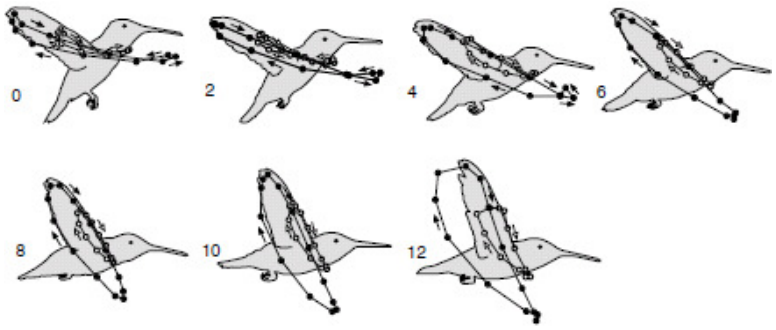

Figure 10. Hummingbird wing motion relative to its body at different flight speeds varying from 0 to 12 m/s [47] (Reused with permission).

2.2 Recent literature on bio-inspired aquatic vehicles using smart materials

There exists various successful designs with motors and appropriate linkage systems or mechanisms to mimic aquatic animal motion in the existing literature. Locomotion is typically obtained by creating an undulatory motion of the tail portion connected to a passive caudal fin [27-29]. Some of the other studies with motor based actuation include pectoral fins for locomotion [48, 49]. Although motor-based biomimetic vehicles have high swimming speeds, they are noisy and not easy to miniaturize. To overcome this problem, a number of research groups have used smart materials as actuators in bio-inspired aquatic robotics especially in the last few years [26].

The commonly used smart material actuators in biomimetic applications are ionic polymer metal composites (IPMCs), shape memory alloys (SMAs) and piezoelectrics as reviewed by Chu et al [26]. Among these three smart materials, the IPMC technology offers the highest mechanical deformation response to the lowest voltage input, making it arguably the most heavily researched smart material in biomimetic applications. Several studies have been conducted by actuating a tail embedded with IPMC, such as a

cantilever beam, with or without a passive caudal fin attached, including tadpole like robot in undulatory motion to create thrust in [30], an untethered swimming robot in [31], among other centimeter-scale examples [32, 33]. This type of locomotion created by IPMC (Fig. 11) has been well modelled by several authors [50-52]. Other types of IPMC-based biomimetic fish robots use several IPMC actuators either to mimic pectoral fins of a ray fish in rajiform swimming [53] or to mimic a jelly fish propulsion system [54].

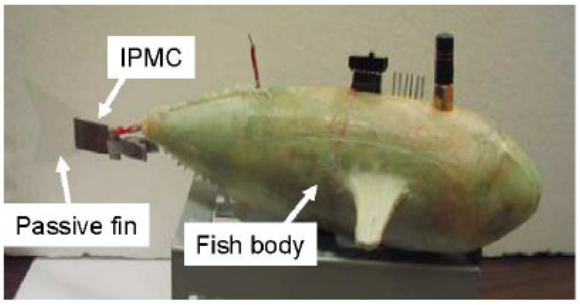

Figure 11. An IPMC actuated robotic fish with a passive caudal fin [52] (Reused with permission, © 2008 IEEE).

Although the SMA technology typically offers lower mechanical deformation compared to IPMC, they are shown to be feasible as biomimetic actuators. For instance, two types of robotic fish using SMA actuators were developed by Wang et al. [55] for carangiform locomotion and rajiform swimming. Rossi et al. [56] designed a robotic fish made of three segments, each actuated by a pair of SMA wires to create undulatory motion.

Piezoelectric actuators are used in many technological systems ranging from robotics to biomedical devices and in energy applications because they are scalable,

noiseless and energy efficient for low power applications (<30W) as compared to conventional actuators [1]. Piezoelectric actuators produce large amounts of force, but their deformation is small and they require high amount of voltage input. Therefore, in biomimetic locomotion, piezoelectric actuators are often used with linkage system (Fig. 12) to turn the high stress capability to large displacement results such that a feasible oscillatory motion is created at the caudal fin in [34, 35].

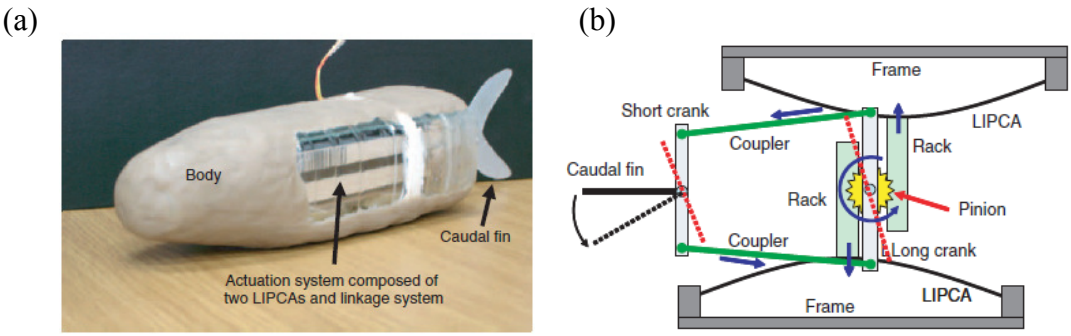

Figure 12. A robotic fish actuated by lightweight piezo-composite actuators (LIPCAs) (a) overall view (b) actuation mechanism [34] (Reused with permission).

Unlike conventional piezoelectric actuators, MFC technology provides high strain and stress performance based on the 33-mode of piezoelectricity (electric field and strain are in the same direction), flexibility, endurance, and they are manufactured in various sizes [2, 3]. Therefore MFCs overcome the problem of small displacement response associated with piezoelectric actuators without trading off the high actutation force capabililty. MFC actuators have beeen successfully used in tethered underwater robotic fish concepts [57-59]. Erturk and Delporte [36] investigated underwater thrust production by MFC bimorphs with and without a passive caudal fin (with a focus on the first two

mode shapes), and more recently, an untethered robotic fish (Figs. 13a-b) was developed and a swimming speed of 0.31 body length/second was achieved [60].

(a) 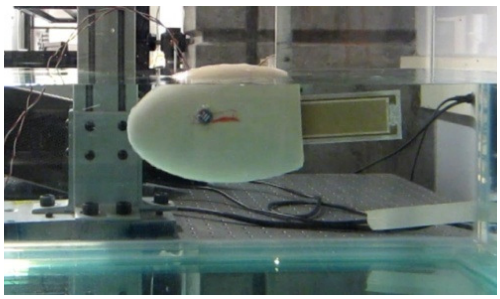 (b) 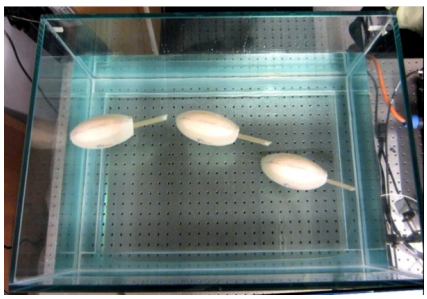

Figure 13. Pictures of an untethered MFC-based piezoelectric swimmer [60] (Reused with permission) showing the (a) side view and (b) top view for combined turning motion.

Although the existing fish-like aquatic locomotion efforts employ simple bending motions, experimental biologists have shown that fish caudal fin exhibits more complex motions than one-dimensional bending. Caudal fin muscle activity was recently investigated for different speeds under steady swimming conditions of a bluegill sunfish by Flammang and Lauder [37]. They observed that more muscles are activated to make complex motions with the fin as well as hardening in the fin while the fish swims faster. In addition, they characterized the different shapes that the caudal fin takes during unsteady swimming regimes of kick-and-glide, braking, and backing-up [38]. These biological observations inspired Esposito et al. [39] to build a caudal fin controlled by six fin rays actuated by a servomotor. With relatively different actuation of each fin rays, the robotic caudal fin was capable of following complex motion patterns, such as flat, cupping, undulation, and rolling motions (Fig. 14). In Fig. 14, flat is the pure bending of the caudal fin, and rolling is the combination of bending and twisting. Cup shape occurs

when the mid-section of the caudal fin lags the outer most sections. W motion is to name the W-like shape at the caudal fin when the fin rays located between the outer edges and the mid-section lags the motion of the caudal fin. Undulation motion refers to the wave-like motion starting at the dorsal edge moving toward the ventral edge at the caudal fin. Expectedly, thrust resultant (and lift) can be strongly affected by the nature of the caudal fin motion

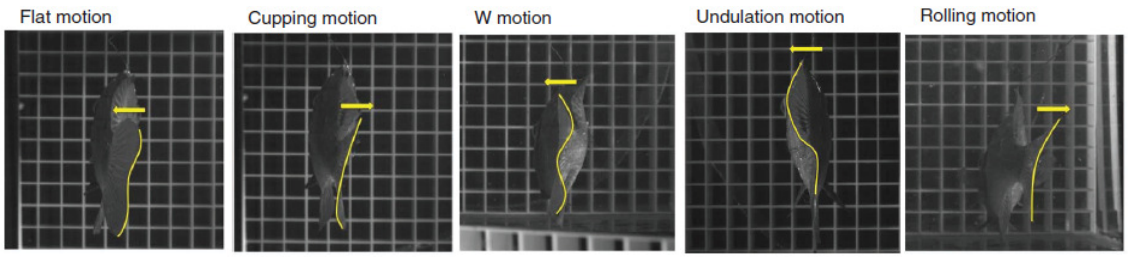

Figure 14. Motion of the caudal fin observed in biological fish [39] (Reused with permission).

2.3 Significance of the current research

In this thesis, active structures made of flexible Macro-Fiber Composite (MFC) piezoelectric materials for bio-inspired independent and combined bending-twisting actuation are investigated for potential flapping-wing flight and fish-like swimming applications using (1) an Asymmetric Bimorph (AB) with 0°/45°-fiber laminates, (2) a Double Bimorph (DB) with narrow 0°-fiber laminates (for flapping-wing applications), and (3) a Triple Bimorph (TB) with narrow 0°-fiber laminates (for aquatic robotics). The significance of this thesis work has multiple aspects with ramifications for bio-inspired structural dynamic systems.

Flapping-wing flight offers higher maneuverability and agility as compared to fixed-wing flight. Improved and independent actuation authority over bending and twisting motions can potentially enhance the asymmetry of flapping toward increasing the lift and thrust resultants. With this motivation, in this thesis, two MFC-based composite architectures (namely the AB and DB) are introduced, which are capable of producing both bending and twisting motions within a similar frequency range. Electroelastic bending and twisting actuation performance characteristics are determined experimentally for different actuation cases involving highly nonlinear response under different high voltage levels. The effect of airflow speed on the coupling of bending and twisting motions is also studied through wind-tunnel tests.

Varying stiffness wings are promising for morphing wing applications since lower stiffness is favorable during morphing process. Furthermore, altering the stiffness of a wing without changing its geometry can potentially be used to alter the flutter envelope of aircraft. Active stiffness change can also be combined with dynamic actuation for enabling varying stiffness caudal fins in underwater locomotion. Therefore, active stiffness change concept is tested on the MFC-based composite architecture by applying static actuation (DC voltage) and exploiting the static axial stress resultant produced by MFCs.

Triple Bimorph Piezoelectric Caudal Fin (TBPCF) made of narrow MFC piezoelectric bimorph actuators sharing a rubber substrate is investigated experimentally to form a three degree-of-freedom (DOF) caudal fin. Using different actuation voltage amplitude and phase patterns, flat, cup and rolling cases are explored. To the best of our knowledge, it is the first smart-material actuated 3-DOF caudal fin in the literature. The

dynamic response of the caudal fin is investigated in terms of velocity, phase, displacement and resultant thrust responses. Power consumption levels are also recorded. Thrust production of each actuation cases are compared considering both thrust resultants and power consumption levels.

One of the benefits of using MFC actuators is their low-power consumption. Therefore, power consumption levels of the MFC-based composite architectures are recorded for the bending-twisting mode and compared with typical power output levels that can be generated using flexible solar films of similar dimensions toward self-powered flapping. In addition to solar energy harvesting, electrical power generation from ambient vibrations is investigated by using the direct piezoelectric effect of the MFC-based composite architectures.

CHAPTER 3

ASYMMETRIC BIMORPH WITH WIDE 0°/45°-FIBER LAMINATES

3.1 Asymmetric bimorph with wide 0°/45°-fiber laminates

The first architecture investigated in this chapter is an asymmetrically laminated bimorph with 0°/45° MFC laminates (where the angles denote the orientation of the piezoelectric fibers as in conventional laminated composite structures [61, 62]). As shown in Fig. 15, one of the MFCs has 0° piezoelectric fibers (the top laminate – Fig. 15a), while the other one has 45° oriented piezoelectric fibers (the bottom laminate – Fig. 15b). The manufacturer's (Smart Material Corp.) product names of the MFCs with 0° and 45° laminates are M8557-P1 and M8557-F1, respectively. The dimensions of the active region that covers the piezoelectric fibers in both laminates are 57 mm x 77 mm and the total thickness is 0.67 mm. Each one of the MFC laminates has a thickness of around 0.31 mm. Therefore the epoxy thickness resulting from the vacuum bonding process (discussed in the next paragraph) is very low. The points of transverse velocity measurement (denoted by A, B, and C in Fig. 15) are selected to capture both bending and twisting motions. Two consecutive points have a 26 mm distance in between, and all three points are 79.5 mm away from the clamped end. The static capacitance values of the laminates in clamped-free end conditions are 10.9 nF and 15.5 nF for the 45° and 0° degree MFCs, respectively.

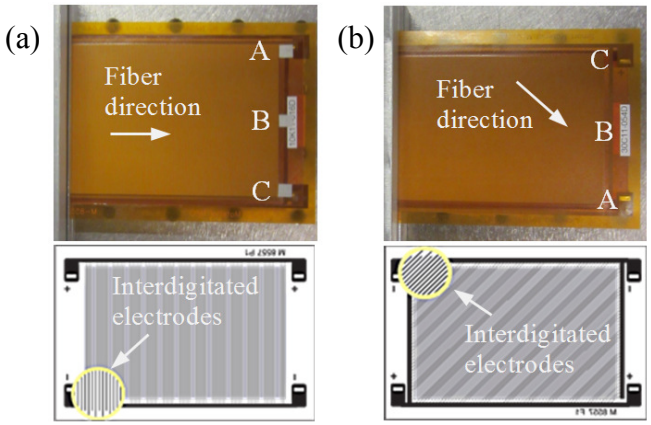

Figure 15. Asymmetric bimorph architecture with wide 0°/45° MFC laminates: (a) top laminate (0° fibers) and (b) bottom laminate (45° fibers) along with the tip velocity measurement points (A, B, and C). The samples are clamped at the left end of the view. The schematics from the manufacturer (Smart Material Corp.) display the interdigitated electrode fingers which are perpendicular to the fibers.

The composite laminates discussed in this thesis are assembled by using high shear strength epoxy in a vacuum bonding process (Fig. 16). First, 3M ScotchWeld™ DP460 two-part epoxy is uniformly distributed between the MFC laminates. Then, peel ply layers are placed both on top and bottom of the composite structure, and eventually it is covered by cotton layers before locating in the plastic bag. Note that, overall curing setup is supported by a flat metal surface in the plastic bag. During curing process, the composite structure is left 24 hours in the sealed plastic bag whose pressure is kept 20 in-Hg by a vacuum pump. Due to air pressure, excess epoxy is absorbed through peel ply and cotton layers during curing.

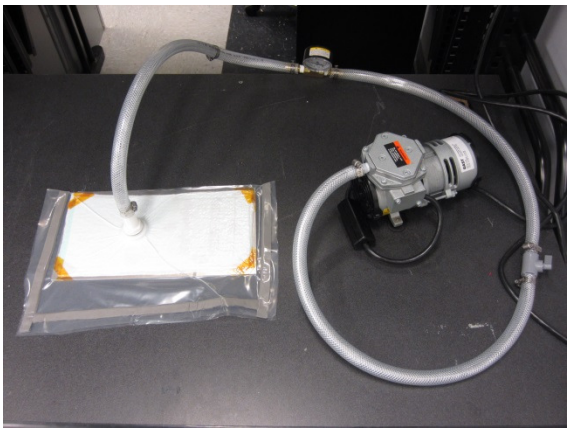

Figure 16. Vacuum bonding process setup showing the vacuum pump and the curing setup in a sealed plastic bag.

3.2 Experimental setup and measurement procedure

The experimental setup used for characterizing the aerial composite architectures investigated in this thesis is shown in Fig. 17. In order to characterize the electroelastic dynamics of the asymmetric bimorph, several different voltage levels and changing frequencies are applied to the MFCs using a data acquisition system (Siglab 20-42) and software in conjunction with high voltage amplifiers (Trek 2220) with current monitor, while the velocity response is measured at A, B and C points using a single-point laser vibrometer (Polytec OFV-505 with OFV-5000 controller) in a set of experiments. For all actuation cases, the frequency step is chosen to be 0.1 Hz around the resonant and antiresonant frequencies (and 1 Hz away from resonance and antiresonance regions). The displacement response is calculated by taking the integral of the velocity in frequency domain. The current drawn by the MFCs for a given actuation voltage level is used in calculating the power consumption. In the following, the velocity and displacement outputs are given in the form of peak-to-peak values corresponding to peak-to-peak

voltage input, and all results are reported in the magnitude form. Forward frequency sweep experiments are conducted and it is important to note that full nonlinear analysis would require backward sweep as well in the presence of hysteresis.

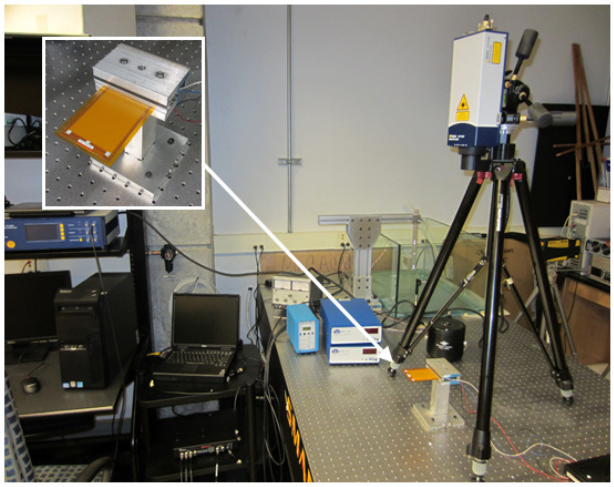

Figure 17. Experimental setup with a close up view of 0°/45° asymmetrically laminated MFC flapping cantilever and its aluminum fixture to realize clamped-free boundary conditions.

3.3 Linear modeling of the asymmetric bimorph for low-voltage actuation

The 0°/45° asymmetrically laminated wide bimorph cantilever is modeled as a 2-DOF lumped-parameter system (based on experimentally identified parameters); each degree of freedom representing the deflection of two measurement points that are located on two sides at the free end of the architecture (Fig. 18). The main goal in this effort is to have a descriptive model of the linear electroelastic system dynamics.

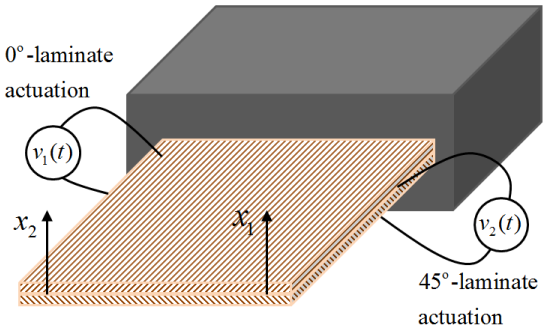

Figure 18. Schematic of 0°/45°-fiber asymmetrically laminated wide bimorph cantilever showing each degree of freedom along with the actuation voltage variables.

The governing equations in the physical coordinates can be given in the matrix form as

$$\begin{bmatrix} m & 0 \\ 0 & m \end{bmatrix}\begin{bmatrix} \ddot{x}_1 \\ \ddot{x}_2 \end{bmatrix}+\begin{bmatrix} k_a+k_b & -k_b \\ -k_b & k_a+k_b \end{bmatrix}\begin{bmatrix} x_1 \\ x_2 \end{bmatrix}=\begin{bmatrix} 0 \\ 0 \end{bmatrix} \tag{1}$$

where x_1 and x_2 stand for the peak-to-peak deflections of points A and C (Fig. 15) respectively, m is lumped mass of the architecture assumed to be identical at each node, and k_b represents the stiffness between the lumped masses, while k_a is assigned to represent the stiffness of each coordinate relative to the fixed end.

Introducing $\omega_a^2=\frac{k_a}{m}$ and $\omega_b^2=\frac{k_b}{m}$, Eq. (1) becomes,

$$\begin{bmatrix} 1 & 0 \\ 0 & 1 \end{bmatrix}\begin{bmatrix} \ddot{x}_1 \\ \ddot{x}_2 \end{bmatrix}+\begin{bmatrix} \omega_a^2+\omega_b^2 & -\omega_b^2 \\ -\omega_b^2 & \omega_a^2+\omega_b^2 \end{bmatrix}\begin{bmatrix} x_1 \\ x_2 \end{bmatrix}=\begin{bmatrix} 0 \\ 0 \end{bmatrix} \tag{2}$$

Since x_1 and x_2 are the peak-to-peak displacement responses to the harmonic actuation input, they can be represented as $x_{1,2}=X_{1,2}e^{j\omega t}$, where $j=\sqrt{-1}$ and ω is the actuation frequency. Thus Eq. (2) becomes

$$\begin{bmatrix} \omega_a^2 + \omega_b^2 - \omega^2 & -\omega_b^2 \\ -\omega_b^2 & \omega_a^2 + \omega_b^2 - \omega^2 \end{bmatrix} \begin{bmatrix} X_1 \\ X_2 \end{bmatrix} = \begin{bmatrix} 0 \\ 0 \end{bmatrix} \tag{3}$$

Based on the overall experimental behavior of the cantilever discussed in the following sections, at the bending mode natural frequency, ω_1, mode shape is $\begin{bmatrix} X_1 \\ X_2 \end{bmatrix} = \begin{bmatrix} 1 \\ 1 \end{bmatrix}$, and twist mode shape is $\begin{bmatrix} X_1 \\ X_2 \end{bmatrix} = \begin{bmatrix} 1 \\ -1 \end{bmatrix}$ at the twist natural frequency of ω_2. Therefore, following the standard eigensolution procedure, Eq. (4) represents the bending mode, and Eq. (5) represents the twist mode:

$$\begin{bmatrix} \omega_a^2 + \omega_b^2 - \omega_1^2 & -\omega_b^2 \\ -\omega_b^2 & \omega_a^2 + \omega_b^2 - \omega_1^2 \end{bmatrix} \begin{bmatrix} 1 \\ 1 \end{bmatrix} = 0 \tag{4}$$

$$\begin{bmatrix} \omega_a^2 + \omega_b^2 - \omega_2^2 & -\omega_b^2 \\ -\omega_b^2 & \omega_a^2 + \omega_b^2 - \omega_2^2 \end{bmatrix} \begin{bmatrix} 1 \\ -1 \end{bmatrix} = 0 \tag{5}$$

Here, ω_a is found from Eq. (4):

$$\begin{aligned} &\omega_a^2 + \omega_b^2 - \omega_1^2 - \omega_b^2 = 0 \\ &\omega_a = \omega_1 \end{aligned} \tag{6}$$

Similarly, ω_b is identified from Eq. (5):

$$\begin{aligned} &\omega_a^2 + \omega_b^2 - \omega_2^2 + \omega_b^2 = 0 \\ &\omega_2^2 = \omega_a^2 + 2\omega_b^2 \\ &\omega_b = \sqrt{\frac{\omega_2^2 - \omega_1^2}{2}} \end{aligned} \tag{7}$$

The experimental bending mode resonant frequency is ω_1 = 32 Hz and the experimental twist mode resonant frequency is ω_2 =96.4 Hz. Therefore, by using Eqs. (6) and (7), $\omega_a = \omega_1 = 32$ Hz and $\omega_b = \sqrt{\frac{96.4^2 - 32^2}{2}} = 64.3$ Hz.

Introducing damping and force terms to Eq. (2) yields

$$\begin{bmatrix} 1 & 0 \\ 0 & 1 \end{bmatrix}\begin{bmatrix} \ddot{x}_1 \\ \ddot{x}_2 \end{bmatrix} + \begin{bmatrix} c_1 & c_2 \\ c_3 & c_4 \end{bmatrix}\begin{bmatrix} \dot{x}_1 \\ \dot{x}_2 \end{bmatrix} + \begin{bmatrix} \omega_a^2 + \omega_b^2 & -\omega_b^2 \\ -\omega_b^2 & \omega_a^2 + \omega_b^2 \end{bmatrix}\begin{bmatrix} x_1 \\ x_2 \end{bmatrix} = \begin{bmatrix} 1 & a \\ 1 & b \end{bmatrix}\theta\begin{bmatrix} v_1 \\ v_2 \end{bmatrix} \quad (8)$$

where c is a damping coefficient, θ is the piezoelectric coupling (which correlates the voltage input to displacement response), v_1 is voltage input to 0° laminate, v_2 is actuation voltage for the 45° laminate, a and b are the rate of response at points A and C, respectively, due to the 45° laminate actuation. To decouple the system, the following coordinate transformation is applied

$$[x(t)] = [\Phi][\eta(t)] \quad (9)$$

where $[\eta(t)] = \begin{bmatrix} \eta_1(t) \\ \eta_2(t) \end{bmatrix}$ are the modal coordinates, and $[\Phi]$ is the mass-normalized modal matrix: $[\Phi] = \frac{1}{\sqrt{2}}\begin{bmatrix} 1 & 1 \\ 1 & -1 \end{bmatrix}$.

Therefore, Eq. (8) becomes

$$\begin{bmatrix} \ddot{\eta}_1 \\ \ddot{\eta}_2 \end{bmatrix} + \begin{bmatrix} 2\xi_1\omega_1 & 0 \\ 0 & 2\xi_2\omega_2 \end{bmatrix}\begin{bmatrix} \dot{\eta}_1 \\ \dot{\eta}_2 \end{bmatrix} + \begin{bmatrix} \omega_1^2 & 0 \\ 0 & \omega_2^2 \end{bmatrix}\begin{bmatrix} \eta_1 \\ \eta_2 \end{bmatrix} = [\Phi]^T\begin{bmatrix} 1 & a \\ 1 & b \end{bmatrix}\theta\begin{bmatrix} v_1 \\ v_2 \end{bmatrix} \quad (10)$$

where ξ is the damping ratio of the respective mode. Since the sample is actuated harmonically,

$$\nu(t) = Ve^{j\omega t} \tag{11}$$

yielding

$$\eta(t) = \mathrm{H}e^{j\omega t} \tag{12}$$

at steady state.

Therefore Eq. 10 becomes

$$\begin{bmatrix} \omega_1^2 - \omega^2 + 2j\xi_1\omega_1\omega & 0 \\ 0 & \omega_2^2 - \omega^2 + 2j\xi_2\omega_2\omega \end{bmatrix} \begin{bmatrix} \mathrm{H}_1 \\ \mathrm{H}_2 \end{bmatrix} = \frac{1}{\sqrt{2}} \begin{bmatrix} 2 & a+b \\ 0 & a-b \end{bmatrix} \theta \begin{bmatrix} V_1 \\ V_2 \end{bmatrix} \tag{13}$$

$$\begin{bmatrix} \mathrm{H}_1 \\ \mathrm{H}_2 \end{bmatrix} = \begin{bmatrix} \beta_{11} & \beta_{12} \\ \beta_{21} & \beta_{22} \end{bmatrix} \begin{bmatrix} V_1 \\ V_2 \end{bmatrix} \tag{14}$$

where $\beta_{11} = \dfrac{2/\sqrt{2}\,\theta}{\omega_1^2 - \omega^2 + 2j\xi_1\omega_1\omega}$, $\beta_{12} = \dfrac{1/\sqrt{2}\,\theta(a+b)}{\omega_1^2 - \omega^2 + 2j\xi_1\omega_1\omega}$, $\beta_{21} = 0$, and $\beta_{22} = \dfrac{1/\sqrt{2}\,\theta(a-b)}{\omega_2^2 - \omega^2 + 2j\xi_2\omega_2\omega}$.

Transforming back to the physical coordinates yields

$$[X] = [\Phi][\mathrm{H}] = [\Phi] \begin{bmatrix} \beta_{11} & \beta_{12} \\ \beta_{21} & \beta_{22} \end{bmatrix} \begin{bmatrix} V_1 \\ V_2 \end{bmatrix} = \begin{bmatrix} \alpha_{11} & \alpha_{12} \\ \alpha_{21} & \alpha_{22} \end{bmatrix} \begin{bmatrix} V_1 \\ V_2 \end{bmatrix} \tag{15}$$

where $[\alpha]=[\Phi][\beta]=\frac{1}{\sqrt{2}}\begin{bmatrix}\beta_{11}+\beta_{21} & \beta_{12}+\beta_{22}\\ \beta_{11}-\beta_{21} & \beta_{12}-\beta_{22}\end{bmatrix}$ is the matrix of actuation frequency response functions (FRFs).

Therefore, one obtains

$$\alpha_{11}(\omega)=\alpha_{21}(\omega)=\frac{\theta}{\omega_1^2-\omega^2+2j\xi_1\omega_1\omega} \tag{16}$$

$$\alpha_{12}(\omega)=\frac{1/2\,\theta(a+b)}{\omega_1^2-\omega^2+2j\xi_1\omega_1\omega}+\frac{1/2\,\theta(a-b)}{\omega_2^2-\omega^2+2j\xi_2\omega_2\omega} \tag{17}$$

$$\alpha_{22}(\omega)=\frac{1/2\,\theta(a+b)}{\omega_1^2-\omega^2+2j\xi_1\omega_1\omega}-\frac{1/2\,\theta(a-b)}{\omega_2^2-\omega^2+2j\xi_2\omega_2\omega} \tag{18}$$

Experimental data for each α are taken by actuating laminates separately, and the displacement responses are measured at the measurement points A and C for both actuation cases. In order to be in the linear region, a very low voltage input, 1 V peak to peak is applied. There are five unknown model parameters for $[\alpha]$, which are θ, ξ_1, ξ_2, a, and b. In order to determine θ, damping ratios are set to zero. Considering the α_{11}, which is not related to a or b, tuning θ gives a good match between experimental data and model except the resonant regions where the modeling response is infinite due to zero damping. Then, ξ_1 and ξ_2 are identified from the resonant regions. Thus θ, ξ_1 and ξ_2 are found as $\theta=50\ (\text{mm/s}^2)/V$, $\xi_1=0.0154$, and $\xi_2=0.0118$. Both experimental data and model results for α_{11} and α_{21} FRFs are given in Fig. 19.

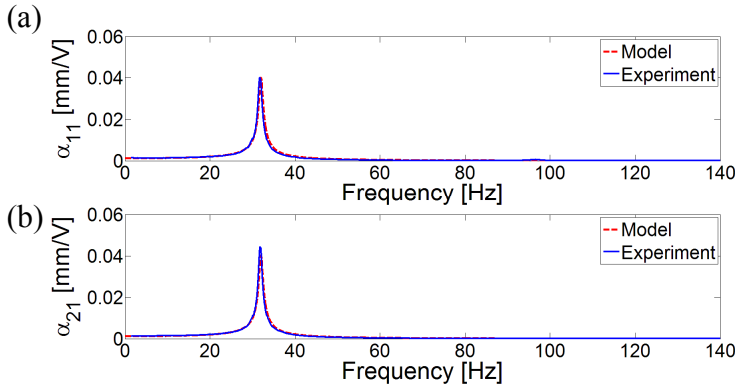

Figure 19. Peak-to-peak displacement response of the asymmetric bimorph measured at (a) point A, α_{11}, and (b) point C, α_{21}, due to the actuation of 0°-fiber laminate.

Figure 20 compares experimental data and model for α_{12} and α_{22} that are displacement responses at point A and point C, respectively, due to 45° laminate actuation with 1 V peak to peak. To identify the values of a and b in Eqs. (17) and (18), the response at the bending modes of α_{12} and α_{11} are compared (based on the experimental data). At the bending mode, setting ω to ω_1 in Eqs. (16) and (17), that defines α_{11} and α_{12} respectively, and dividing α_{12} by α_{11} leads to

$$\frac{\alpha_{12}}{\alpha_{11}} \cong \frac{a+b}{2} \cong \frac{0.0144}{0.04} \cong 0.36 \tag{19}$$

Since the displacement response graphs are in absolute form, $abs(a+b) = 0.72$.

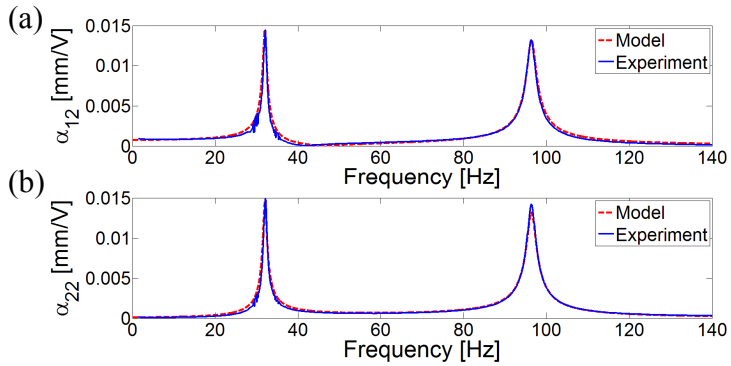

Figure 20. Peak-to-peak displacement response of the asymmetric bimorph measured at (a) point A, α_{12}, and (b) point C, α_{22}, due to the actuation of 45°-fiber laminate.

A combined actuation case is tried on the 0°/45° laminated cantilever. V_1 and V_2 in Eq. (15), are set to 1 V and -1 V respectively in order to create out of phase actuation of the laminates. Since the formulations for each α FRF are known, combined actuation case can be modeled by Eq. (15). Figure 21 compares experimental results with the model for the combined actuation case. Both 45° laminate actuation case and combined actuation case depend on a and b, which are $a = 2.64$, $b = -1.92$ in agreement with Eq. (19).

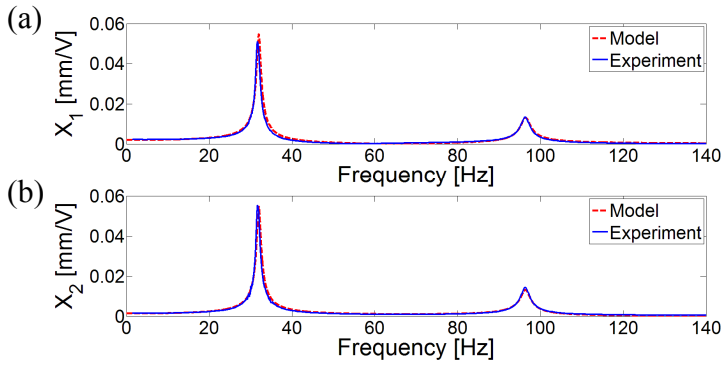

Figure 21. Peak-to-peak displacement response of the asymmetric bimorph measured at (a) point A, and (b) point C due to out-of-phase combined actuation of 0° and 45°-fiber laminates.

3.4 Stiffness identification for the asymmetric bimorph

The stiffness matrix of the 0°/45° asymmetrically laminated MFC flapping cantilever is identified experimentally. First, different loads are applied to the sample in order to find each element of the flexibility matrix, $[A]$, in Eq. (20), and eventually taking the reciprocal of the flexibility matrix results in the stiffness matrix of the beam. The displacement results and point loads are related by

$$\begin{bmatrix} X_1 \\ X_2 \end{bmatrix} = \begin{bmatrix} A_{11} & A_{12} \\ A_{21} & A_{22} \end{bmatrix} \begin{bmatrix} F_1 \\ F_2 \end{bmatrix} \tag{20}$$

where X_1 and X_2 are the displacement response shown in Fig. 18; F_1 and F_2 are the loads applied to the measurement points A and C (Fig 15) respectively.

Figure 22 presents experimental measurements of deflection, X_1 and X_2 for different loading conditions at short circuit condition. Stiffness matrix is theoretically symmetric, so is the flexibility matrix. Therefore, experimental data related to the

diagonal and off-diagonal terms of the flexibility matrix are averaged separately, and two curves are fitted whose slopes are the elements of the flexibility matrix.

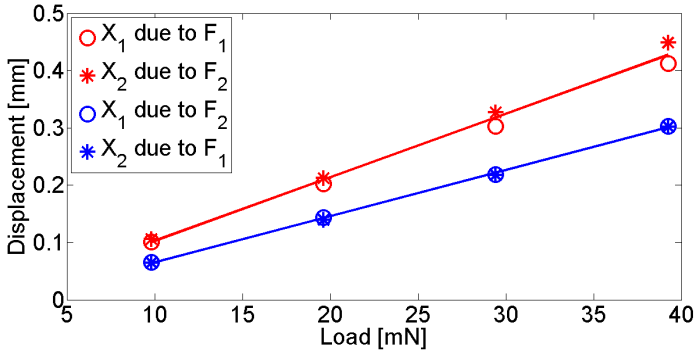

Figure 22. Experimental data of deflection versus different cases of loading for determining the flexibility matrix of the 0°/45° asymmetrically laminated MFC flapping cantilever. (Solid lines are curve fit to the average of experimental data related to diagonal and off-diagonal terms of the flexibility matrix).

Based on the slopes of the curve fits to the experimental data of deflection in Fig. 22, short circuit flexibility matrix for the 0°/45° asymmetrically laminated MFC flapping cantilever is

$$[A] = \begin{bmatrix} 0.0111 & 0.0080 \\ 0.0080 & 0.0111 \end{bmatrix} (\text{mm/mN}) \tag{21}$$

Stiffness matrix is the inverse of the flexibility matrix:

$$[K] = [A]^{-1} = \begin{bmatrix} 187.4683 & -135.1123 \\ -135.1123 & 187.4683 \end{bmatrix} (\text{N/m}) \tag{22}$$

Note that, in section 3.3 the values of ω_a and ω_b were found. Therefore the stiffness matrix for unit mass (i.e. identity mass matrix) is

$$[K]' = \begin{bmatrix} \omega_a^2 + \omega_b^2 & -\omega_b^2 \\ -\omega_b^2 & \omega_a^2 + \omega_b^2 \end{bmatrix} = \begin{bmatrix} 203650 & -163220 \\ -163220 & 203650 \end{bmatrix} (1/\mathrm{s}^2) \tag{23}$$

Thus the element-wise ratio of K to the K' gives the lumped masses as

$$\begin{aligned} m_1 &= \frac{187468.3}{203650} = 0.9205 \text{ g} \\ m_2 &= \frac{135112.3}{163220} = 0.8278 \text{ g} \end{aligned} \tag{24}$$

Lumped masses were assumed to be identical, yielding the following mass matrix based on the average of m_1 and m_2:

$$[M] = \begin{bmatrix} 0.8741 & 0 \\ 0 & 0.8741 \end{bmatrix} \text{ g} \tag{25}$$

which is therefore the experimentally identified mass matrix based on the static stiffness components and natural frequencies.

3.5 High voltage characterization of the asymmetric bimorph and nonlinear response

In order to characterize the 0°/45° asymmetrically laminated wide bimorph cantilever, the two laminates are actuated separately. Forward frequency sweep experiments are conducted for a wide range of voltage levels. In both actuation cases, the peak-to-peak voltage level ranges from 5 V to 800 V while the frequency range is 1-140 Hz. Then, combined actuation case is applied by actuating the laminates 180° out-of-phase.

3.5.1 Actuation using the 45° MFC laminate:

Peak-to-peak velocity frequency response curves at points A, B and C (Fig. 15) due to 45°-MFC actuation are presented in Fig. 23. The resonant frequency of the fundamental bending mode of the asymmetric bimorph decreases from 33 Hz to 27.5 Hz as the peak-to-peak voltage input increases from 5 V to 800 V. This behavior is an indication of *softening* nonlinearity of the laminate and is typically observed for the first bending mode in high voltage piezoelectric actuation as well as under high mechanical excitation levels in piezoelectric energy harvesting [63-65]. In addition, the first bending mode is observed to have large and comparable amplitudes at all three points of measurement although the amplitude at point A is slightly larger due to the fiber orientation.

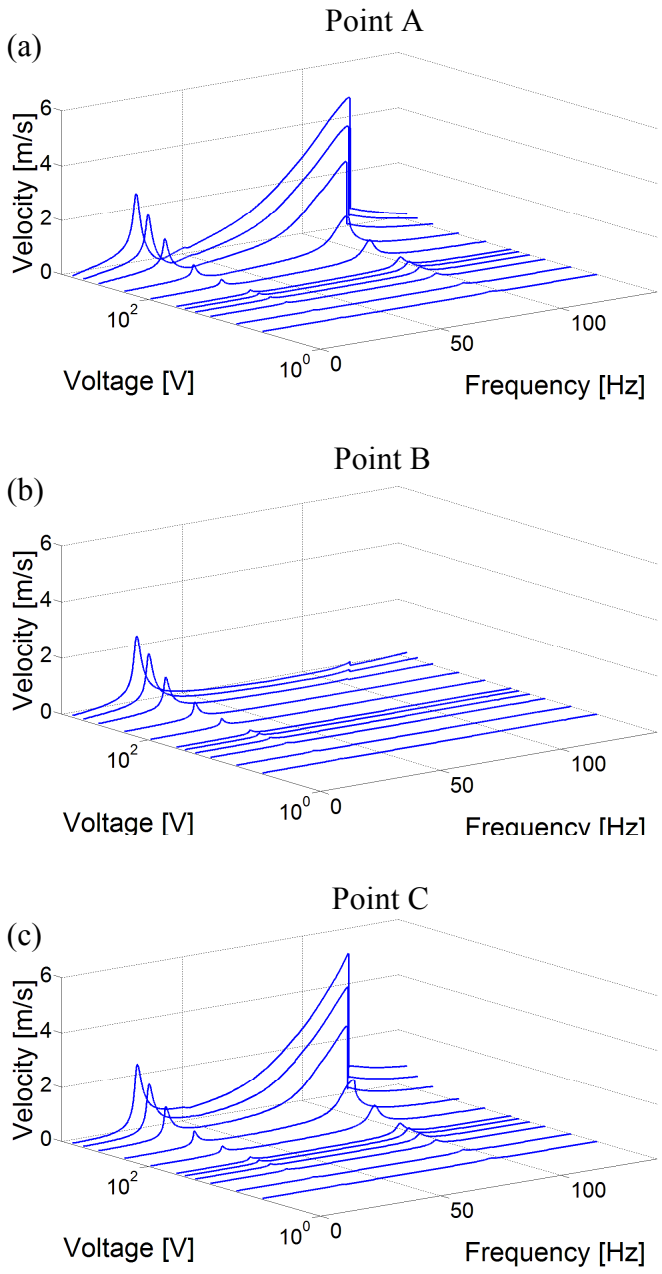

Figure 23. Peak-to-peak tip velocity frequency response curves measured at (a) point A, (b) point B, and (c) point C for actuation with different peak-to-peak voltage input levels using the 45° MFC laminate (forward frequency sweep).

The resonant frequency of the fundamental twist mode first decreases from 95.4 Hz to 94 Hz as the voltage input is increased from 5 V to 50 V, which can again be attributed to piezoelectric softening [63-65]. However, starting from 100 V voltage input, the twist mode exhibits *hardening* nonlinearity, which is expected to be due to geometric effects [66], with an increase in the resonant frequency from 94.2 Hz to 115.7 Hz when the peak-to-peak voltage input reaches 800 V. Resulting from the hardening nonlinearity, the asymmetric bimorph experiences the jump phenomenon [67], which is a sudden drop in response due to forward frequency sweep, as observed in Fig. 23 above 400 V input actuation.

Note that the anti-resonance following the first bending mode in the point A measurements is not observed in the point C measurements (which is due to the orientation of the 45° fibers). Additionally, point B is a stationary point for the twist mode, and the velocity response amplitude at point B is almost zero for the twist mode (Fig. 23).

3.5.2 Actuation using the 0° MFC laminate:

Actuation with the 0° MFC laminate results in velocity frequency response curves at points A, B and C shown in Fig. 24. Vibration response around the twist mode is very small as compared to the 45°-MFC actuation case since the 0° fibers primarily pronounce bending rather than twisting. Moreover, the velocity response at point B shows essentially no displacement around the twist mode since this point of measurement is an almost stationary point for the twist mode. As expected, the velocity response of the bending mode of the 0°-MFC actuation case is higher than the bending mode velocity response of the 45°-MFC actuation case since the 0°-MFC primarily excites the bending

mode. Note that the fundamental bending mode exhibits softening nonlinearity in this case as well.

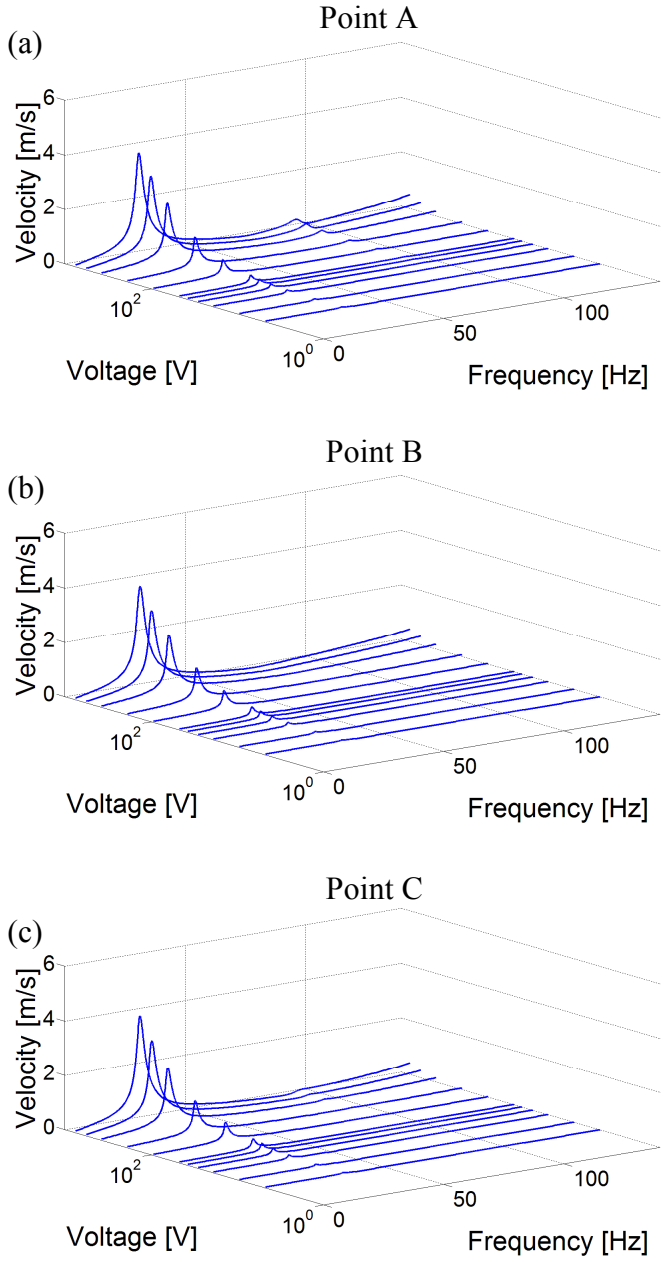

Figure 24. Peak-to-peak tip velocity frequency response curves measured at (a) point A, (b) point B, and (c) point C for actuation with different peak-to-peak voltage input levels using the 0° MFC laminate (forward frequency sweep).

The displacement response of the asymmetric bimorph is calculated by taking time integral of the velocity responses at the three different points of measurement, A, B and C. The resonant peak-to-peak displacement values for both bending resonance and twist resonance are plotted in Fig. 25. The displacement values for actuation using the 45° and 0° laminates are shown in Figs. 25a and 25b, respectively. As observed in Fig. 25a, there is a slight twist at the first bending mode, such that due to 45° fiber laminate actuation, displacement of point A is approximately 1 mm larger than points B and C (when input voltage is 800 V). Therefore the cantilever does both bending and small amount of twist although it is actuated at the bending dominated resonant frequency. Comparing Figs. 25a and 25b shows that bending displacement response of the 0° fiber actuation case is larger than the 45° fiber actuation case. However, twist displacement of 0° fiber actuation case is almost zero. On the other hand, actuation using the 45° fibers does result in twisting.

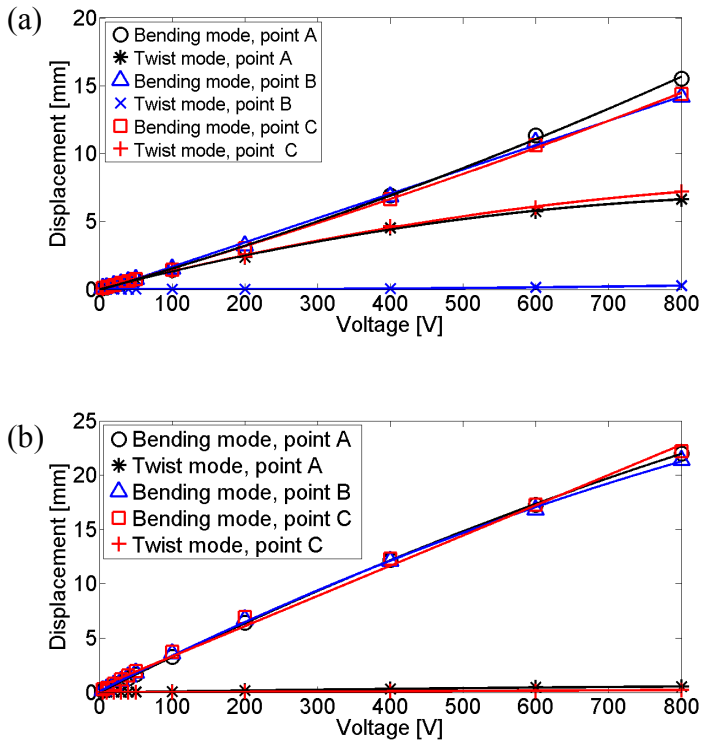

Figure 25. Resonant peak-to-peak displacement values for the bending and twist modes measured at points A, B, and C due to actuation using the (a) 45° and (b) 0° MFC laminates (solid lines are curve fit).

3.5.3 Combined actuation case of the asymmetric bimorph

To investigate the effect of actuating both laminates of the 0°/45° asymmetrically laminated MFC bimorph at the same time, the 0° and 45° laminates are connected in parallel and actuated 180° out of phase. Peak-to-peak voltage levels of 200 V, 400 V, 600 V and 800 V are applied with changing frequencies between 1-140 Hz. Figure 26 presents the velocity response of the asymmetric bimorph at the measurement points A, B, and C (Fig. 15). Both bending and twisting modes are observed except for point B which is stationary point for the twist mode. The *softening* nonlinearity is observed as the resonant frequency of the bending mode decreases from 28 Hz to 25.4 Hz, and the

hardening nonlinearity is seen since the resonant frequency of the twist mode increases from 95.2 Hz to 113 Hz due to increased actuation voltage.

Figure 27 presents the effect of combined actuation by comparing it with the separate actuation cases of the 45° laminate and 0° laminate covered in Sections 3.5.1 and 3.5.2. As one would expect, velocity response of the combined actuation is roughly the sum of the two separate actuation cases although the overall dynamics is highly nonlinear.

Figure 28 presents the resonant displacement values of the bending and twisting modes for the combined actuation case. As compared to the separate actuation case, the combined actuation scenario results in quite symmetric motion such that displacements of A, B and C points at the bending mode are essentially the same, and displacements of points A and C points are same for the twisting mode (Fig. 28).

Current consumption due to combined actuation of the asymmetric bimorph is plotted in Fig. 29. As expected, current consumption increases as the input voltage level increases. Moreover, current consumption increases as the frequency of actuation increases, and current consumption makes local peaks at the resonant frequencies of bending and twisting modes.

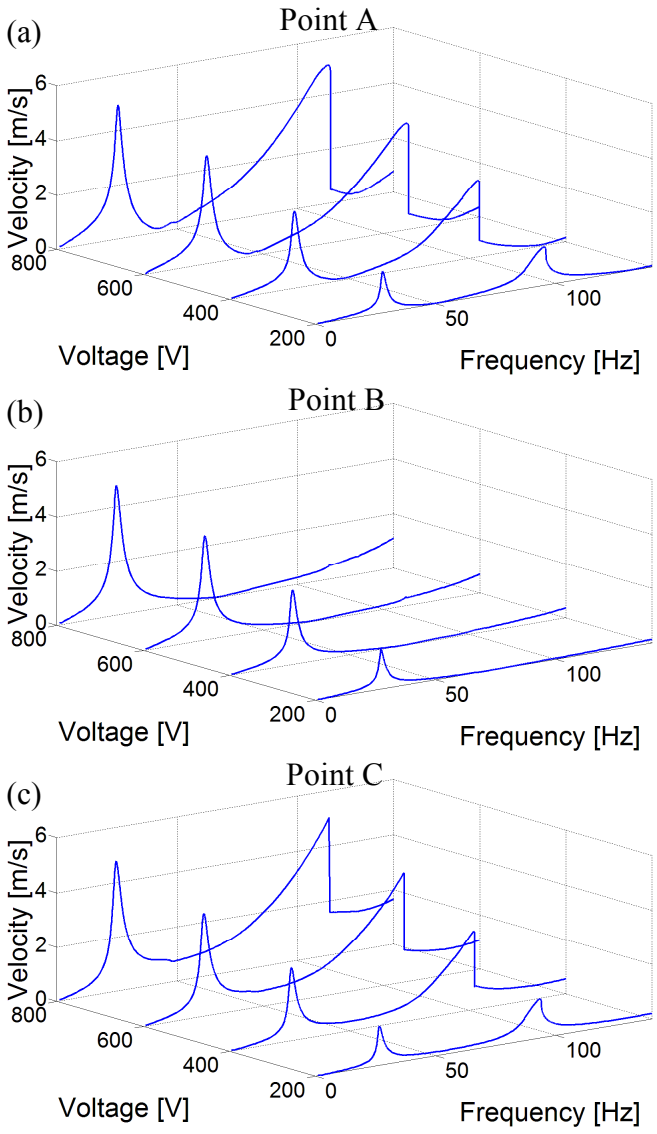

Figure 26. Peak-to-peak tip velocity frequency response curves measured at (a) point A, (b) point B, and (c) point C for combined actuation of the asymmetric bimorph with different peak-to-peak voltage input levels (forward frequency sweep). The top (0° MFC) and the bottom (45° MFC) laminates are actuated simultaneously 180° out of phase.

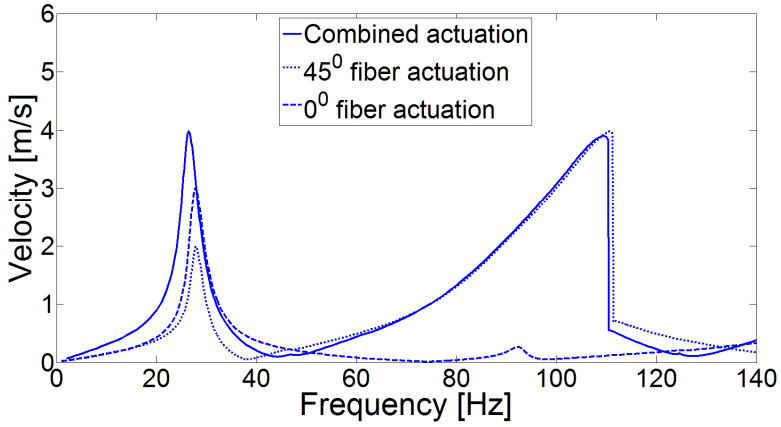

Figure 27. Comparison of combined (45° and 0° laminates out of phase simultaneously) and separate (45° laminate and 0° laminate separately) actuation cases with a focus on the peak-to-peak velocity response at point A for a peak-to-peak voltage input of 600 V (forward frequency sweep).

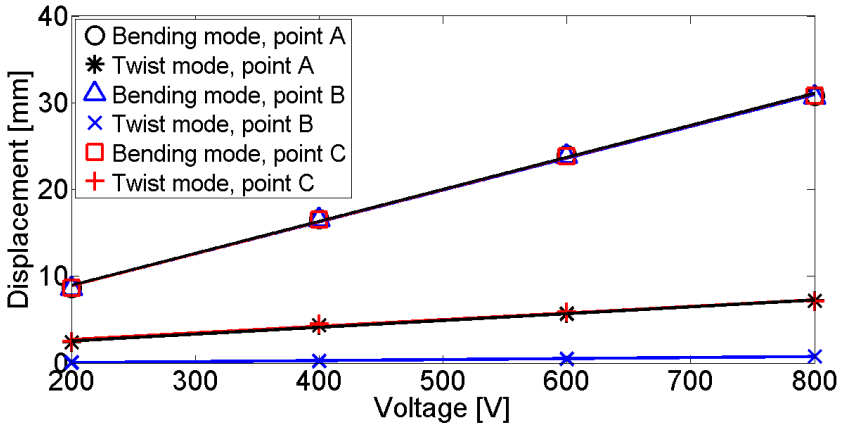

Figure 28. Resonant peak-to-peak displacement values for the bending and twist modes measured at points A, B, and C due to combined actuation of the asymmetric bimorph (solid lines are curve fit).

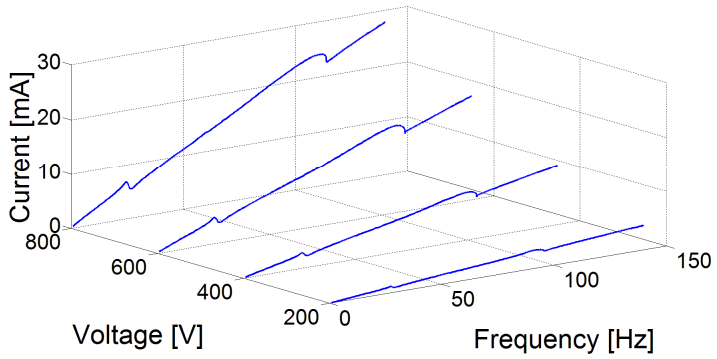

Figure 29. Frequency response curves of current consumption amplitude for different peak-to-peak voltage levels due to combined actuation of the asymmetric bimorph (forward frequency sweep).

3.5.4 Flapping and twisting angles

Displacement response at the first bending and twist resonance of the asymmetric bimorph in different actuation cases were presented before. Since displacement values and the geometry of the architecture are known, maximum flapping angle and twist angle for each different experimental case are calculated and tabulated in Table 1. Flapping angle is calculated at the bending mode (BM), and twist angle is calculated at the twist mode (TM). Note that the data in Table 1 are from peak to peak values.

Table 1. Maximum flapping and twist angle results observed during actuation of the asymmetric bimorph.

Experiment Type	Frequency (Hz)	Voltage Input (V)	Flapping Angle (Degree)	Twist Angle (Degree)
0° actuation	27.3 (BM) 92.5 (TM)	800	16.2	0.8
45° actuation	27.3 (BM) 116 (TM)	800	11.2	15.3
Combined Actuation	25.4 (BM) 113 (TM)	800	22.8	15.7

For the asymmetric bimorph, 0°-MFC actuation provides mostly bending, but actuating only 45° MFC provides both bending and twisting. For the same architecture, combined actuation responses are close to the sum of the separate actuation cases. Note that the combined actuation case yields slightly lower resonance frequencies.

CHAPTER 4

DOUBLE BIMORPH WITH NARROW 0°-FIBER LAMINATES

4.1 Double bimorph with narrow 0°-fiber laminates

As displayed in Fig. 30, the double bimorph architecture is built by bonding four 0° MFC laminates (M8514-P1, Smart Material Corp.) onto a flexible solar film substrate (MPT3.6-150, PowerFilm, Inc). Therefore, essentially two bimorphs are formed with a chord wise spacing of 18 mm to constitute a double bimorph. Each MFC has an active region of 74 mm x 14 mm and a thickness of 0.30 mm and the clamped-free capacitance of each MFC is 4 nF. The two MFCs in the top view (Fig. 30a) from the top to bottom are labeled as MFCs (1) and (2) while the two MFCs in the bottom view (Fig. 30b) from the top to bottom are labeled as (3) and (4), respectively. Once again, the points of transverse velocity measurement (denoted by A, B, and C in Fig. 30) are selected to capture both bending and twisting motions. The spacing between A to B and B to C is 23.5 mm, and all of the points are 76 mm far from the clamped end. The substrate is silicon-based solar film with a thickness of 0.17 mm. Overall the architecture is 75 mm wide, 82 mm long, and the thickness of the structure increases from 0.17 mm to 0.85 mm at the regions of the MFCs. The same experimental setup, which is described in section 3.2, is used for characterization of the double bimorph.

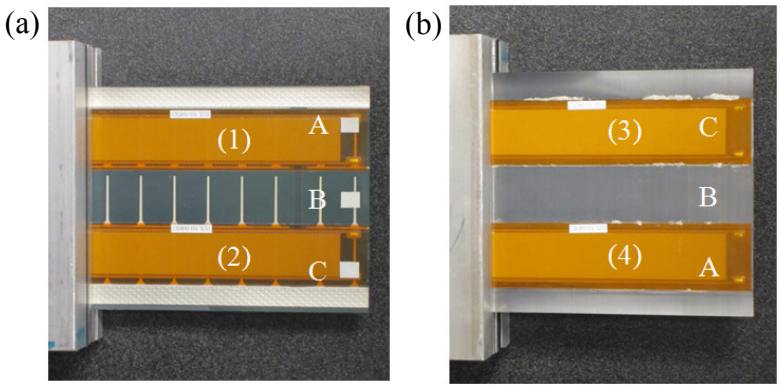

Figure 30. Double bimorph architecture with narrow 0° MFC laminates and solar film substrate: (a) top view and (b) bottom view along with the tip velocity measurement points and labeling detail of the four laminates (top laminates: (1) and (2); bottom laminates: (3) and (4)). The samples are clamped at the left end of the view.

4.2 Linear modeling of the double bimorph for low-voltage actuation

As shown in Fig. 31, double bimorph is modeled as a 2-DOF system; each degree of freedom is representing the tip deflection of one narrow bimorph. Therefore, undamped and unforced model of the asymmetric bimorph architecture is valid for the double bimorph as well:

$$\begin{bmatrix} m & 0 \\ 0 & m \end{bmatrix}\begin{bmatrix} \ddot{x}_1 \\ \ddot{x}_2 \end{bmatrix}+\begin{bmatrix} k_a+k_b & -k_b \\ -k_b & k_a+k_b \end{bmatrix}\begin{bmatrix} x_1 \\ x_2 \end{bmatrix}=\begin{bmatrix} 0 \\ 0 \end{bmatrix} \tag{26}$$

where x_1 and x_2 stands for the peak-to-peak deflection of each bimorph, m is the lumped mass, and k_b represents the stiffness between the bimorphs while k_a is assigned to represent the stiffness of each coordinate relative to the fixed end.

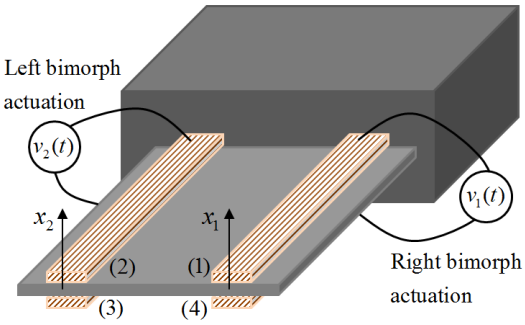

Figure 31. Schematic of the double bimorph architecture showing each degree of freedom along with the actuation voltage variables.

Introducing $\omega_a^2 = \frac{k_a}{m}$ and $\omega_b^2 = \frac{k_b}{m}$, Eq. (26) becomes

$$\begin{bmatrix} 1 & 0 \\ 0 & 1 \end{bmatrix} \begin{bmatrix} \ddot{x}_1 \\ \ddot{x}_2 \end{bmatrix} + \begin{bmatrix} \omega_a^2 + \omega_b^2 & -\omega_b^2 \\ -\omega_b^2 & \omega_a^2 + \omega_b^2 \end{bmatrix} \begin{bmatrix} x_1 \\ x_2 \end{bmatrix} = \begin{bmatrix} 0 \\ 0 \end{bmatrix} \tag{27}$$

The solution to the Eq. (27) was given in Eqs. (6) and (7) as

$$\begin{aligned} \omega_a &= \omega_1 \\ \omega_b &= \sqrt{\frac{\omega_2^2 - \omega_1^2}{2}} \end{aligned} \tag{28}$$

Based on the experimental results $\omega_1 = 55.3$ Hz and $\omega_2 = 76.4$ Hz. Therefore ω_a and ω_b are found by using Eq. (28) as, $\omega_a = \omega_1 = 55.3$ Hz, $\omega_b = \sqrt{\frac{76.4^2 - 55.3^2}{2}} = 37.3$ Hz.

The damped and forced system can be represented as

$$\begin{bmatrix} 1 & 0 \\ 0 & 1 \end{bmatrix} \begin{bmatrix} \ddot{x}_1 \\ \ddot{x}_2 \end{bmatrix} + \begin{bmatrix} c_1 & c_2 \\ c_3 & c_4 \end{bmatrix} \begin{bmatrix} \dot{x}_1 \\ \dot{x}_2 \end{bmatrix} + \begin{bmatrix} \omega_a^2 + \omega_b^2 & -\omega_b^2 \\ -\omega_b^2 & \omega_a^2 + \omega_b^2 \end{bmatrix} \begin{bmatrix} x_1 \\ x_2 \end{bmatrix} = \begin{bmatrix} 1 & 0 \\ 0 & 1 \end{bmatrix} \theta \begin{bmatrix} v_1 \\ v_2 \end{bmatrix} \tag{29}$$

where c, θ, and v terms are the damping coefficients, piezoelectric coupling (which correlates the voltage input to displacement response), and voltage input, respectively. Model is transformed to modal coordinates from physical coordinates by the same procedure followed in section 3.3, therefore Eq. (29) becomes,

$$\begin{bmatrix} \omega_1^2 - \omega^2 + 2j\xi_1\omega_1\omega & 0 \\ 0 & \omega_2^2 - \omega^2 + 2j\xi_2\omega_2\omega \end{bmatrix} \begin{bmatrix} \mathrm{H}_1 \\ \mathrm{H}_2 \end{bmatrix} = \frac{1}{\sqrt{2}} \begin{bmatrix} 1 & 1 \\ 1 & -1 \end{bmatrix} \theta \begin{bmatrix} V_1 \\ V_2 \end{bmatrix} \tag{30}$$

$$\begin{bmatrix} \mathrm{H}_1 \\ \mathrm{H}_2 \end{bmatrix} = \begin{bmatrix} \beta_{11} & \beta_{12} \\ \beta_{21} & \beta_{22} \end{bmatrix} \begin{bmatrix} V_1 \\ V_2 \end{bmatrix} \tag{31}$$

where $\beta_{11} = \beta_{12} = \dfrac{1/\sqrt{2}\,\theta}{\omega_1^2 - \omega^2 + 2j\xi_1\omega_1\omega}$, $\beta_{21} = \dfrac{1/\sqrt{2}\,\theta}{\omega_2^2 - \omega^2 + 2j\xi_2\omega_2\omega}$, and $\beta_{22} = \dfrac{-1/\sqrt{2}\,\theta}{\omega_2^2 - \omega^2 + 2j\xi_2\omega_2\omega}$.

Transforming back to physical coordinates yields

$$[X] = [\Phi][\mathrm{H}] = [\Phi] \begin{bmatrix} \beta_{11} & \beta_{12} \\ \beta_{21} & \beta_{22} \end{bmatrix} \begin{bmatrix} V_1 \\ V_2 \end{bmatrix} = \begin{bmatrix} \alpha_{11} & \alpha_{12} \\ \alpha_{21} & \alpha_{22} \end{bmatrix} \begin{bmatrix} V_1 \\ V_2 \end{bmatrix} \tag{32}$$

where $[\alpha] = [\Phi][\beta] = \dfrac{1}{\sqrt{2}} \begin{bmatrix} \beta_{11} + \beta_{21} & \beta_{12} + \beta_{22} \\ \beta_{11} - \beta_{21} & \beta_{12} - \beta_{22} \end{bmatrix}$ is the matrix of actuation frequency response functions (FRFs). Therefore,

$$\alpha_{11}(\omega) = \alpha_{22}(\omega) = \frac{1/2\,\theta}{\omega_1^2 - \omega^2 + 2j\xi_1\omega_1\omega} + \frac{1/2\,\theta}{\omega_2^2 - \omega^2 + 2j\xi_2\omega_2\omega} \tag{33}$$

$$\alpha_{12}(\omega)=\alpha_{21}(\omega)=\frac{\frac{1}{2}\theta}{\omega_1^2-\omega^2+2j\xi_1\omega_1\omega}-\frac{\frac{1}{2}\theta}{\omega_2^2-\omega^2+2j\xi_2\omega_2\omega} \tag{34}$$

Experimental data for each α are taken by actuating bimorphs separately under 1 V peak-to-peak voltage input, and the displacement response of each bimorph is measured for both actuation cases. Unknown model parameters for α are θ, ξ_1, and ξ_2. θ is determined by tuning to match with the experimental data. Then, ξ_1 and ξ_2 are varied to catch the resonant response. Thus θ, ξ_1, and ξ_2 are found as $\theta=170$ (mm/s^2)/V, $\xi_1=0.02$, and $\xi_2=0.0165$. Both experimental data and model results for each α FRF are given in Figs. 32 and 33.

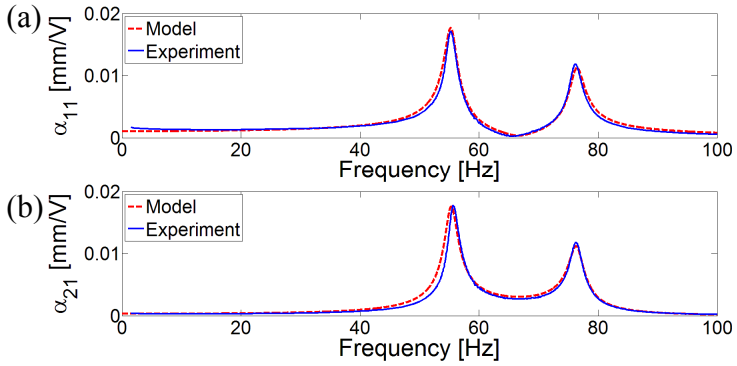

Figure 32. Peak-to-peak displacement response of the double bimorph measured at (a) point A, α_{11}, and (b) point C, α_{21} due to the actuation of (1) and (4) (Fig. 31) laminates out of phase.

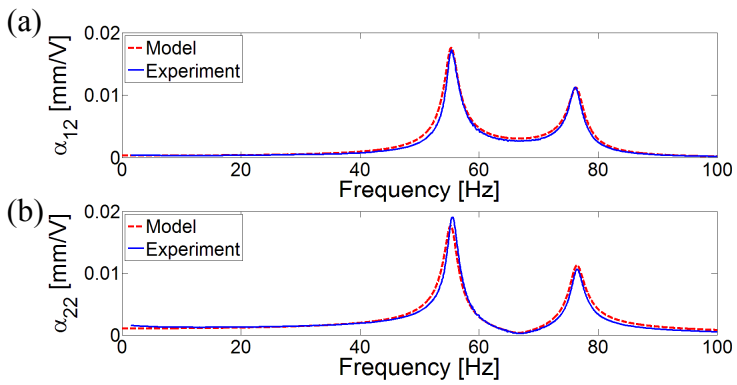

Figure 33. Peak-to-peak displacement response of the double bimorph measured at (a) point A, α_{12}, and (b) point C, α_{22} due to the actuation of (2) and (3) (Fig. 31) laminates out of phase.

After finding $[\alpha]$, displacement response can be found for any low voltage input by Eq. (32). Two cases are considered that are pure bending and pure twisting actuation cases. For pure bending case, bimorphs are actuated in phase with 1 V peak-to-peak voltage input, thus setting both V_1 and V_2 to 1 V in Eq. (32). On the other hand, for the pure twisting case, V_1 and V_2 are set to 1 V and -1 V respectively in order to create out of phase actuation. Figure 34 compares experimental results with the model for the pure bending case, and Fig. 35 presents the pure twisting results of both experimental data and model.

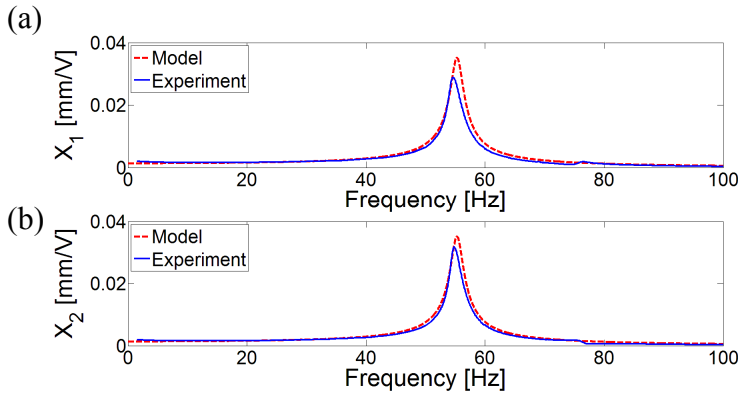

Figure 34. Peak-to-peak displacement response of the double bimorph measured at (a) point A, and (b) point C due to pure bending actuation case.

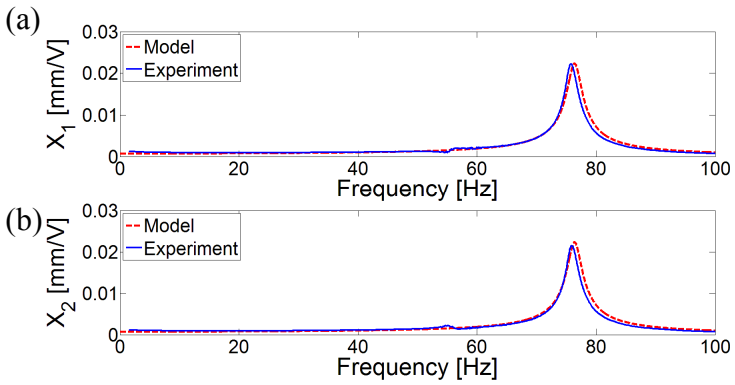

Figure 35. Peak-to-peak displacement response of the double bimorph measured at (a) point A, and (b) point C due to pure twist actuation case.

4.3 Stiffness identification for the double bimorph

The stiffness matrix of the double bimorph with narrow 0°-fiber MFC laminates is identified by the same procedure described in Section 3.4. First, the flexibility matrix, that is matrix $[A]$ in Eq. (35), is found. Then, stiffness matrix of the double bimorph is

determined by taking the reciprocal of the flexibility matrix. The displacement to force relation is

$$\begin{bmatrix} X_1 \\ X_2 \end{bmatrix} = \begin{bmatrix} A_{11} & A_{12} \\ A_{21} & A_{22} \end{bmatrix} \begin{bmatrix} F_1 \\ F_2 \end{bmatrix} \tag{35}$$

where X_1 and X_2 are the displacement responses that are presented in Fig. 36; F_1 and F_2 are the loads applied to the measurement points A and C (Fig. 30) respectively.

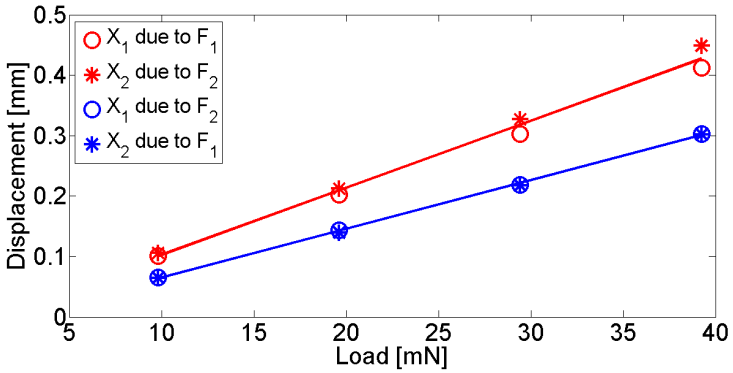

Figure 36. Experimental data of deflection versus different cases of loading for determining the flexibility matrix of the double bimorph cantilever. (Solid lines are curve fit to the average of experimental data related to diagonal and off-diagonal terms of the flexibility matrix).

Slopes of the curve fits to the experimental data of deflection in Fig. 36 form the short circuit flexibility matrix, $[A]$, for the double bimorph cantilever as,

$$[A] = \begin{bmatrix} 0.0104 & 0.0028 \\ 0.0028 & 0.0104 \end{bmatrix} (\text{mm/mN}) \tag{36}$$

Stiffness matrix is the inverse of the flexibility matrix,

$$[K]=\begin{bmatrix}103.6683 & -27.9107\\ -27.9107 & 103.6683\end{bmatrix}(\text{N/m}) \tag{37}$$

In section 4.2, the values of ω_a and ω_b were found. Therefore the stiffness matrix for unit mass (i.e. identity mass matrix) is

$$[K]'=\begin{bmatrix}\omega_a^2+\omega_b^2 & -\omega_b^2\\ -\omega_b^2 & \omega_a^2+\omega_b^2\end{bmatrix}=\begin{bmatrix}175650 & -54926\\ -54926 & 175650\end{bmatrix}(1/\text{s}^2) \tag{38}$$

, the element-wise ratio of K to the K' gives the lumped masses as,

$$\begin{aligned} m_1 &= \frac{103668.3}{175650} = 0.5902 \text{ g}\\ m_2 &= \frac{27910.7}{54926} = 0.5081 \text{ g}\end{aligned} \tag{39}$$

The double bimorph cantilever is assumed to be lumped equally, thus average of m_1 and m_2 forms the mass matrix,

$$[M]=\begin{bmatrix}0.5492 & 0\\ 0 & 0.5492\end{bmatrix}\text{ g} \tag{40}$$

which is the experimentally identified mass matrix in the assumed diagonal form.

4.4 Active stiffness change

Stiffness variation without shape change in the double bimorph structure due to the DC voltage input is investigated by the experimental setup shown in Fig. 37. Different constant DC voltage levels ranging from -400 V to 1400 V voltages are applied in phase to all MFC laminates such that positive DC voltage input acts as a tensile load while negative DC voltage input represents a compressive load on the overall structure.

For each DC voltage input, the velocity response on the tip due to base acceleration is measured. Base excitation is provided by electromagnetic shaker, and an accelerometer is attached to the clamp to measure the base acceleration simultaneously.

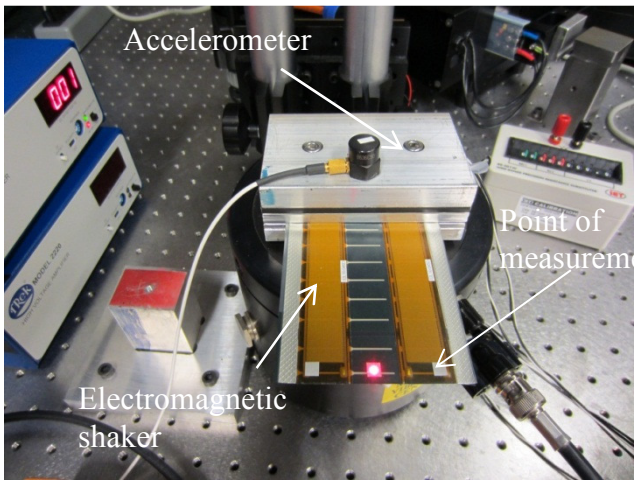

Figure 37. Experimental setup for measuring stiffness variation due to different DC voltage input to the double bimorph structure.

Figure 38 presents the velocity response – to – base acceleration FRFs of the double bimorph for different DC voltage levels. A single degree of freedom model is applied to the experimental data. In [21], the transmissibility function that gives the relative tip displacement to base displacement is expressed as,

$$T_{rel}(\omega,\zeta) = \frac{\mu_1 \omega^2}{\omega_1^2 - \omega^2 + j2\zeta\omega_1\omega} \tag{41}$$

where μ_1 is the correction factor to lumped parameter model solution based on distributed parameter model solution following Erturk and Inman [21]; μ_1 is given as 1.566 for the first mode of a uniform thin cantilever without a tip mass attachment.

The relative transmissibility function, $T_{rel}(\omega,\zeta)$, is related to the absolute tip velocity-to-base acceleration FRF by Eq. (42),

$$\frac{\partial w(x,t)/\partial t\big|_{x=L}}{-\omega^2 W_0 e^{jwt}} = \frac{1+T_{rel}(\omega,\zeta)}{j\omega} \tag{42}$$

where W_0 is the base displacement amplitude, $w(x,t)$ is the transverse displacement response at measurement point, and L is the distance between the measurement point and the clamped end. Therefore, the left hand side in Eq. (42) represents the experimental data in Fig. 38 only if it is multiplied by gravitational acceleration, g, because experimental data is taken per g. Hence, Eq. (42) is used to model the experimental data as a corrected single degree of freedom lumped parameter system.

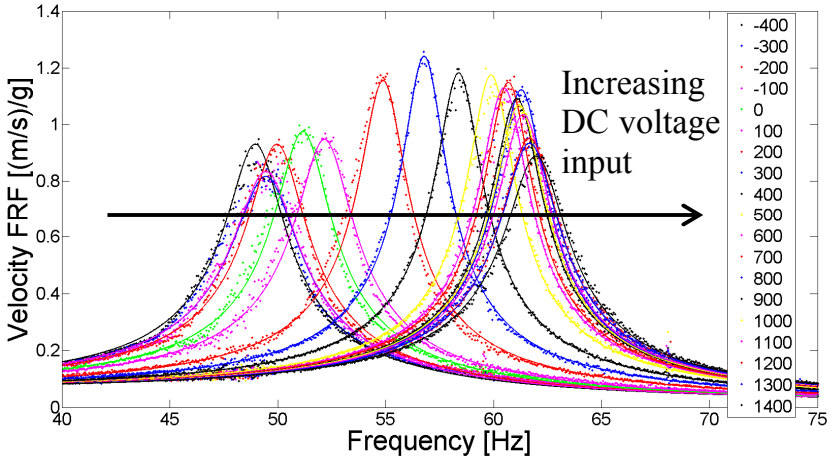

Figure 38. Tip velocity – to – base acceleration FRFs for each level of DC voltage input to the double bimorph to change the stiffness. (Solid lines are model results)

As the DC voltage input to MFC laminates increases from −400 V to 1400 V, the natural frequency changes significantly as a result of the stiffness change. Since the natural frequency is determined by the square root of the ratio of the effective stiffness to effective mass for this well separated bending mode, one can obtain stiffness of the structure for each DC voltage input from Fig. 38. Stiffness variation of the double bimorph with changing DC voltage level is presented in Fig. 39. It is observed in Fig. 39 that the change in stiffness of the structure becomes smaller out of −100 V and 600 V range. Approximately 60 % change in the stiffness takes place for the change of DC voltage from −400 V to 1400 V, and most of this variation occurs in the range of −100 V to 600 V. It can be suggested that the surface shear stress transmission from the MFC layers becomes saturated after certain voltage level.

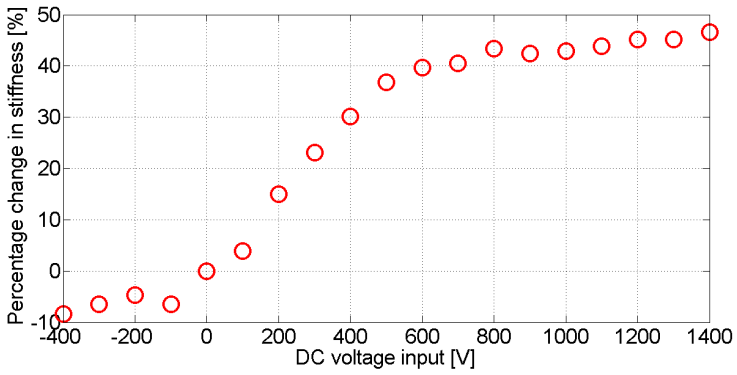

Figure 39. Percentage change in bending stiffness of the double bimorph for varying DC voltage input.

It is observed from Fig. 38 that the damping is also altered by changing DC voltage level and it deserves further investigation. After determining the stiffness for each DC voltage input, corresponding viscous damping ratios are extracted from model based on the peak amplitude of each FRF in Fig. 38. These damping ratios are plotted versus DC voltage input in Fig. 40. As it is seen in Fig. 40, viscous damping ratio follows a decreasing trend as the input DC voltage level increases up to 300 V, after which the viscous damping ratio increases. The bonding epoxy layer is expected to exhibit varying dissipative behavior with changing actuation voltage.

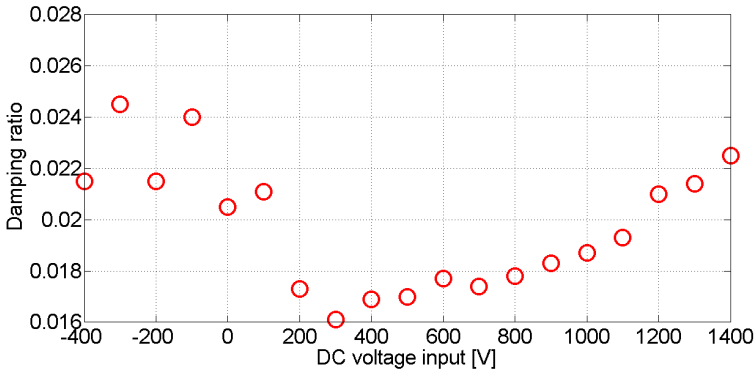

Figure 40. Extracted damping ratio values of the double bimorph for each level of DC voltage input.

4.5 High-voltage characterization of the double bimorph and nonlinear response

In order to characterize the dynamic response of the double bimorph sample, three actuation cases are studied: (1) pure bending, (2) pure twisting, and (3) combined actuation case. Forward frequency sweep experiments are conducted covering the first bending and twisting modes for a wide range of voltage levels.

4.5.1 Pure bending actuation

For the pure bending case, the laminates 1-2 are connected in phase and they are combined with the laminates 3-4 180° out of phase (Fig. 30). All laminates are connected in parallel. According to manufacturer, MFCs are safe to be actuated between -500 V and 1500 V without depolarization. Therefore, for the pure bending actuation case, an appropriate DC offset voltage is applied to increase the actuation range for demonstration. For instance, in order to apply 1200 V peak-to-peak voltage input, 200 V DC offset voltage is added to move voltage peaks from -600 V and 600 V to -400 V and 800 V.

Velocity response measurements, for the pure bending case, are taken only at the point B (central point – Fig. 30). Starting from peak-to-peak actuation input voltage of 5 V, several input voltages are applied until 1400 V, with a maximum frequency of 100Hz. Figure 41 presents results for pure bending case of the double bimorph. As can be seen in Fig. 41, the fundamental bending mode of the double bimorph architecture shows *softening* nonlinearity such that resonant frequency decreases from 56.6 Hz to 31.8 Hz as peak-to-peak voltage input increases from 5 V to 1400 V. The displacement versus voltage graph is presented in Fig. 42, where it is seen that the DC offset causes piecewise linear behavior.

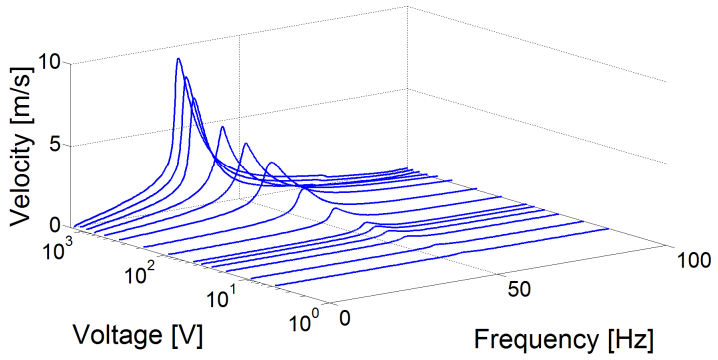

Figure 41. Peak-to-peak tip velocity frequency response curves measured at point B for pure bending actuation of the double bimorph (forward frequency sweep). The laminate pairs 1-2 (top) and 3-4 (bottom) in Fig. 30 are actuated 180° out of phase to create pure bending.

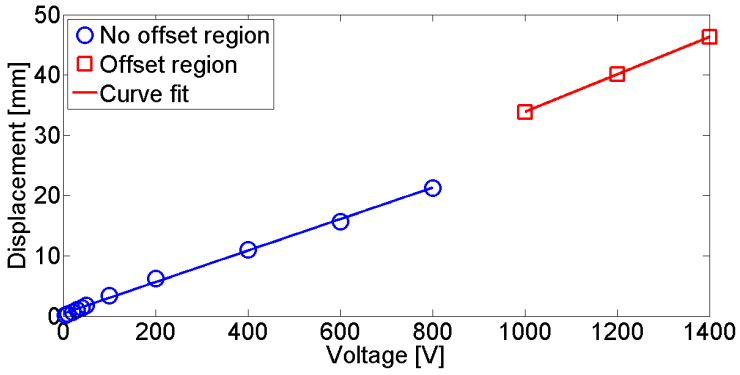

Figure 42. Resonant peak-to-peak displacement values for the bending mode measured at point B due to pure bending actuation of the double bimorph including the actuation range with positive DC offset for increased actuation voltage without depolarization (solid lines are curve fit).

4.5.2 Pure twist actuation

For the pure twist actuation case, the laminates 1 and 3 are connected in phase, and they are combined with the laminates 2 and 4 180° out of phase (Fig. 30). All laminates are connected in parallel. Figure 43 presents the velocity responses at points A, B, and C (Fig. 30) due to the pure twist actuation case. Figures 43a and 43c display that the double bimorph does quite symmetrical twisting, and it shows similar behavior as the asymmetric bimorph architecture such that the twist mode first softens, and then it shows *hardening* nonlinearity as well as the jump phenomenon. Velocity response at point B (Fig. 43b) is almost zero since it is the stationary point for the twisting motion.

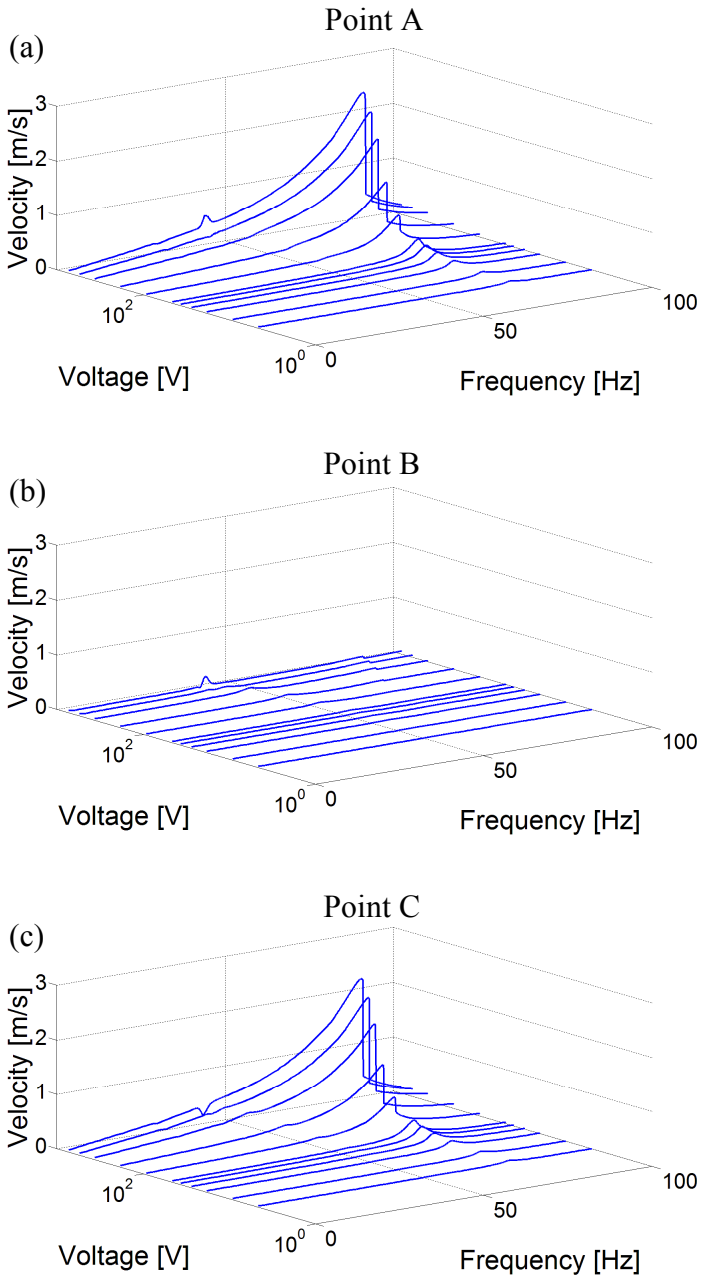

Figure 43. Peak-to-peak tip velocity frequency response curves measured at (a) point A, (b) point B, and (c) point C for pure twist actuation of the double bimorph (forward frequency sweep). The cross laminate pairs 1-3 and 2-4 in Fig. 30 are actuated 180° out of phase to create pure twist.

Figure 44 shows the resonant peak-to-peak displacements for the twist mode. Unlike the bending case, the displacement versus voltage curves for pure twisting actuation of the double bimorph changes with a nonlinear behavior.

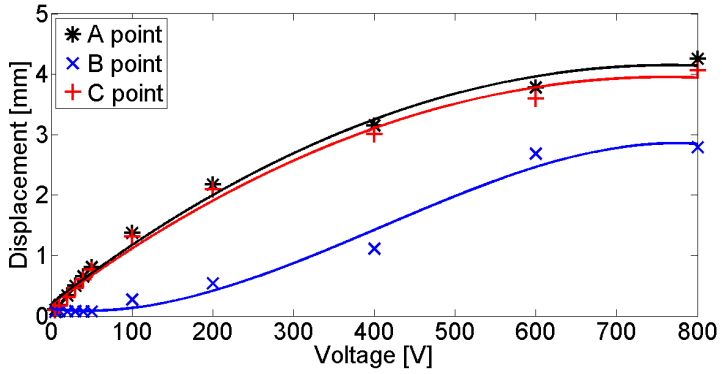

Figure 44. Resonant peak-to-peak displacement values for the twist mode measured at points A, B, and C due to pure twist actuation of the double bimorph (solid lines are curve fit).

4.5.3 Combined actuation

For the combined actuation case of the double bimorph, the MFCs 2, 3, and 4 are actuated in phase while the MFC 1 is actuated 180° out of phase (Fig. 30). In simplest terms to interpret this combined actuation mechanism, the MFCs at the bottom perform bending while the MFCs at the top are employed for twisting. Therefore, the double bimorph is actuated to do both bending and twisting. All laminates are connected in parallel.

As can be seen in Fig. 45, both bending and twisting are observed on the sample, except for point B, which is relatively stationary in twisting. With increasing voltage input, the resonant frequency of the bending mode decreased from 45.2 Hz to 37.3 Hz

(showing softening effect) while the resonant frequency of the twist mode increased from 72.2 Hz to 79.8 Hz (indicating hardening). Note that combined actuation case experiments are done with voltage inputs varying between 100 V and 600 V.

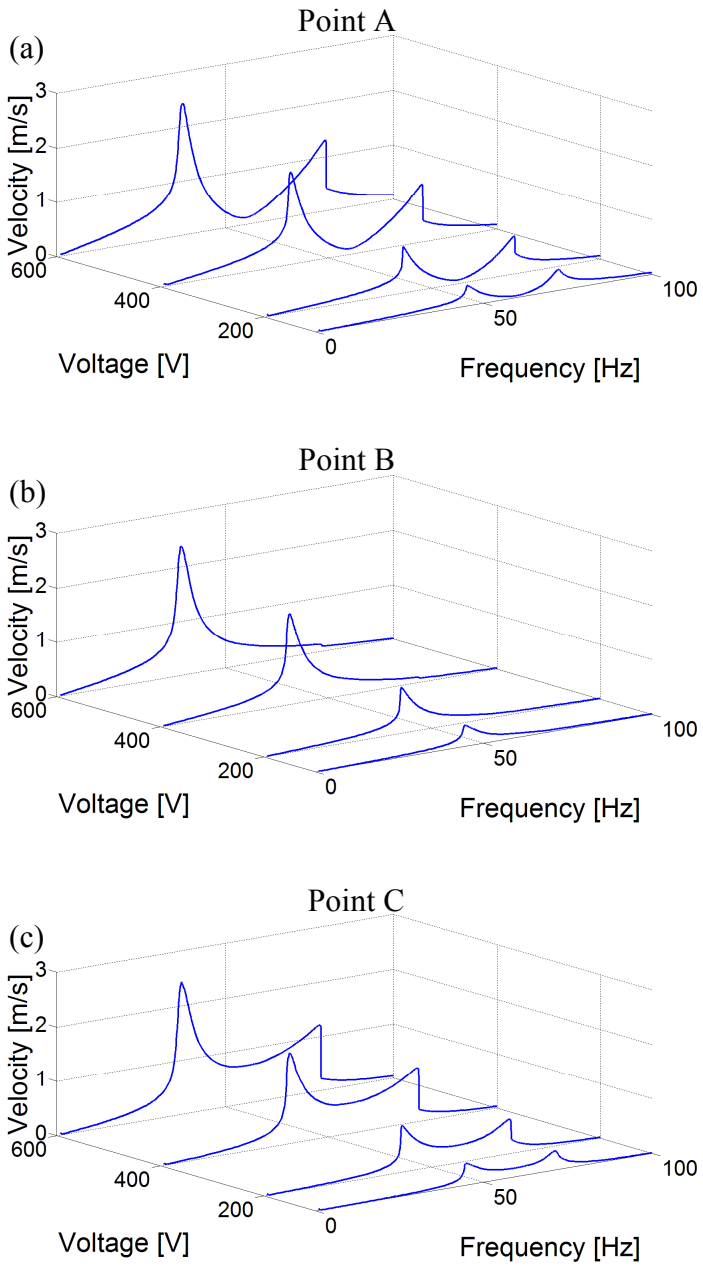

Figure 45. Peak-to-peak tip velocity frequency response curves measured at (a) point A, (b) point B, and (c) point C for combined actuation of the double bimorph with different peak-to-peak voltage input levels (forward frequency sweep). The MFCs 2, 3, and 4 are in phase while the MFC 1 is 180° out of phase during the simultaneous actuation.

Figure 46 displays the resonant peak-to-peak displacement values of the double bimorph sample for combined actuation. In addition, current consumption amplitudes for the combined actuation case experiments are given in Fig. 47.

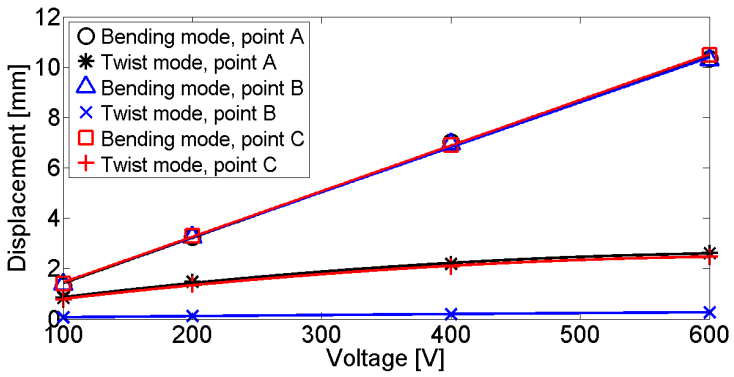

Figure 46. Resonant peak-to-peak displacement values for the bending and twist modes measured at points A, B, and C due to combined actuation of the double bimorph (solid lines are curve fit).

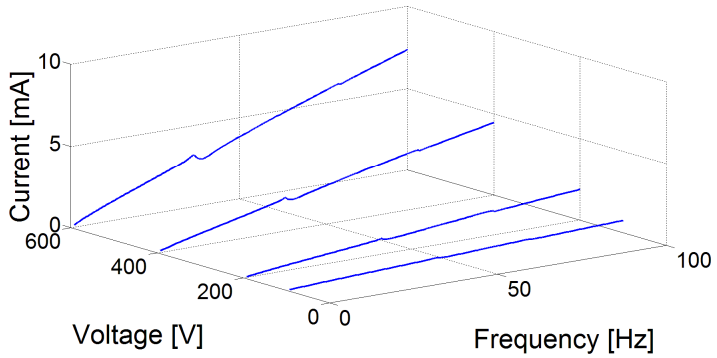

Figure 47. Frequency response curves of current amplitude for different peak-to-peak voltage levels due to combined actuation of the double bimorph (forward frequency sweep).

4.5.4 Flapping and twist angles

Displacement response at the first bending and twist resonance of the double bimorph in different actuation cases were presented before. Maximum flapping angle and twist angle for each different experimental case are calculated by using the displacement values and dimensions of the architecture. Flapping and twist angles are tabulated in Table 2. Flapping angle is calculated at the bending mode (BM), and twist angle is calculated at the twist mode (TM). Note that the data in Table 2 are from peak to peak values.

Table 2. Maximum flapping and twist angle results observed during actuation of the double bimorph.

Experiment Type	Frequency (Hz)	Voltage Input (V)	Flapping Angle (Degree)	Twist Angle (Degree)
Pure bending actuation	42.9 (BM)	600	11.8	0
	31.8 (BM)	1400	36.3	0
Pure twisting actuation	86.6 (TM)	600	0	8.7
	88.7 (TM)	800	0	9.8
Combined Actuation	37.3 (BM) 79.7 (TM)	600	7.9	6.0

Combined actuation of the double bimorph is performed under 600 V input voltage at maximum. Therefore, there are two sets of data, which are for 600 V and maximum input voltage ever tried, for separate actuation cases of the double bimorph. For the double bimorph, the combined actuation provides both bending and twisting although the resulting values are lower than the separate actuation cases because four

MFC laminates are grouped into two to make either twist or bending. Therefore, the combined actuation case is not the linear sum of the separate actuation cases, but it divides the performance into both bending and twisting. In addition, combined actuation results in slightly lower resonant frequencies as in the asymmetric bimorph case.

CHAPTER 5

WIND TUNNEL EXPERIMENTS FOR BENDING-TWISTING COUPLING OF A FLEXIBLE DOUBLE BIMORPH

Similar to double bimorph sample with the solar energy harvester substrate, a flexible double bimorph sample is made by using a rubber substrate to be used in wind-tunnel characterization experiments. The flexible double bimorph sample is first experimentally characterized for different peak-to-peak actuation voltage inputs ranging from 5 V to 800 V for zero airflow speed. Then, for the actuation input voltages between 200 V and 800 V, the response of the flexible double bimorph is studied under different wind speeds between 10 kph and 90 kph (where kph stands for kilometer per hour).

5.1 Structural properties of the flexible double bimorph

The double bimorph with flexible rubber substrate (DB-FRS) sample is built by bonding four narrow 0° MFC laminates (M8507-P1, Smart Material Corp.) onto an abrasion-resistant natural latex rubber (85995K15, McMaster-Carr). The substrate has a thickness of 0.30 mm, and it is chosen to be flexible as well as having a good tear-resistance. Each MFC has a thickness of 0.31 mm and capacitance of 1.4nF. Chordwise distance between the bimorphs is 3 cm, and overall thickness of each bimorph is 0.98 mm which has two MFCs, the substrate and high-shear strength epoxy layers which is used for bonding process that is described in the section 3.1. Two points of measurement A, and B (Fig. 48a) are used to capture both bending and twist modes as well as the degree of symmetry of the sample. The distance of measurement points to the clamp is 79.5 mm, and the chordwise distance between them is 44.2 mm. Overall sample weighs 6.4 g. Each

MFC is numbered from 1 to 4 (Figs. 48a and 48b) such that 1 and 3 MFCs form the bimorph at point A side; 2 and 4 MFCs make the bimorph at point B side. In clamped conditions, active region area is 1085 mm^2.

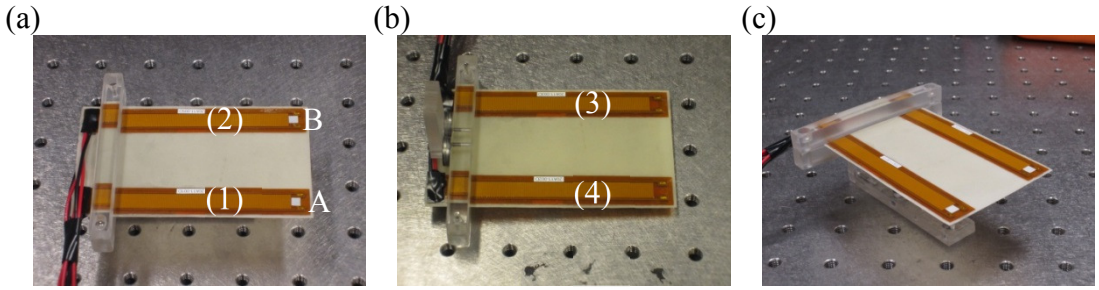

Figure 48. The double bimorph with flexible rubber substrate: (a) top view along with the measurement points and labels for MFCs (b) bottom view showing the labels for MFCs (c) isometric view.

5.2 Experimental setup and measurements

The experimental characterization of nonlinear behavior of DB-FRS is done with the same experimental setup that is described in Section 3.2. The only difference in this chapter is that only two points of measurement are used. After determining the nonlinear behavior of DB-FRS for different input voltage levels, response of the sample is further investigated in the wind tunnel which is presented in Fig. 49. The desktop wind tunnel (Jet Stream 500, Interactive Instruments Inc.) is used to create a wind speed between 10 kph and 90 kph, and for every wind speed the flexible double bimorph is actuated in pure bending case, pure twisting case, and combined case by a peak-to-peak actuation voltage input changing from 200 V to 800 V. Velocity response at points A and B are measured by a single-point laser vibrometer (Polytec OFV-505 with OFV-5000 controller). A close

up view of the wind tunnel experimental setup is given in Fig. 49b which exhibits the wind speed direction. Due to the wind speed direction and the position of the fixture, measurement point A is along the leading edge while point B is on the trailing edge.

(a) (b)

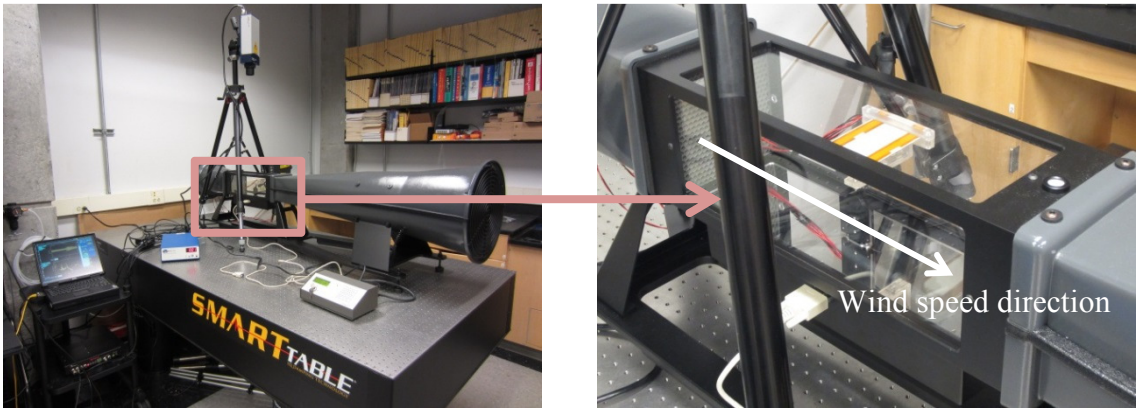

Figure 49. Experimental setup for wind tunnel experiments: (a) general view (b) close up view presenting the test section and wind speed direction.

5.3 High-voltage characterization of the nonlinear behavior

Nonlinear behavior of DB-FRS is experimentally characterized for peak-to-peak actuation voltage levels ranging from 5 V to 800 V with a sweeping frequency from 10 Hz to 60 Hz.

5.3.1 Pure bending actuation

For pure bending actuation case, MFCs labeled as 1 and 2 in Fig. 48 are actuated 180° out-of-phase with the MFCs that are labeled as 3 and 4. As can be seen in Fig. 50, velocity responses at measurement points A and B are identical to each other, which prove that the sample is quite symmetric. Bending mode resonant frequency decreases

from 32.5 Hz to 29.6 Hz as the voltage input level increases from 5 V to 800 V, which is due to the *softening* nonlinearity. Resonant peak-to-peak displacement responses at points A and B are given in Fig. 51. Displacement responses at points A and B are quite similar and they linearly increase by increasing input voltage level.

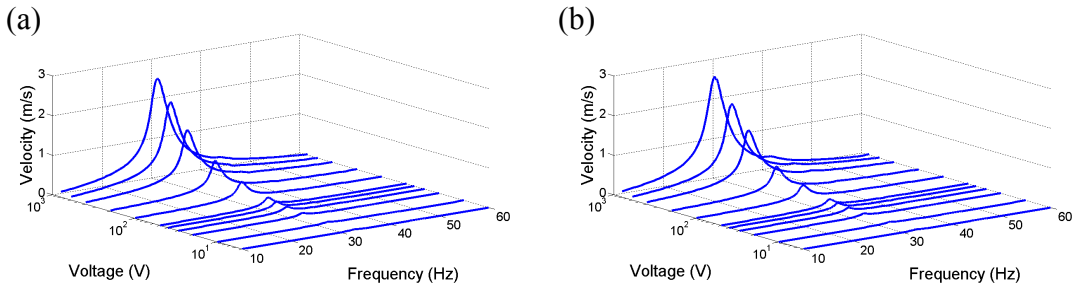

Figure 50. Peak-to-peak tip velocity frequency response curves measured at (a) point A (b) point B for the pure bending actuation case of DB-FRS (forward frequency sweep).

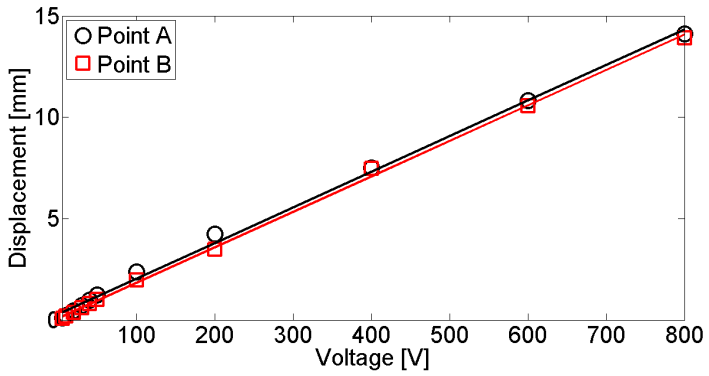

Figure 51. Resonant peak-to-peak displacement values for the bending mode measured at points A and B due to pure bending actuation case of DB-FRS (solid lines are curve fit).

5.3.2 Pure twist actuation

Twist motion is created by actuating the MFCs that are labeled as 1 and 3 (Fig. 48) 180° out-of-phase with the 2 and 4. In other words each bimorph is actuated 180°

out-of-phase relative to other bimorph. For twisting actuation, velocity responses at points A and B are given in Fig. 52. For the twist mode, piezoelectric nonlinearities are dominant from 5 V to 50 V such that resonant frequency drops from 45.3 Hz to 44.6 Hz due to *softening* effect. After 50 V, *hardening* effect is observed such that resonant frequency increases from 44.6 Hz to 49.9 Hz due to geometric nonlinearities. In addition, jump is observed after 200 V actuation level. Resonant peak-to-peak displacement responses at points A and B are given in Fig. 53. Similar displacement amplitudes are observed at points A and B. Note that there is 180° phase difference between the responses at points A and B due to the actuation case.

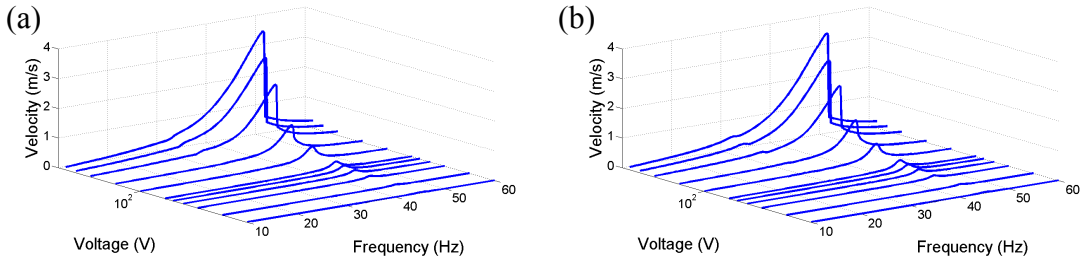

Figure 52. Peak-to-peak tip velocity frequency response curves measured at (a) point A and (b) point B for the pure twist actuation case of DB-FRS (forward frequency sweep).

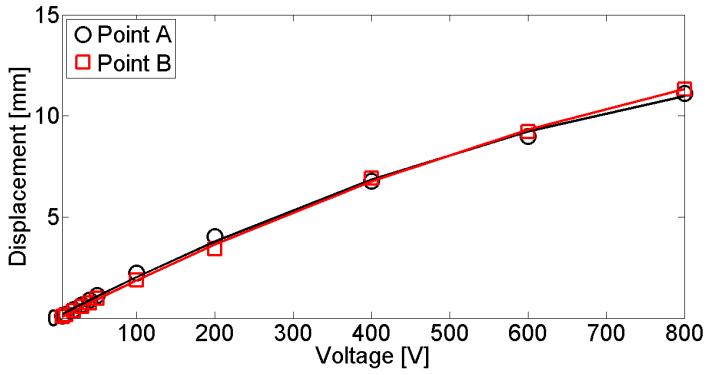

Figure 53. Resonant peak-to-peak displacement values for the twist mode measured at points A and B for the pure twist actuation case of DB-FRS (solid lines are curve fit).

5.3.3 Combined actuation

For the combined actuation case, the MFCs 2, 3, and 4 are actuated in phase while the MFC 1 is actuated 180° out of phase (Fig. 48). Hence, the MFCs at the bottom do bending, and the MFCs at the top are employed for twisting. As it seen in Fig. 54, both bending and twist modes are observed for the combined actuation case. *Softening* and *hardening* nonlinearities are again observed for the bending and twist modes, respectively. Since bending and twisting modes are well-separated for this actuation case, both modes can be exploited based on specific needs.

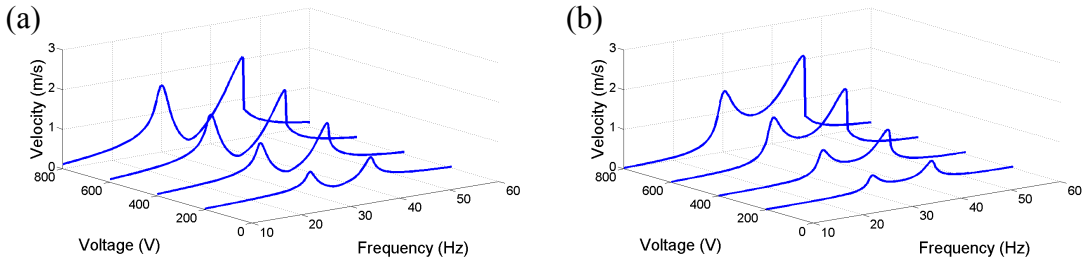

Figure 54. Peak-to-peak tip velocity frequency response curves measured at (a) point A and (b) point B for the combined actuation case of DB-FRS (forward frequency sweep).

Peak-to-peak displacement responses at both bending and twisting mode resonant frequencies are given in Fig. 55. Different from asymmetric bimorph and double bimorph with solar film substrate (DB-SFS), bending mode and twist mode displacement response amplitudes are close to each other for this DB-FRS. This is thought to be due to the elastic rubber substrate. Essentially the individual bimorphs as single degree-of-freedom systems are connected through a soft component.

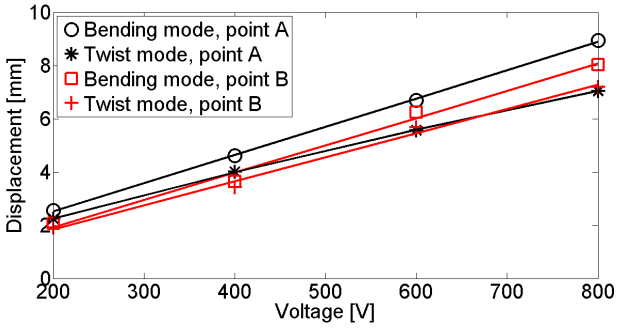

Figure 55. Resonant peak-to-peak displacement values for the bending and twist modes measured at the points A and B due to combined actuation case of DB-FRS (solid lines are curve fit).

Peak-to-peak current consumption amplitudes for the combined actuation case on DB-FRS are given in Fig. 56. Current consumption of this sample is lower than the current consumption levels of DB-SFS and asymmetric bimorph because this sample has the lowest active region area which has the piezoelectric fibers.

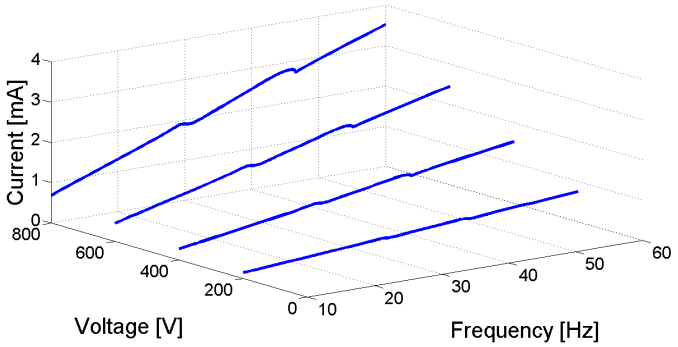

Figure 56. Frequency response curves of current consumption amplitude for different peak-to-peak voltage levels due to combined actuation case of DB-FRS (forward frequency sweep).

5.3.4 Flapping and twist angles

For the DB-FRS sample, maximum flapping and twist angles for each different experimental case are calculated and tabulated in Table 3. Note that, flapping angle is calculated at the bending mode (BM) resonance, and twist angle is calculated at the twist mode (TM) resonance.

Comparing the DB-FRS architecture with the DB-SFS (see Tables 2 and 3), DB-FRS has lower resonant frequencies. Moreover, the DB-FRS architecture has higher twist angle results than the DB-SFS architecture. This is due to the flexible substrate that DB-FRS has. However, DB-SFS has higher response in flapping because DB-SFS has wider active region (thus more piezo-fibers).

Table 3. Maximum flapping and twist angle (peak-to-peak) results observed during the actuation of the DB-FRS

Experiment Type	Frequency (Hz)	Voltage Input (V)	Flapping Angle (Degree)	Twist Angle (Degree)
Pure Bending Actuation	29.6 (BM)	800	10	0
Pure Twist Actuation	49.9 (TM)	800	0	14.2
Combined Actuation	29.9 (BM) 46.4 (TM)	800	6.1	9.1

5.4 Wind tunnel experiments under dynamic actuation

Dynamic response of DB-FRS is also investigated under different airflow speeds by using the experimental setup that is described in Section 5.2. Four input voltage levels are studied which are varied between 200 V to 800 V peak to peak. Similar to the previous experimental studies in this thesis, pure bending, pure twist, and combined actuation cases are studied for each set of voltage levels. For every actuation case and input voltage level, wind speed is varied from 0 kph to 90 kph.

5.4.1 Pure bending actuation

For pure bending actuation case, the velocity response of DB-FRS is presented in Fig. 57. Each row in Fig. 57 differs in terms of the voltage input level. Comparing the rows in Fig. 57, the amplitude of the response increases as the voltage input level increases. The two columns in Fig. 57 refer to the points of measurement such that the first column is the measurements at point A, which is the leading edge, and the second column refers to the measurements at point B that is the trailing edge.

Variation in the wind speed changes the total damping (structural and aerodynamic) such that the amplitude of the response first decreases, i.e. until the wind

speed of 50 kph for the input voltage level of 200 V. Then the amplitude of response increases. Hence, for 200 V actuation, aerodynamic damping first increases making a peak at 50 kph, then it decreases. This typical trend of the aerodynamic damping in classical flutter was recently reported for aeroelastic energy harvesting using piezoelectric cantilevers [68]. The highest aerodynamic damping is observed at 60 kph for higher input voltage levels. With increasing flow speed the bending and twisting modes are coupled around the frequency of 33 Hz in the sense of classical aeroelastic flutter. With further increase of the airflow speed the bending-twisting response continues and is bounded due to nonlinearities in the system (i.e. it is not divergent flutter). Since the flutter motion has both bending and twisting motions along with a relative phase, the amplitude of response at the trailing edge is higher than leading edge, which is observed by comparing the two columns in Fig. 57.

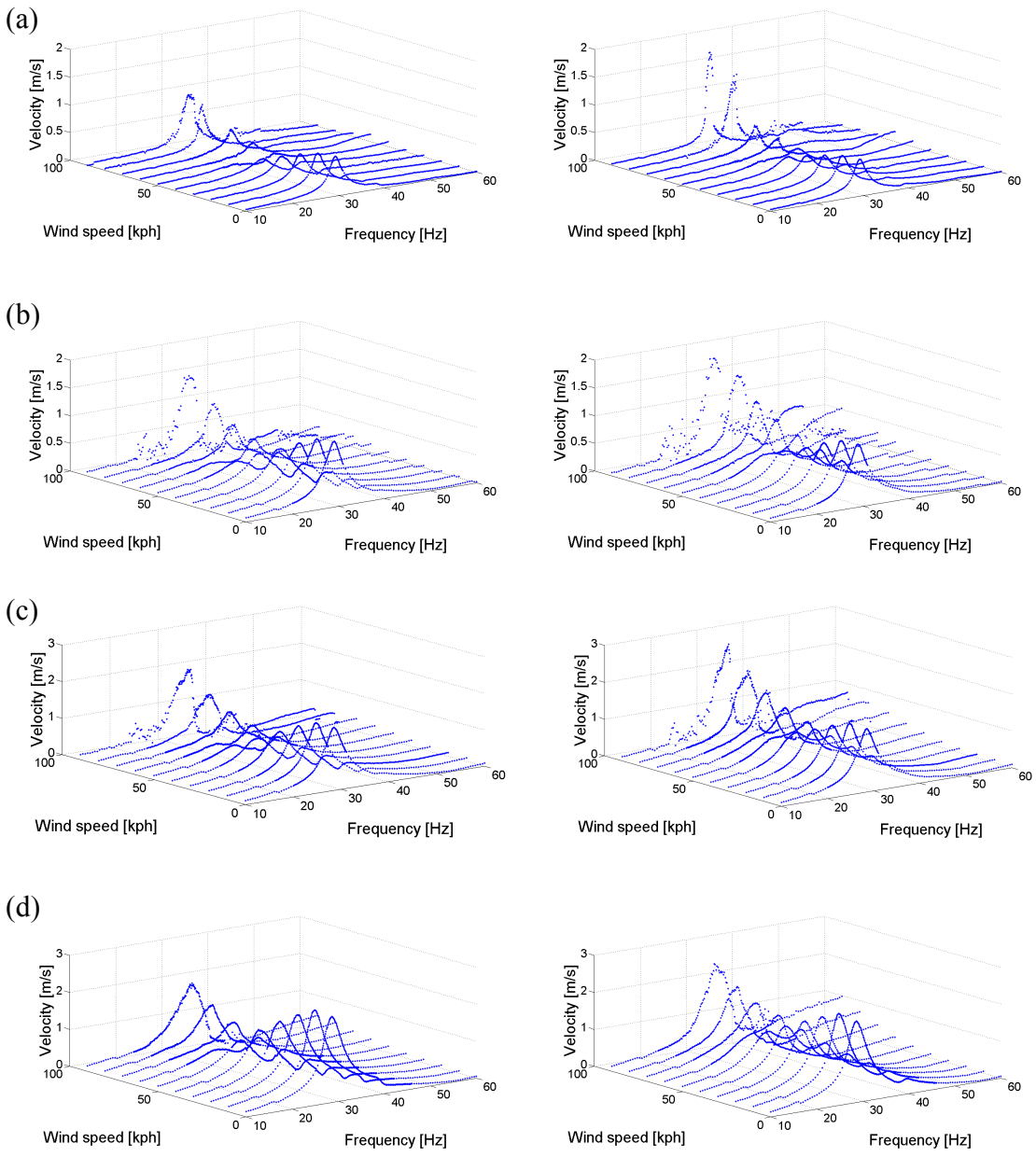

Figure 57. Wind tunnel tests on DB-FRS for pure bending actuation case with peak-to-peak input voltage levels of (a) 200 V, (b) 400 V, (c) 600 V, and (d) 800 V (the first column refers to the measurements at point A, leading edge; and the second column refers to the measurements at point B, trailing edge).

5.4.2 Twist actuation

Similar aerodynamic damping behavior is observed for twisting actuation case as well. Aerodynamic damping increases until 60 kph of wind speed, resulting in the lowest amplitude of velocity response at that wind speed (Fig. 58). Due to decreasing aerodynamic damping after the peak at 60 kph, velocity amplitude increases with pronounced flutter motion. Note that, the responses at the leading edge and the trailing edge are same in amplitude when there is no wind speed. While the wind speed is increased so that flutter motion becomes dominant, the difference between the amplitudes of the response at the leading edge and trailing edge increases. In addition, the resonant frequency keeps reducing as the wind speed increases since the flutter mode occurs at a frequency between the bending and twisting resonant frequencies.

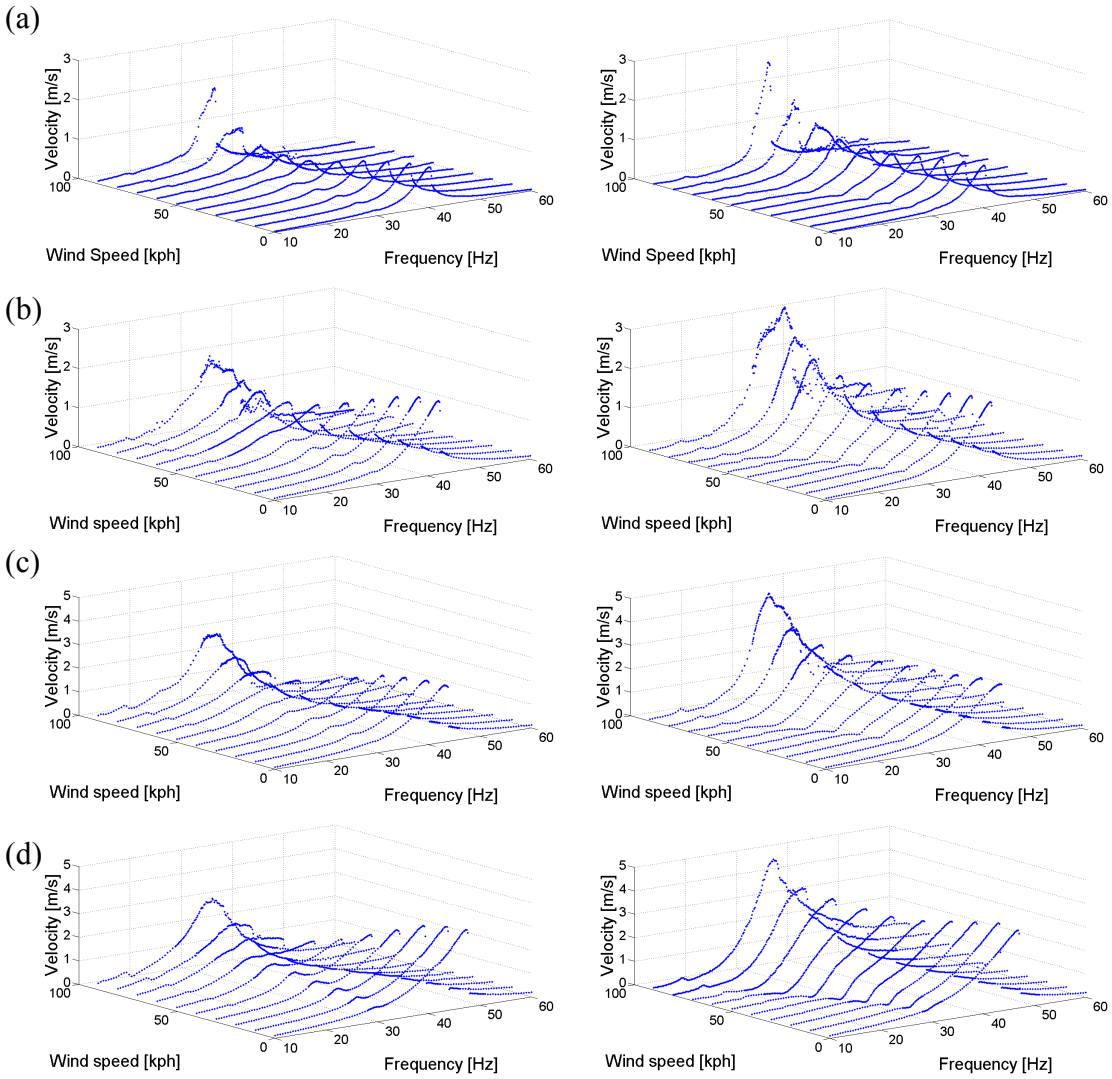

Figure 58. Wind tunnel tests on DB-FRS for the twisting actuation case with peak-to-peak input voltage levels of (a) 200 V, (b) 400 V, (c) 600 V, and (d) 800 V, (the first column refers to the measurements at point A, leading edge; and the second column refers to the measurements at point B, trailing edge).

5.4.3 Combined actuation

Since it is possible to observe both bending and twisting modes in combined actuation case, wind tunnel tests for this actuation case clearly demonstrate the effect of increasing wind speed on the electroelastic behavior (Fig. 59). The bending mode

response amplitude decreases, and it couples with the twisting mode while the twist mode resonant frequency decreases. Finally, the sample shows flutter motion between the structural bending and twisting mode frequencies, approximately at 33 Hz.

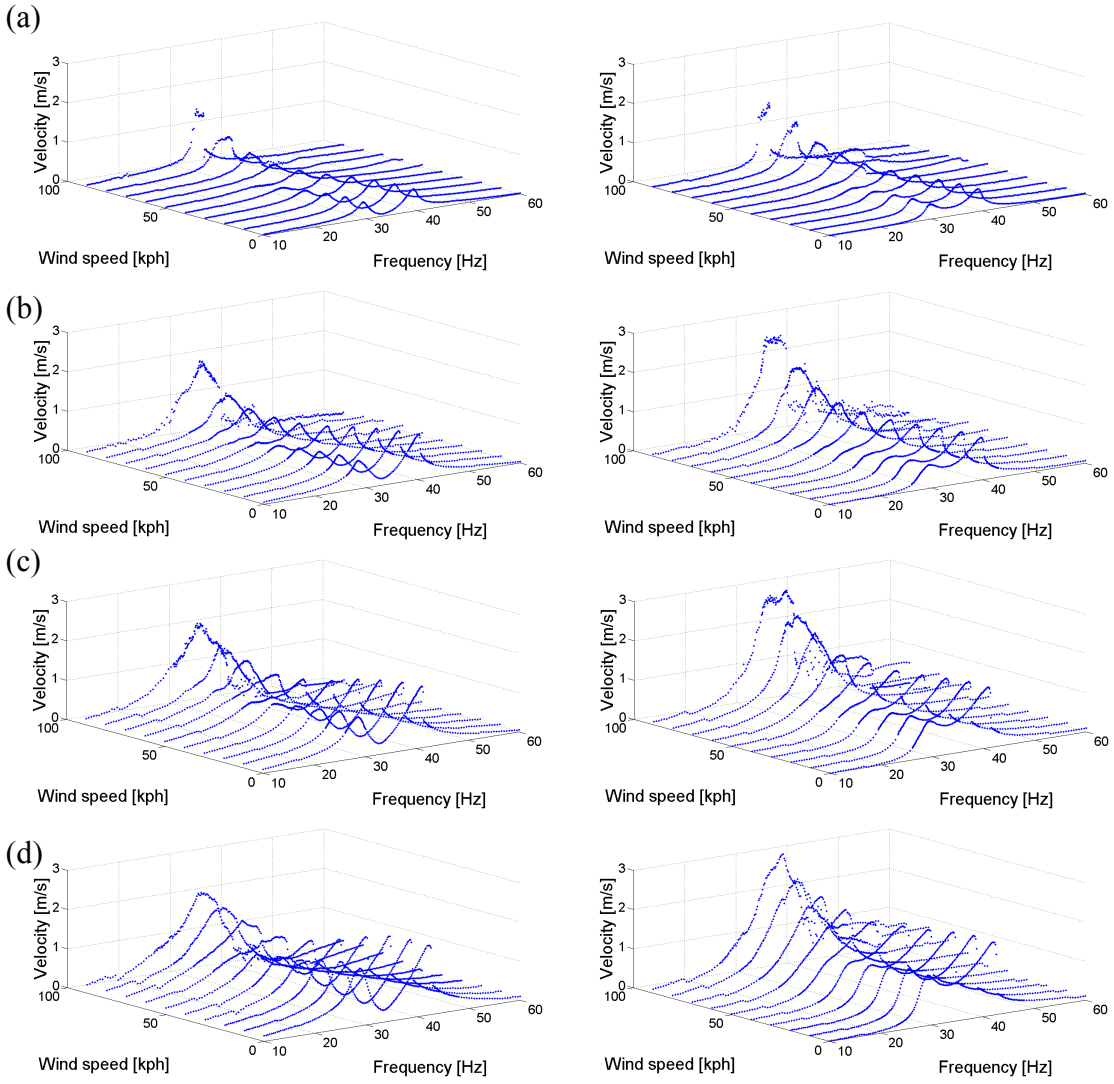

Figure 59. Wind tunnel tests on DB-FRS for the combined actuation case with peak-to-peak input voltage levels of (a) 200 V, (b) 400 V, (c) 600 V, and (d) 800 V (the first column refers to the measurements at point A, leading edge; and the second column refers to the measurements at point B, trailing edge).

CHAPTER 6

TRIPLE BIMORPH AND AQUATIC THRUST GENERATION

6.1 Triple bimorph caudal fin with narrow 0°-fiber laminates

Triple Bimorph Piezoelectric Caudal Fin (TBPCF) architecture (Fig. 60) is based on three bimorphs made of six narrow 0°-fiber MFCs (M8507P1 – Smart Material Corp.) bracketing a continuous natural latex rubber substrate (85995K13 – McMaster-Carr). Bonding of the MFCs onto the rubber substrate is done by using high shear strength epoxy (3M DP 460) in a vacuum bonding process (details are in section 3.1). Each of the MFCs has 85 mm x 7 mm active region dimensions, which includes piezoelectric fibers, and the total area of the MFC is 103 mm x 16.5 mm. Note that the electrodes of each MFC are covered by polyester sheets for improving water proof behavior (in the custom fabrication process of the manufacturer). The capacitance of each MFC is measured to be 2.4 nF. The thickness for the latex rubber substrate is 0.2 mm. The clamped length of each bimorph is 84 mm, and the total thickness including the MFCs, substrate and the epoxy is around 1 mm in the bimorph regions of the TBPCF. Further dimensional details of the fin are given in Fig. 60b. Three points of measurement A, B, and C are determined along the longitudinal centerline of the bimorphs, and each point is 77.5 mm away from the clamped end. Fabricated TBPCF and lateral velocity measurement points with reflector tape attachments are shown in Fig. 60c.

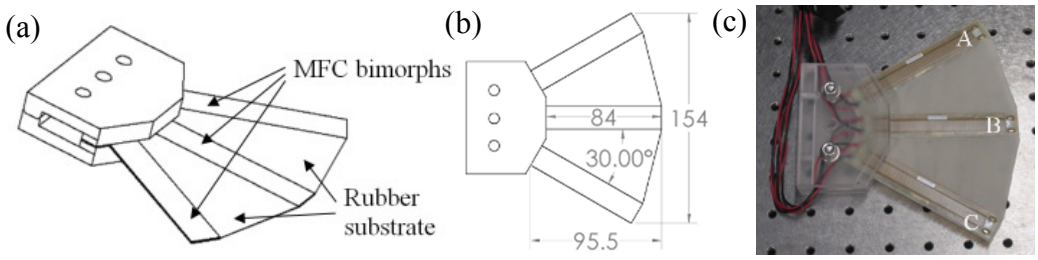

Figure 60. (a) Isometric view and (b) side view (all dimensions are in mm) of the 3-D TBPCF model composed of 3 narrow MFC bimorphs sharing a rubber substrate; (c) picture of the fabricated TBPCF and its clamp along with the tip velocity measurement points (A, B, and C).

6.2 Details of the experimental setup

The experimental setup to characterize the mean thrust output for the actuation of the TBPCF is presented in Fig. 61. As can be seen in Fig. 61a, four single-point laser vibrometers are used. One of them (Polytec OFV-505 with OFV-5000 controller with a displacement decoder) measures the mean thrust output (correlated to constrained head displacement of the fin) as displayed in Fig. 61b, and the other three laser vibrometers (Polytec PDV-100) measure the lateral velocity response at points A, B, and C as shown in Fig. 61c. Actuation signals sourced from the data acquisition system are amplified by high voltage amplifiers (Trek 2220). Mean thrust output and velocity responses at the measurement points A, B, and C are recorded by a data acquisition system (Siglab 20-42). The front view and the side view of the aquarium are given in Figs. 61b and 61c respectively. Mirrors are used to reflect the laser beam as required depending on the location of the laser vibrometers in the experimental setup.

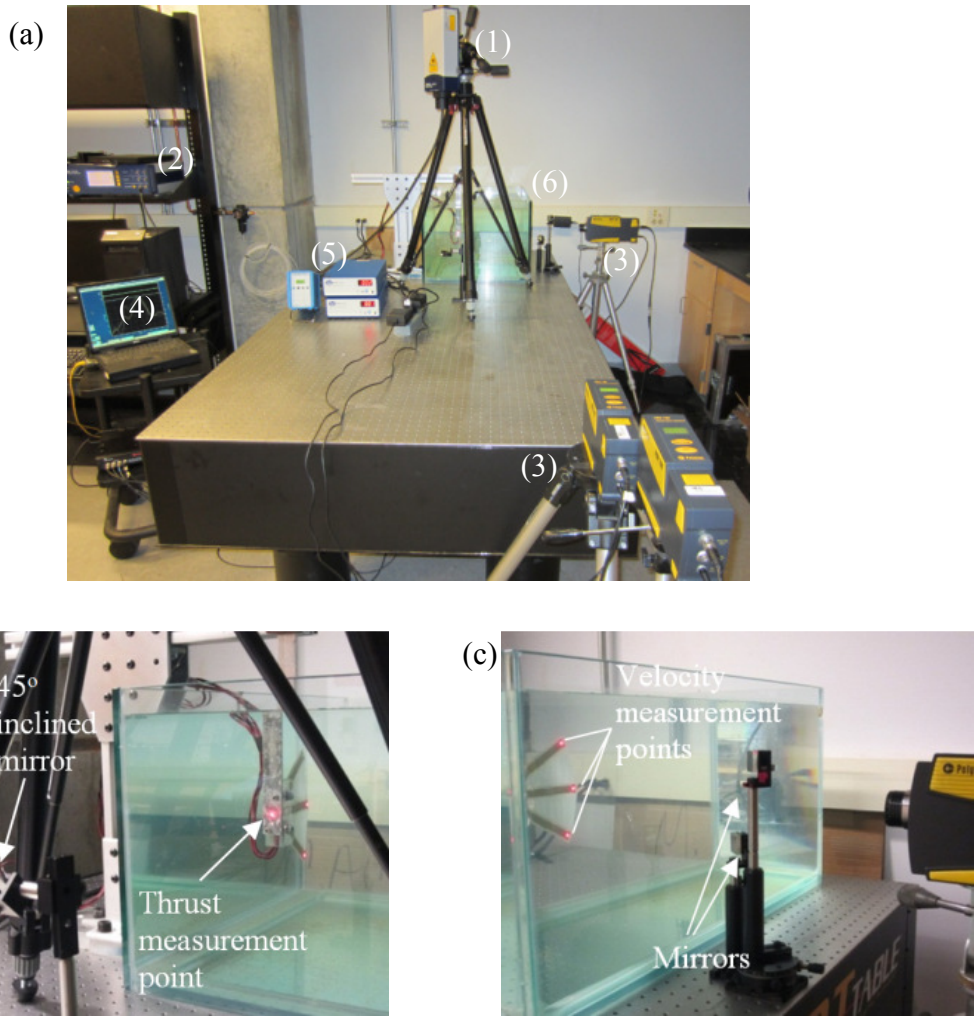

Figure 61. (a) Overview of the experimental setup: (1) laser vibrometer and (2) its displacement decoder used for thrust measurement, (3) laser vibrometers used for vibration of points A, B, and C (see Fig. 60c) on the TBPCF, (4) signal generation and data acquisition system, (5) high-voltage amplifiers, and (6) water tank; (b) close-up view of the water tank showing the thrust measurement point and the corresponding mirror to reflect the laser beam; (c) close-up view of the water tank showing velocity measurement points and mirrors used to reflect the laser beams.

6.3 Calibration for thrust measurement

In order to measure the mean thrust output, elastically constrained deflection of the TBPCF is measured during the actuation experiments. Therefore it is required to determine the force-deflection relationship, in other words the stiffness of the aluminum

cantilever beam to which the TBPCF is attached from its clamp. Fig. 62a presents the experimental setup for measuring the stiffness of the cantilever beam in air. Indicated by F in Fig. 62b, various loads are applied to the mid-point of the section where the clamp is attached to the beam, and the corresponding deflection of the beam is measured at the point indicated by δ. Figure 62c presents the experimental data of the force applied to the cantilever beam versus the resulting deflection. The solid line in Fig. 62c is the curve fit to the experimental data whose slope is the stiffness of the cantilever. The stiffness of the cantilever is found to be 6570 N/m, which is used for determining the mean thrust output from the deflection caused by the actuation of the TBPCF in the underwater experiments (since the hydrostatic loads cancel out). It is important to note that the fixture is checked by a instrumented hammer excitation (impact testing) to ensure that its natural frequencies are not within the range of underwater frequencies of interest. Therefore the thrust resultant due to underwater actuation of the TBPCF is in the quasistatic region of the statically calibrated aluminum cantilever.

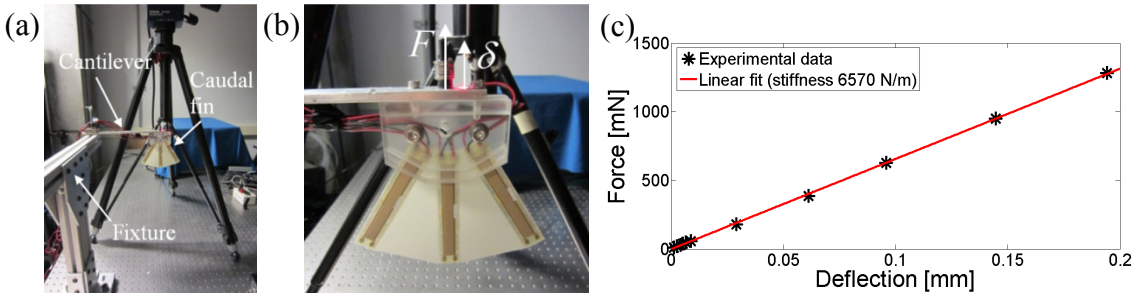

Figure 62. Calibration of the thrust measurement system (a) experimental setup used for determining the stiffness of the cantilever beam for thrust measurement; (b) close-up view showing the point of applied force and the point of deflection; (c) calibration line showing the applied force versus deflection of the horizontal cantilever beam.

6.4 Actuation cases: flat, cup, and rolling

Six different cases of actuation on the TBPCF are investigated. Properties of the actuation cases are given in Table 4. The first actuation case, case 1, is the "flat" case in which all bimorphs are actuated with the same signal that is 800 V peak to peak. Actuation cases from case 2 to 5 can be described as "cup" in which actuation signal inputted to bimorph B is different than bimorphs A and C in order to create a cup like shape at the TBPCF. Signal difference herein is either amplitude difference or phase difference. The last actuation case is "rolling" in which TBPCF has both bending and twist motions due to the fact that all bimorphs are actuated with different voltage amplitudes (in particular, one of the bimorphs is not actuated in this last case).

Table 4. Voltage and phase levels for the different actuation cases applied to the TBPCF

Actuation Cases	Actuation Voltage (V) (peak-to-peak)			Phase Difference of B relative to A and C (Degree)
	Bimorph A	Bimorph B	Bimorph C	
Case 1	800	800	800	0
Case 2	800	400	800	0
Case 3	800	0	800	0
Case 4	800	400	800	180
Case 5	800	800	800	180
Case 6	0	400	800	0

Figure 63a is the side view of the TBPCF underwater showing the labels of velocity measurement point for each narrow bimorph (A, B, and C). Figure 63b presents the schematic of the actuation cases observed from the rear view. Each colored rectangle represents the position of the corresponding bimorph, and the white slender rectangle

represents the central line (equilibrium). Light blue arrows indicate actuation is from peak to peak.

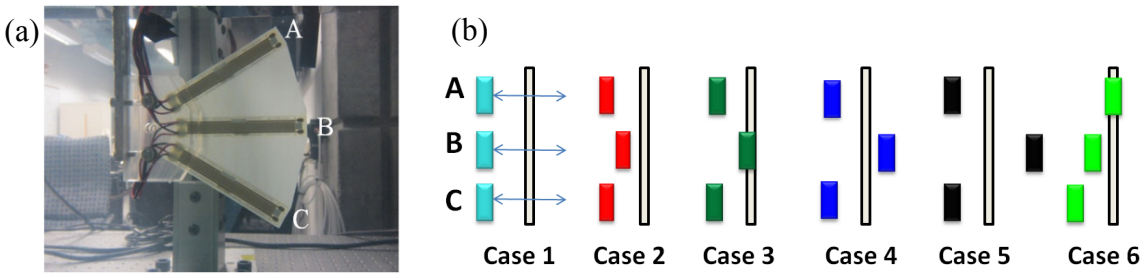

Figure 63. Underwater actuation experiments: (a) side view of the TBPCF showing labels for each bimorph; (b) schematics describing the actuation cases (rear view) for the intended motion patterns.

6.5 Velocity and phase histories for different actuation cases

In this section, dynamic underwater response of the TBPCF to the aforementioned actuation cases is discussed in terms of general trends, leaving the important numerical results to the next section. Discussion herein includes the velocity responses of each bimorph as well as the mean thrust resultants.

6.5.1 Case 1: "flat" actuation

The first actuation case of the TBPCF is the actuation of each bimorph with 800 V peak to peak. Figure 64a shows the velocity response versus frequency of the actuation signal due to actuation case 1. As seen in Fig. 64a, the velocity responses of bimorphs A and C are quite similar. However; velocity response of bimorph B is different than the other bimorphs for higher frequencies of actuation, although all bimorphs are actuated by the same voltage. This is expected to be due to the asymmetries of the TBPCF; specifically note that bimorphs A and C are oriented 30° with respect to the horizontal

axis (Fig. 63a). Importantly TBPCF behaves as a single-degree-of-freedom system within the range of measurement; and the natural frequency of this mode, roughly the "flat mode", is around 11 Hz.

Fig. 64b is the mean thrust result graph of the TBPCF subjected to the actuation case 1. Comparing Fig. 64a and 64b, it can be observed that thrust resultant curve follows similar pattern with the velocity response of bimorph B. For the same frequency range, highest mean thrust is obtained at 10.75 Hz. Therefore simultaneous velocity response of each bimorph at this frequency of interest is investigated in Fig. 64c. It is observed that the velocity responses of bimorphs A and C are very similar and they slightly differ from the velocity response of bimorph B.

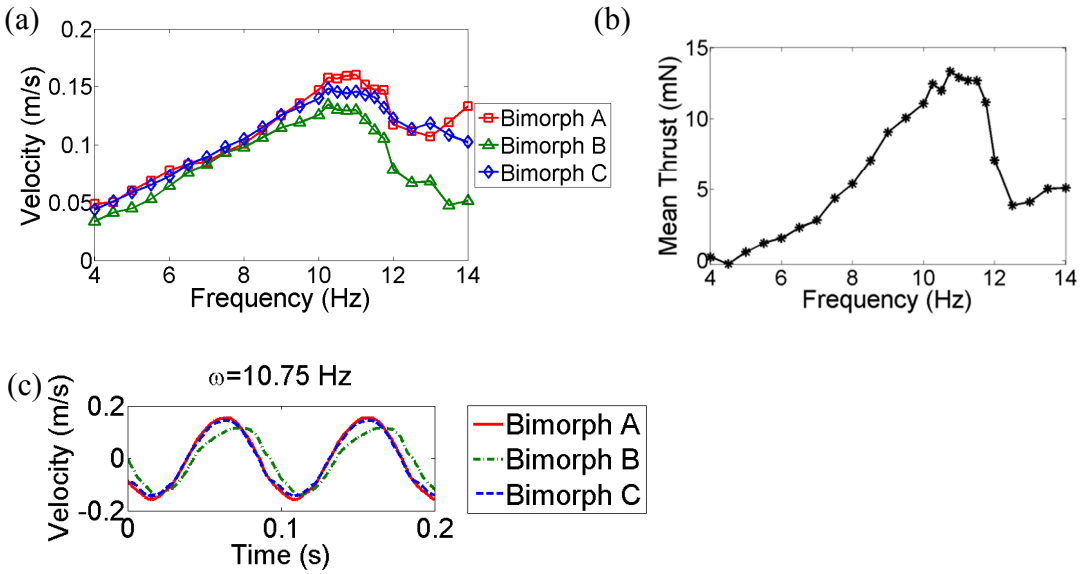

Figure 64. TBPCF dynamics under actuation case 1: (a) velocity frequency response of bimorphs A, B, and C; (b) mean thrust frequency response; (c) simultaneous velocity histories at the resonant frequency.

6.5.2 Cases 2-5: “cup” actuation

As mentioned previously, for actuation cases 2 to 5 (Fig. 63b), a cup like shape is to be created for the TBPCF. Therefore, bimorph B is actuated relatively different for each case although the actuation signal of bimorphs A and C remains the same as 800 V peak to peak.

For actuation case 2, bimorph B is actuated by 400 V peak to peak and in-phase with bimorphs A and C. As can be seen in Fig. 65a, velocity response of bimorph B is lower than the side bimorphs since it is actuated with lower voltage amplitude. Mean thrust response is plotted in Fig. 65b. Two modes are observed at the thrust curve; whose natural frequencies are around 6.5 Hz and 11 Hz. Investigating the simultaneous velocity responses of each bimorph at these frequencies (Fig. 65c), it is observed that the first mode has more phase difference between the mid and the side bimorphs than the second mode. Therefore, the first mode creates more cup-like shape and the second mode is related more to the flat shape (as already known from the previous case). Comparing actuation cases 1 and 2 in general, decreasing actuation voltage amplitude of bimorph B increases the phase difference between the mid and the side bimorphs.

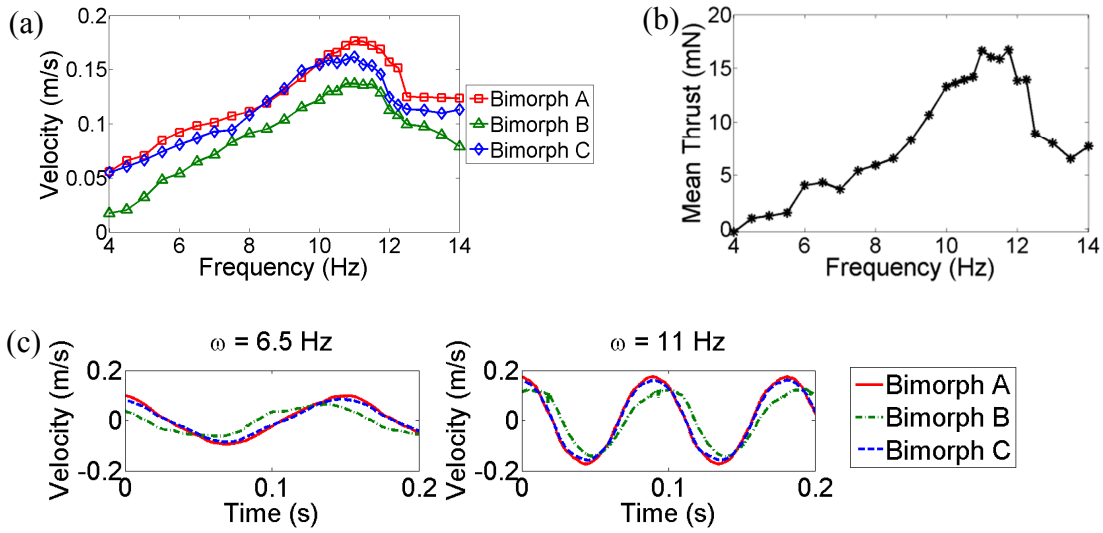

Figure 65. TBPCF dynamics under actuation case 2: (a) velocity frequency response of bimorphs A, B, and C; (b) mean thrust frequency response; (c) simultaneous velocity histories at the resonant frequencies.

Bimorph B is not actuated for the third actuation case. Velocity and mean thrust frequency response graphs related to actuation case 3 are given in Figs. 66a and 66b, respectively. Comparing case 3 with case 2, velocity response of bimorph B has more amplitude difference relative to the side bimorphs (see Fig. 66a). In addition, it is observed in Fig. 66b that the first mode is pronounced more whereas the second mode is suppressed which is expected because the first mode is tried to be promoted by increasing the relative difference of the actuation voltage. Simultaneous velocity response graphs corresponding to both modes are given in Fig. 66c which reveals that the phase difference between the mid and the side bimorphs is higher for case 3 as compared to the previous cases.

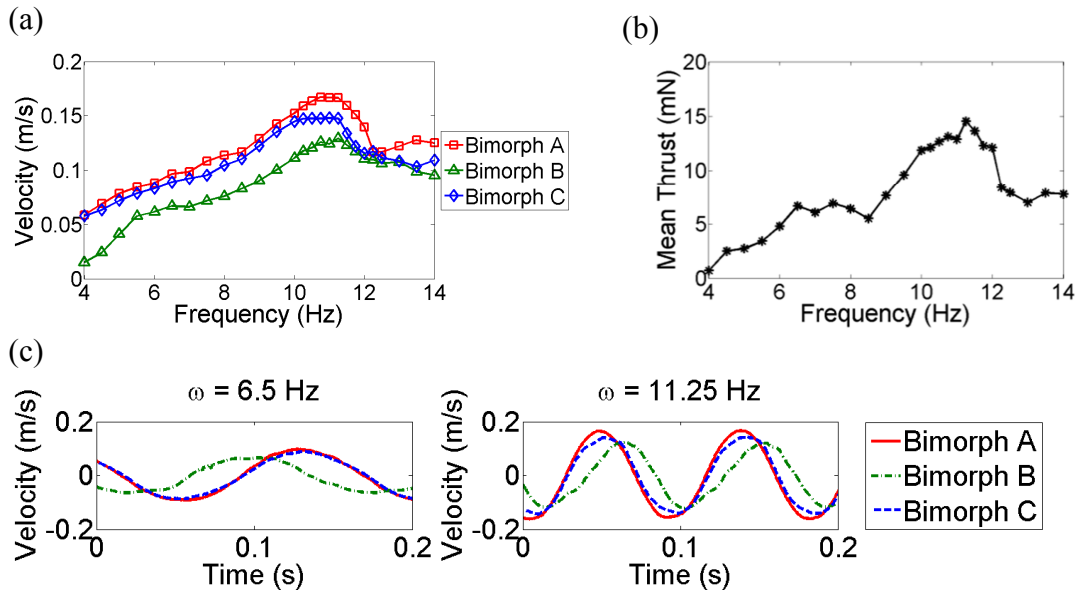

Figure 66. TBPCF dynamics under actuation case 3: (a) velocity frequency response of bimorphs A, B, and C; (b) mean thrust frequency response; (c) simultaneous velocity histories at the resonant frequencies.

Figures 67a and 67b are the velocity and thrust results of actuation case 4, at which bimorph B is actuated with 400 V peak to peak and 180° out of phase to bimorphs A and C. Since the relative difference of actuation between the mid bimorph and the side bimorphs is increased, the first mode is pronounced more, whereas the second mode is weakened comparing to the previous cases of actuation. Although bimorph B is still actuated by lower voltage amplitude, its response is higher than the side bimorphs at the first mode (Fig. 67a). In addition, applying a phase difference to the actuation signals results in a higher phase difference between the velocity responses of the mid and the side bimorphs comparing to the previous cases of actuation (Fig. 67c).

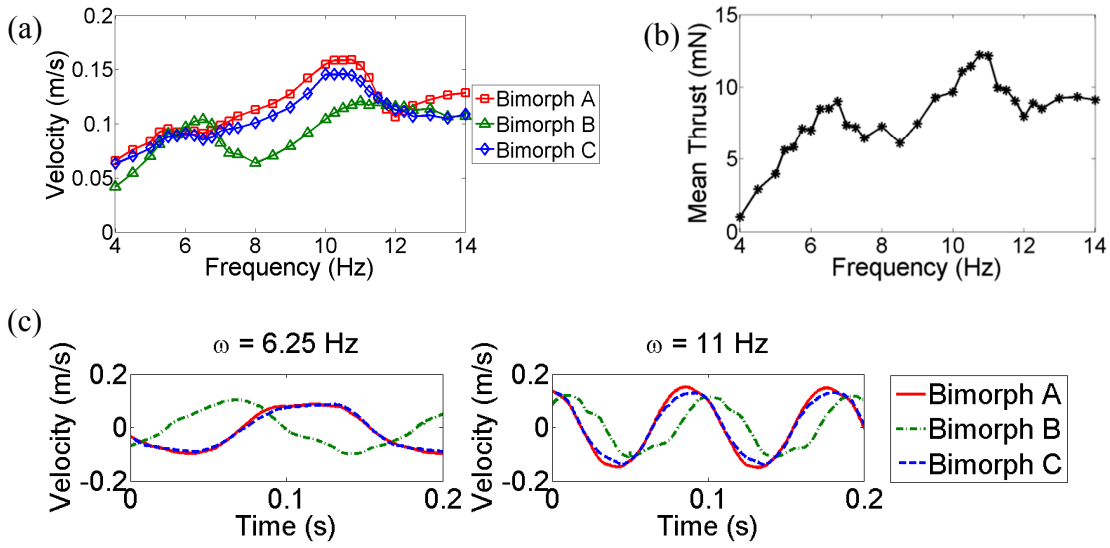

Figure 67. TBPCF dynamics under actuation case 4: (a) velocity frequency response of bimorphs A, B, and C; (b) mean thrust frequency response; (c) simultaneous velocity histories at the resonant frequencies.

Actuation case 5 includes the most relative difference of actuation between the mid bimorph and the side bimorphs, such that bimorph B is actuated with peak-to-peak 800 V with a 180° phase difference. As expected, actuation case 5 has the most pronounced first mode and the most submissive second mode (Figs. 68a and 68b) comparing to the previous cases of actuation; and, the actuation case 5 results in the highest phase difference between the mid bimorph and the side bimorphs for both modes (Fig. 68c).

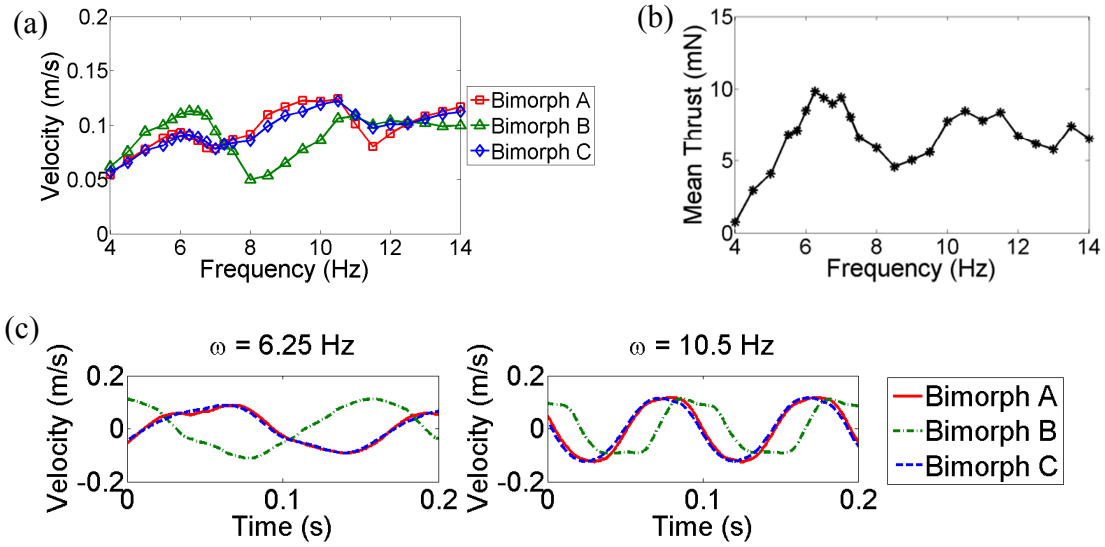

Figure 68. TBPCF dynamics under actuation case 5: (a) velocity frequency response of bimorphs A, B, and C; (b) mean thrust frequency response; (c) simultaneous velocity histories at the resonant frequencies.

6.5.3 Case 6: "rolling" actuation

The last case of actuation, case 6 is called "rolling" at which bimorph B and bimorph C are actuated with peak-to-peak 400 V and 800 V, respectively. There is no phase difference between the actuation signals, and bimorph A is not given any input. As can be seen in Fig. 69a, velocity responses of bimorph B and bimorph C are quite proportional to the actuation voltages. Bimorph A has velocity response as well due to the elastic coupling between bimorphs. Figure 69b is the mean thrust resultant graph which does not exhibit a distinct well-defined mode. However the highest thrust is obtained at 7.25 Hz and that is why corresponding simultaneous velocity responses at this frequency are plotted in Fig. 69c. Figure 69c shows that all of the bimorphs have phase differences.

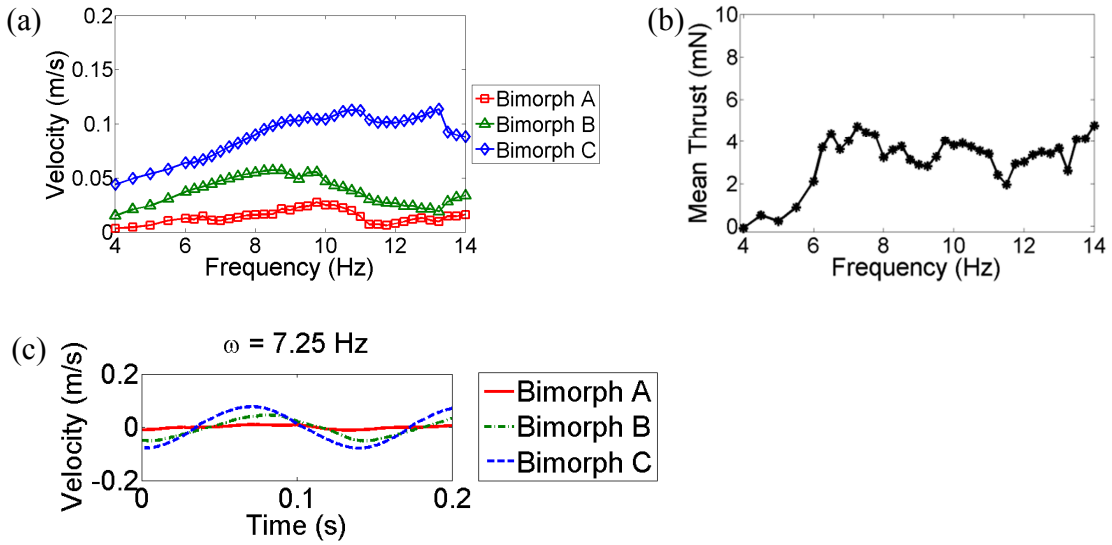

Figure 69. TBPCF dynamics under actuation case 6: (a) velocity frequency response of bimorphs A, B, and C; (b) mean thrust frequency response; (c) simultaneous velocity histories at the resonant frequencies.

6.5.4 Tabulated velocity and phase results

Table 5 lists the numerical values of the velocity and phase responses at the resonant frequencies of the first and second modes observed during each of the actuation cases. Note that the first mode is not observed in case 1, therefore Table 5 does not include any data for that. In addition only the first mode is investigated for case 6 since it gives the highest thrust. Phase values are calculated based on the simultaneous velocity graphs. Note that phase values are extracted comparing to the zero phase sine wave. In other words, those phase values of the bimorphs are not determined with respect to the input actuation signal. Therefore phase of the response of each bimorph can only be compared among themselves as long as they are simultaneous.

Table 5. Numerical values of the velocity and phase responses at the resonant frequencies of the first and second modes observed during each of the actuation cases

Actuation Cases		First Mode			Second Mode		
		Freq. (Hz)	Vel. (m/s)	Phase (Deg.)	Freq. (Hz)	Vel. (m/s)	Phase (Deg.)
Case 1	A				10.75	0.1594	150
	B					0.1295	167
	C					0.1447	149
Case2	A	6.5	0.0980	250	11	0.1764	262
	B		0.0650	208		0.1369	281
	C		0.0865	255		0.1615	264
Case3	A	6.5	0.0966	216	11.25	0.1665	110
	B		0.0670	139		0.1293	167
	C		0.0889	218		0.1475	115
Case4	A	6.25	0.0930	161	11	0.1538	253
	B		0.1021	53		0.1207	319
	C		0.0892	166		0.1391	254
Case5	A	6.25	0.0906	24	10.5	0.1243	194
	B		0.1127	-102		0.1061	268
	C		0.0907	28		0.1224	188
Case 6	A	7.25	0.0122	111			
	B		0.0493	115			
	C		0.0787	92			

6.5.5 Displacement response of the TBPCF

Using the velocity and phase values in Table 5, the lateral displacements of each bimorph are simulated in Fig. 70 for every case and modes aforementioned. Since displacement is the integral of the velocity, each velocity values are divided by the corresponding frequency so that displacement in amplitude of each bimorph is found. For finding the simultaneous displacements of each bimorph, phase values are taken into account. Keeping bimorph A as reference, phase differences are calculated for each bimorph, and the cosine of these phase differences are multiplied with the corresponding displacement values resulting in the simultaneous displacements of each bimorph.

As can be seen in Fig. 70, cup-like shape at the TBPCF becomes more dominant as the actuation cases changes from 1 to 5, which corresponds to increasing relative difference of actuation signal between the mid and the side bimorphs. Case 6 is a different actuation case which incorporates both twist and bending modes that can clearly be seen in Fig. 70.

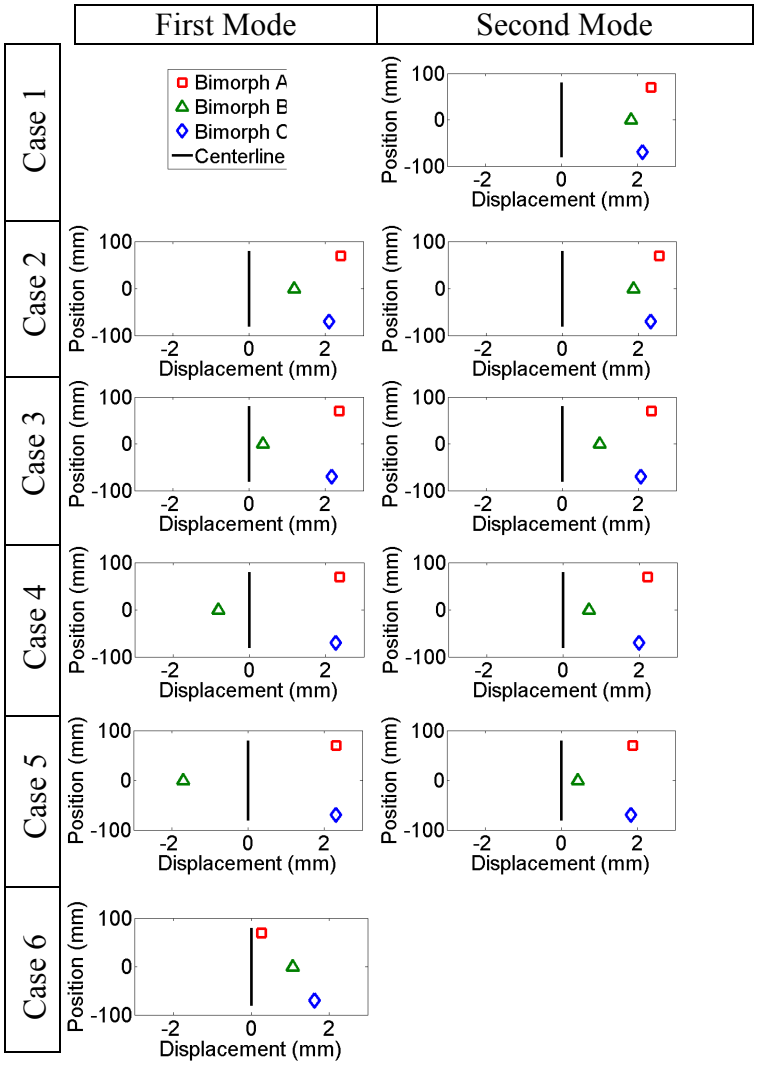

Figure 70. Measured simultaneous displacements of points A, B, and C in different actuation cases.

6.6 Thrust generation and power consumption

6.6.1 Power consumption frequency response curves

Power consumption levels of the TBPCF under the aforementioned actuation cases are given in Fig. 71. Power consumption is directly proportional to the amount of the actuation voltage, and it makes local peaks around the resonant frequencies of the dynamic modes. Therefore actuation cases 1 and 5, and cases 2 and 4 exhibit similar power consumption levels. Phase difference only affects in terms promoting different modes resulting in increased power consumption around different modes. Actuation case 6 is the least power consuming case, yielding also the lowest thrust output.

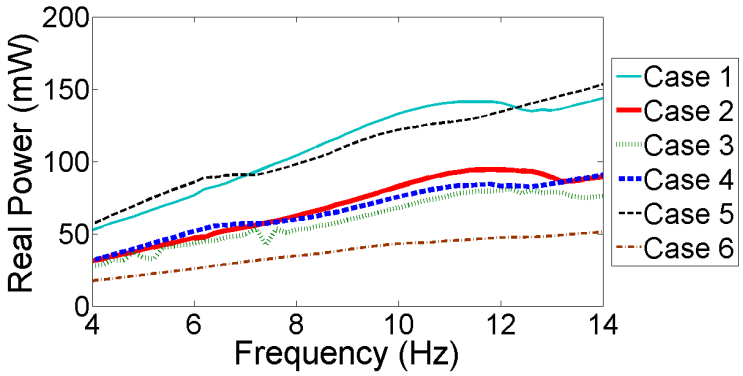

Figure 71. Comparison of real power consumption by TBPCF for different actuation cases.

6.6.2 Mean thrust frequency response curves and thrust comparison

Figure 72 compares the mean thrust results of the actuation cases. In general, thrust is increased for the first mode as the relative difference between the actuation signals of the mid and side bimorphs is increased. Excluding case 1, thrust is higher at the second mode for the cases whose actuation levels of each bimorph are more similar. Although case 1 is the actuation of all bimorphs with the same input, it ranks as the third

highest trust producer at the second mode. Pronounced cup motion results in evolution of the thrust frequency response curves due to formation of the first mode, yielding broadband thrust generation behavior.

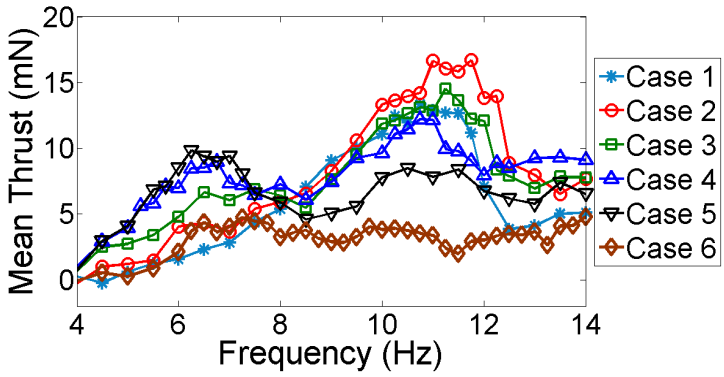

Figure 72. Comparison of mean thrust generated by TBPCF for different actuation cases.

Figure 73 displays an effort to compare the performance of the actuation cases by plotting the mean thrust divided by power consumption. Although thrust results for case 6 is very low, it still performs well at the first mode since its power consumption is lower as well. Considering both power consumption and thrust production characteristics, actuation case 4 is the best choice for the first mode; and for the second mode, case 3 is the most favorable actuation case according to Fig. 73. Note that, an accurate efficiency comparison would require the unconstrained swimming velocity as well, which is not studied in this thesis and suggested for future work.

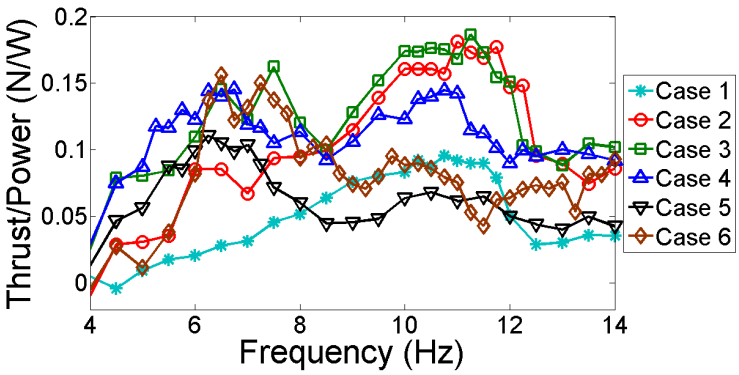

Figure 73. Comparison of mean thrust output per power input of TBPCF for different actuation cases.

CHAPTER 7

POWER CONSUMPTION LEVELS AND ENERGY HARVESTING EXPERIMENTS

7.1 Power consumption in combined dynamic actuation

The average power required for actuation is calculated for the combined actuation cases of the asymmetric bimorph, double bimorph with solar film substrate (DB-SFS), and double bimorph with flexible rubber substrate (DB-FRS). Combined actuation is considered for power consumption calculations since it yields both bending and twisting capabilities, which is a preferred scenario in flapping-wing applications. The current consumption frequency response curves for the combined actuation cases were given in Figs. 29, 47, and 56. The power consumption levels are calculated for the bending mode (BM) and twist mode (TM) resonant frequencies separately. In order to find average power requirement for actuation, the root-mean-square values of the current and voltage input are considered. The average power is given by $P_{\text{ave}} = V_{\text{rms}} I_{\text{rms}} = VI/2$ (where V and I are the voltage input and current consumption amplitudes, respectively).

These average power consumption values are then normalized with respect to the area of active region, where all piezoelectric fibers are located. The active region of the asymmetric bimorph is 8778 mm^2 whereas the active region areas for the DB-SFS and DB-FRS are 4144 mm^2 and 1085 mm^2 respectively. Normalized average power consumption levels in combined actuation case at the BM and TM resonance are plotted in Figs. 74a and 74b respectively. Previously it was observed that current consumption is directly related to the frequency of actuation. Therefore power consumption is related to

the frequency of actuation as well. The difference between the normalized average power consumption levels of the composite architectures depends on the difference between the resonant frequencies of the vibration modes. For instance, DB-SFS has the highest BM resonant frequency, and it has the highest power consumption level in Fig. 74a. Similarly, for the twist mode (Fig 74b), asymmetric bimorph has the highest power consumption level because it has the highest TM resonant frequency.

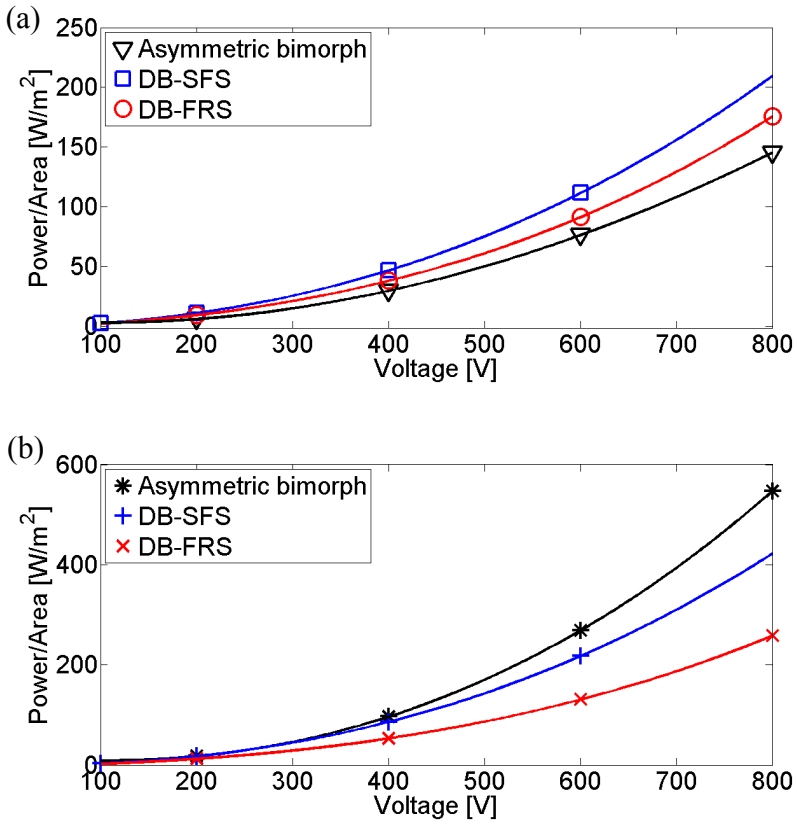

Figure 74. Average power consumption levels per active area of the composite architectures in combined actuation case at (a) bending mode resonant frequencies and (b) twist mode resonant frequencies (Solid lines are curve fit).

7.2 Energy harvesting from ambient vibrations

Piezoelectric composites can also be used to harvest ambient vibration energy by exploiting the direct piezoelectric effect. To determine the energy harvesting capabilities, a series of tests are done on the asymmetric bimorph, DB-SFS, and DB-FRS. Energy harvesting tests are performed by using electromagnetic shaker, resistor box, and accelerometer (Fig. 75), which is a typical setup used in energy harvesting characterization [21]. External load is applied by varying the resistance from short to open circuit conditions in the resistor box. The electromagnetic shaker is employed in order to create base acceleration, which is measured by the accelerometer attached to the clamp connecting the piezo-composite architecture to the armature of the shaker.

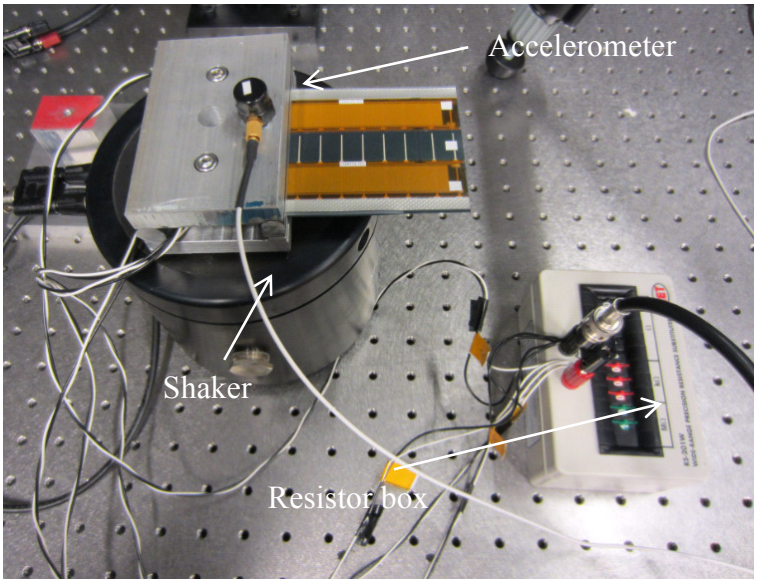

Figure 75. Experimental setup for characterizing the energy harvesting performance of the piezo-composite architectures.

For both of the double bimorphs, the top two MFCs are combined in phase and they are connected to the bottom two MFCs out of phase and in parallel. Basically this wiring corresponds to the pure bending case in the actuation experiments. Similar wiring is applied to the asymmetric bimorph such that 0° laminate is connected out of phase to the 45° laminate. Chirp excitation is used in the experiments covering the fundamental vibration mode. Voltage produced by the asymmetric bimorph and both of the double bimorph architectures due to the base excitation is plotted in Fig. 76 in terms of the voltage – to – base acceleration FRFs (where *g* stands for the gravitational acceleration). The voltage output increases with increased external load as an expected trend [21].

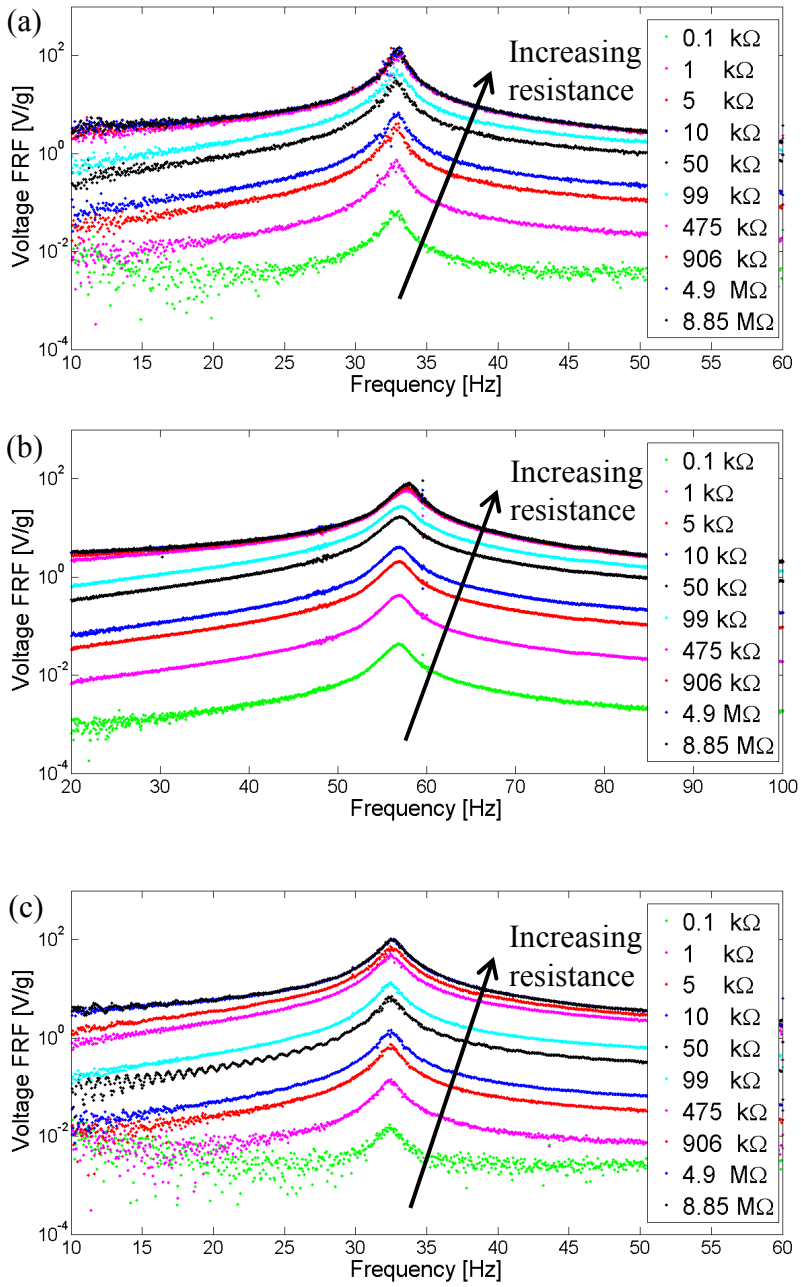

Figure 76. Voltage – to – base acceleration FRFs of the (a) asymmetric bimorph (b) DB-SFS (c) DB-FRS for different levels of external load resistance ranging from short to open circuit conditions.

The input-normalized harvested power can be extracted from the data in Fig. 76 since the power output is related to the voltage produced and electrical resistance. For

resonant excitation, the variation of power output (per base acceleration input) versus load resistance is shown in Fig. 77. It is observed in Fig. 77 that there is an optimum load resistance for every one of the piezo-composite architectures for which the highest amount of power is generated.

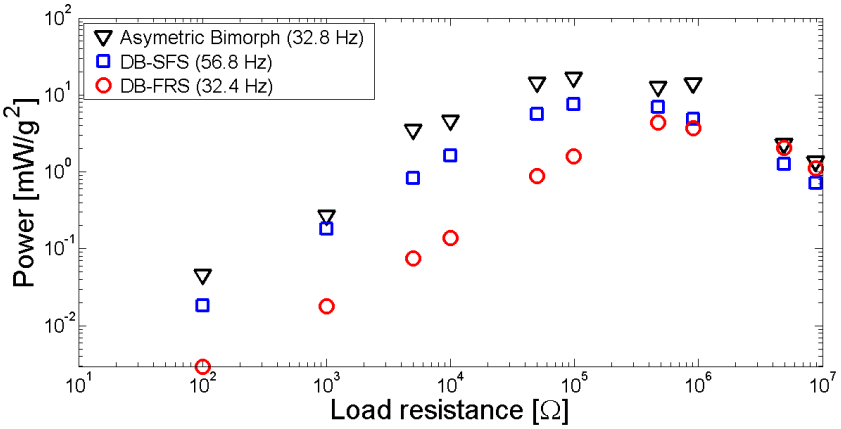

Figure 77. Power outputs (per base acceleration) of the composite architectures versus resistance.

7.3 Solar energy harvesting using flexible solar films

In order to test how much power can be harvested using flexible solar films of similar dimensions to the test samples (such as the substrate material of the double bimorph), three solar films (PowerFilm, Inc.) with the surface areas of 2820 mm^2, 5580 mm^2 and 8760 mm^2 are tested under the realistic irradiance levels of 100 W/m^2, 200 W/m^2, 300 W/m^2, and 400 W/m^2. The experimental setup used in the solar energy harvesting experiments is shown in Fig. 78. In order to change the irradiance level, distance is adjusted between the solar spectrum lamp (6500K Hamilton technology) and the solar film. The irradiance level is measured using an irradiance sensor (SRS-100 solar radiation sensor). The external load resistance (emulated by a resistive decade box)

connected to the electrodes of the solar film is varied from 10 Ω to 1400 Ω. The voltage output (V) is recorded by a multimeter for each resistance (R) value, and the power is calculated from $P = V^2/R$.

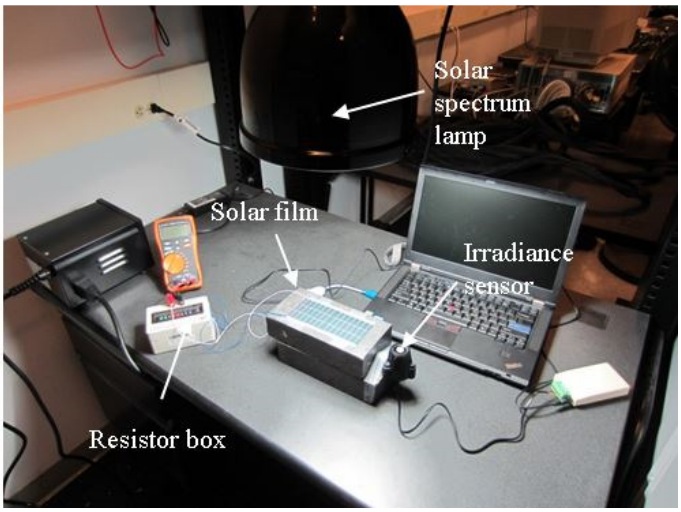

Figure 78. Experimental setup employed for solar energy harvesting measurements using flexible solar films.

For demonstration, the power versus load resistance curves of the 8760 mm^2 area for different irradiance levels are plotted in Fig. 79. For each irradiance level, there exists an optimal load that results in the maximum power output. Furthermore, the optimal electrical load is affected by changing irradiance. With increasing solar irradiance levels, it is observed that the optimal load resistance decreases. Expectedly, the power output increases with increasing solar insolation level.

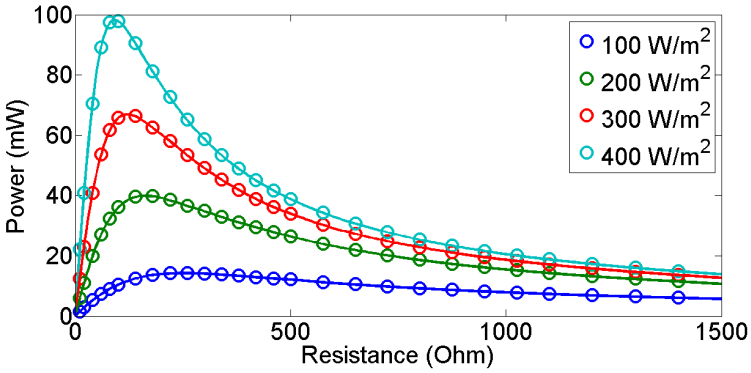

Figure 79. Solar power extracted from 8760 mm^2 solar film area versus resistance for different levels of solar irradiance (solid lines are curve fit).

Having obtained the maximum power output levels for three different solar film areas, the maximum power per solar film area and a curve fit to its mean are plotted versus irradiance level in Fig. 80. In addition to providing the information of the area required for a specific power production level at a given solar irradiance, this graph also provides an idea about the conversion efficiency. Moreover, extrapolation is possible since the power output is directly proportional to the irradiance level.

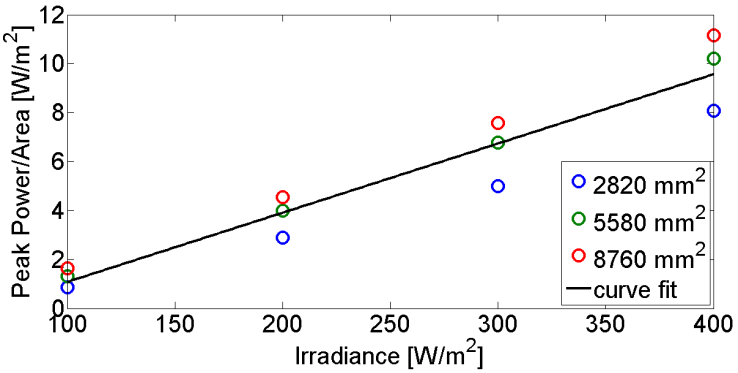

Figure 80. Power per flexible solar film area produced for the optimal resistance value versus solar irradiance.

The set of solar energy harvesting experiments conducted using flexible solar films with dimensions similar to the bimorphs studied in this work show that self-powered wing idea is realistic with a proper storage system. The key comparison of power required and power harvested is made based on the vertical axes in Figs. 74 and 80, respectively. Although the harvested solar power is less than the power consumption of MFCs, structural batteries [69, 70] can be employed for storing the solar energy to use in flapping.

CHAPTER 8

CONCLUSIONS AND RECOMMENDATIONS FOR FUTURE WORK

8.1 Conclusions

This thesis investigates the use of flexible Macro-Fiber Composite (MFC) piezoelectric materials with independent and combined bending-twisting actuation for potential bio-inspired flapping-wing flight and fish-like swimming applications. For flapping-wing flight applications, an asymmetric bimorph (AB) architecture, and two double bimorph architectures, one with a solar film substrate (DB-SFS) and another one with a flexible rubber substrate (DB-FRS), are experimentally characterized covering the fundamental bending and twisting modes. Two degree-of-freedom (DOF) models are applied for the linear region (low voltage actuation) vibratory response for both of the AB and DB configurations. Response under large actuation voltage level is characterized experimentally. Highly nonlinear dynamic behavior is observed under increased voltage actuation. Specifically the piezoelectric softening is pronounced in high voltage actuation of the bending mode whereas strong hardening (yielding the jump phenomenon) is observed in the twisting mode.

The primary focus in this thesis is placed on the structural architectures and concepts for realizing improved bending and twisting actuation authority rather than optimizing or maximizing the numerical performance results. However, numerical performance results in terms of the flapping and twisting angles are also identified. For the asymmetric bimorph, maximum peak-to-peak flapping and twist angles are found to

be 22.8° and 15.7° for the combined actuation case with 800 V peak to peak. Note that MFCs can be actuated up to 2000 V peak to peak without depolarization. For example, DB-SFS is actuated with 1400 V peak to peak in pure bending actuation case resulting in 36.3° flapping angle. Although DB-FRS has the lowest active region area (the least number of piezo-electric fibers), it has highly comparable twisting angle results (14.2° for pure twist actuation at 800 V peak to peak), due to the flexible rubber substrate. The bending-twisting response of DB-FRS is further investigated in the presence of air flow. Wind tunnel tests demonstrated the dynamic bending-twisting coupling (in the sense of classical aeroelastic flutter) with increased air flow speed in the presence of piezoelectric actuation.

Active stiffness change capacity due to static actuation of the double bimorph with the solar film substrate is also investigated. It is observed that approximately 60 % change in the bending stiffness of DB-SFS takes place for the change of DC input voltage from -400 V to 1400 V. Furthermore, energy harvesting from ambient vibration is studied on the two double bimorph architectures and asymmetric bimorph. In optimum external load (resistance) condition, asymmetric bimorph with largest piezoelectric fiber volume produces 16.5 mW/g^2 power using ambient vibrational energy, and it ranks first for energy harvesting capabilities among the three architectures since it has the widest active region. In addition, flexible solar films are investigated as the light-weight multifunctional substructure layers that can create both lift surface and electricity toward the concept of self-powered flapping. For 400 W/m^2 irradiance level, 9.6 W/m^2 amount of energy is harvested by solar panels. The power consumption (in actuation) and power

generation (using flexible solar films) levels are comparable to make the self-powered flapping feasible if an appropriate storage system is employed.

For fish-like swimming applications with complex fin motions, a three degree-of-freedom triple bimorph (TB) biomimetic caudal fin is built and tested for thrust production under different actuation patterns that create flat, cupping and rolling motions at the caudal fin. Six different actuation cases are applied to the TB in order to have flat, cup and rolling shapes at the caudal fin. Evolution of two distinct modes with changing actuation pattern is reported. In the optimum actuation cases, triple bimorph caudal fin produces 9 mN thrust force for a power consumption of 56.4 mW at the first mode, and 16.7 mN thrust force for 94.2 mW power input at the second mode. These thrust values are comparable to biological fish thrust production levels from caudal fin [71]. In addition, a robotic fish that uses the TB as caudal fin has flexibility to choose actuation mode based on the priority between thrust and power consumption.

8.2 Recommendations for future work

8.2.1 Nonlinear electroelastic modeling

This thesis experimentally characterized the electroelastic properties of the bio-inspired piezoelectric architectures both in linear region (low actuation voltage) and nonlinear region (high actuation voltage). A linearized 2-DOF vibration model is successfully applied in the linear region. However, this model is insufficient to predict the response in the nonlinear region because of the softening and hardening nonlinearities as well as the jump phenomenon. In order to clearly demonstrate these nonlinearities, velocity frequency response functions (FRFs) of various actuation cases are shown in

Fig. 81. Softening nonlinearity dominates the first bending mode as can be seen in Fig. 81a which presents the velocity FRFs of the DB-SFS architecture under pure bending actuation case. As stated previously, both softening and hardening nonlinearities and the jump phenomenon are observed for the twist mode of the DB-SFS (Fig 81b). Figure 81c presents the velocity FRFs of asymmetric bimorph under combined actuation case, and similar nonlinearities related to the bending and twisting modes are observed for the combined actuation case as well. Future work should include modeling of electromechanical coupling, geometric, and dissipative nonlinearities, to capture softening and hardening behaviors as well as the jump phenomenon. Specifically the jump phenomenon observed in the twist mode can be exploited for bandwidth and performance enhancement.

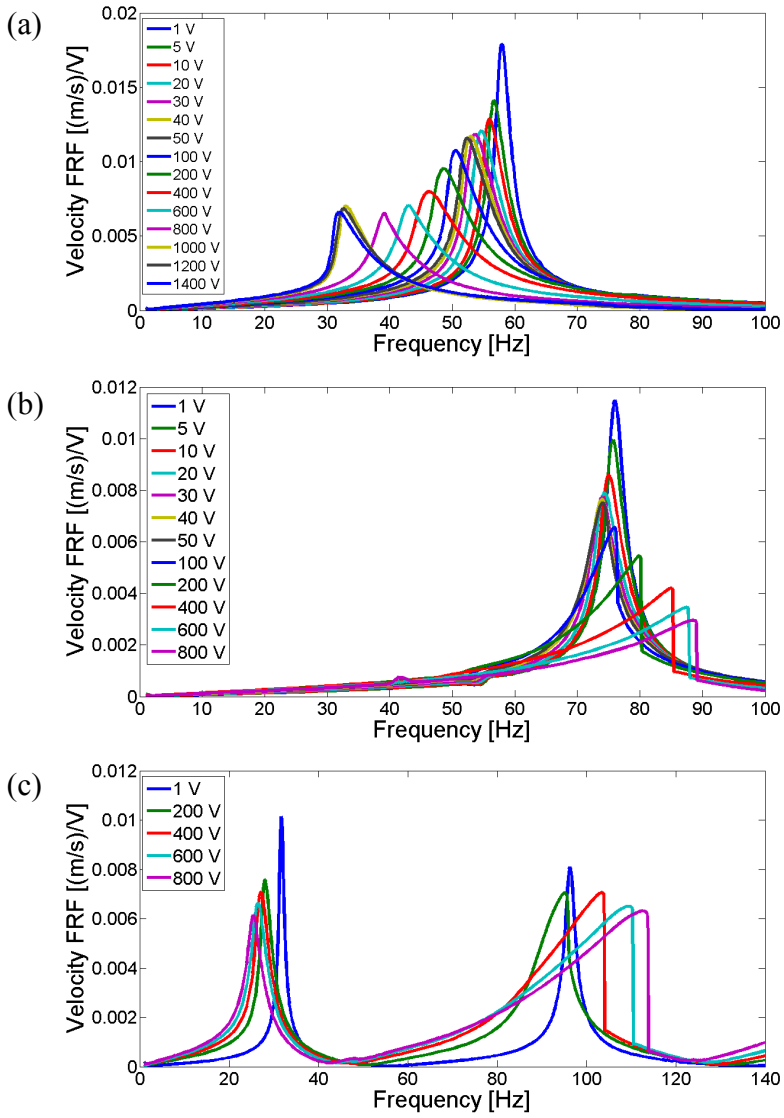

Figure 81. Velocity FRFs per actuation voltage of (a) double bimorph with solar film substrate under pure bending actuation case (at measurement point B), (b) double bimorph with solar film substrate under pure twisting actuation case (at measurement point A), and (c) asymmetric bimorph under combined actuation case (at measurement point A).

8.2.2 Characterization of lift and thrust production for flapping-wing flight

Although fundamental bending-twisting mode characteristics are well determined for different actuation cases, different voltage input levels, and different air flow speeds, characterization of lift and thrust generation is left for future work. Specifically,

asymmetric actuation cases are thought to increase lift and thrust production. For instance, different actuation signals can be applied to the asymmetric bimorph during upstroke and downstroke cycles causing different flapping speeds or mode shapes at each stroke. For the double bimorph architecture, each bimorph can be actuated by different signals which have amplitude, phase, or offset difference. Since the bending and twisting mode resonant frequencies are well-separated, the electroelastic architectures investigated in this thesis have high potential for various asymmetric actuation cases.

8.2.3 Fish prototype to estimate swimming speeds

Thrust generated by the triple bimorph biomimetic caudal fin is measured and compared for different actuation cases. In future, a fish prototype can be built [60], and the locomotion of the prototype can be provided by the triple bimorph biomimetic caudal fin in order to measure the resulting swimming speed. Swimming speeds can be further considered for comparing the efficiency of the actuation cases.

8.2.4 Production of a caudal fin with more fin rays of MFC bimorphs

The biomimetic caudal fin studied in this thesis has three MFC bimorphs and 3-DOF. Therefore, it is able to mimic flat, cupping, and undulation shapes. However, more MFC bimorphs can be employed to have higher DOF and to be able to realize other caudal fin shapes observed in fish which are W and undulation [39]. Additionally, multiple fins can be used for 3-D vectoring of thrust resultant.

REFERENCES

1. Uchino, K., *Piezoelectric actuators 2006 - Expansion from IT/robotics to ecological/energy applications.* Journal of Electroceramics, 2008. **20**(3-4): p. 301-311.

2. Wilkie, W.K., et al., *Low-cost piezocomposite actuator for structural control applications.* Smart Structures and Material 2000: Industrial and Commercial Applications of Smart Structures Technologies, 2000. **3991**: p. 323-334.

3. Bryant, R.G., *Overview of NASA Langley's Piezoelectric Ceramic Packaging Technology and Applications*, 2007, National Aeronautics and Space Administration, Langley Research Center.

4. Sodano, H.A., G. Park, and D.J. Inman, *An investigation into the performance of macro-fiber composites for sensing and structural vibration applications.* Mechanical Systems and Signal Processing, 2004. **18**(3): p. 683-697.

5. Matt, H.M. and F.L. di Scalea, *Macro-fiber composite piezoelectric rosettes for acoustic source location in complex structures.* Smart Materials & Structures, 2007. **16**(4): p. 1489-1499.

6. Yang, Y.W., L.H. Tang, and H.Y. Li, *Vibration energy harvesting using macro-fiber composites.* Smart Materials & Structures, 2009. **18**(11).

7. Mudupu, V., et al., *Design and validation of a fuzzy logic controller for a smart projectile fin with a piezoelectric macro-fiber composite bimorph actuator.* Smart Materials & Structures, 2008. **17**(3).

8. Kovalovs, A., E. Barkanov, and S. Gluhihs, *Active twist of model rotor blades with D-spar design.* Transport, 2007. **22**(1): p. 38-44.

9. Browning, J.S., *F-16 Ventral Fin Buffet Alleviation Using Piezoelectric Actuators*, 2009, DTIC Document.

10. Gomez, J.C. and E. Garcia, *Morphing unmanned aerial vehicles.* Smart Materials and Structures, 2011. **20**: p. 103001.

11. Shyy, W., M. Berg, and D. Ljungqvist, *Flapping and flexible wings for biological and micro air vehicles.* Progress in Aerospace Sciences, 1999. **35**(5): p. 455-505.

12. Kim, D.K. and J.H. Han, *Smart flapping wing using macro-fiber composite actuators - art. no. 61730F.* Smart Structures and Materials 2006: Smart Structures and Integrated Systems, 2006. **6173**: p. F1730-F1730.

13. Kim, D.K., J.H. Han, and K.J. Kwon, *Wind tunnel tests for a flapping wing model with a changeable camber using macro-fiber composite actuators.* Smart Materials & Structures, 2009. **18**(2).

14. Vos, R., et al., *Post-buckled precompressed elements: a new class of control actuators for morphing wing UAVs.* Smart Materials & Structures, 2007. **16**(3): p. 919-926.

15. Paradies, R. and P. Ciresa, *Active wing design with integrated flight control using piezoelectric macro fiber composites.* Smart Materials & Structures, 2009. **18**(3): p. 035010.

16. Bilgen, O., et al., *Macro-Fiber Composite actuated simply supported thin airfoils.* Smart Materials & Structures, 2010. **19**(5).

17. Ha, K.S., et al., *Development of an active wing for flight machines using macro fiber composites.* IEEE ICMA 2006: Proceeding of the 2006 IEEE International Conference on Mechatronics and Automation, Vols 1-3, Proceedings, 2006: p. 261-266.

18. Ming, A.G., et al., *Development of an Active Flapping Wing using Piezoelectric Fiber Composites.* 2008 Ieee International Conference on Robotics and Biomimetics, Vols 1-4, 2009: p. 2144-2149.

19. Minagawa, K., et al., *Development of Flapping Robots using Piezoelectric Fiber Composites - Performance Enhancement by Unique Structure and Drive Control.* Ieee/Rsj 2010 International Conference on Intelligent Robots and Systems (Iros 2010), 2010: p. 1624-1629.

20. Di Lillo, L., Carnelli, D., Bergamini, A., and Ermanni, P., *Multilayered structures for electro bonded laminates*, in *ASME 2011 Conference on Smart Materials, Adaptive Structures and Intelligent Systems*: Scottsdale, AZ, USA.

21. Erturk, A. and D.J. Inman, *Piezoelectric energy harvesting.* 2011, Chichester: Wiley.

22. Cook-Chennault, K.A., N. Thambi, and A.M. Sastry, *Powering MEMS portable devices - a review of non-regenerative and regenerative power supply systems with special emphasis on piezoelectric energy harvesting systems.* Smart Materials & Structures, 2008. **17**(4).

23. Anton, S.R. and H.A. Sodano, *A review of power harvesting using piezoelectric materials (2003-2006).* Smart Materials & Structures, 2007. **16**(3): p. R1-R21.

24. Bandyopadhyay, P.R., *Trends in biorobotic autonomous undersea vehicles.* Oceanic Engineering, IEEE Journal of, 2005. **30**(1): p. 109-139.

25. Roper, D., et al., *A review of developments towards biologically inspired propulsion systems for autonomous underwater vehicles.* Proceedings of the Institution of Mechanical Engineers, Part M: Journal of Engineering for the Maritime Environment, 2011. **225**(2): p. 77-96.

26. Chu, W.S., et al., *Review of biomimetic underwater robots using smart actuators.* International Journal of Precision Engineering and Manufacturing, 2012. **13**(7): p. 1281-1292.

27. Wen, L., et al., *Quantitative Thrust Efficiency of a Self-Propulsive Robotic Fish: Experimental Method and Hydrodynamic Investigation.* IEEE/ASME Transactions on, (Mechatronics): p. 1-12.

28. Liu, J.D., I. Dukes, and H.S. Hu, *Novel mechatronics design for a robotic fish.* 2005 IEEE/RSJ International Conference on Intelligent Robots and Systems, Vols 1-4, 2005: p. 2077-2082.

29. Liu, F.F., K.M. Lee, and C.J. Yang, *Hydrodynamics of an Undulating Fin for a Wave-Like Locomotion System Design.* Ieee-Asme Transactions on Mechatronics, 2012. **17**(3): p. 554-562.

30. Kim, B., et al., *A biomimetic undulatory tadpole robot using ionic polymer-metal composite actuators.* Smart Materials & Structures, 2005. **14**(6): p. 1579-1585.

31. Tan, X.B., et al., *An autonomous robotic fish for mobile sensing.* 2006 IEEE/RSJ International Conference on Intelligent Robots and Systems, Vols 1-12, 2006: p. 5424-5429.

32. Ye, X.F., Y.D. Su, and S.X. Guo, *A centimeter-scale autonomous robotic fish actuated by IPMC actuator.* 2007 Ieee International Conference on Robotics and Biomimetics, Vols 1-5, 2007: p. 262-267.

33. Ye, X.F., et al., *Design and Realization of a Remote Control Centimeter-Scale Robotic Fish.* 2008 Ieee/Asme International Conference on Advanced Intelligent Mechatronics, Vols 1-3, 2008: p. 25-30.

34. Wiguna, T., et al., *Design and Experimental Parameteric Study of a Fish Robot Actuated by Piezoelectric Actuators.* Journal of Intelligent Material Systems and Structures, 2009. **20**(6): p. 751-758.

35. Heo, S., et al., *Effect of an Artificial Caudal Fin on the Performance of a Biomimetic Fish Robot Propelled by Piezoelectric Actuators.* Journal of Bionic Engineering, 2007. **4**(3): p. 151-158.

36. Erturk, A. and G. Delporte, *Underwater thrust and power generation using flexible piezoelectric composites: an experimental investigation toward self-powered swimmer-sensor platforms.* Smart Materials & Structures, 2011. **20**(12).

37. Flammang, B.E. and G.V. Lauder, *Speed-dependent intrinsic caudal fin muscle recruitment during steady swimming in bluegill sunfish, Lepomis macrochirus.* J Exp Biol, 2008. **211**(Pt 4): p. 587-98.

38. Flammang, B.E. and G.V. Lauder, *Caudal fin shape modulation and control during acceleration, braking and backing maneuvers in bluegill sunfish, Lepomis macrochirus.* J Exp Biol, 2009. **212**(Pt 2): p. 277-86.

39. Esposito, C.J., et al., *A robotic fish caudal fin: effects of stiffness and motor program on locomotor performance.* J Exp Biol, 2012. **215**(Pt 1): p. 56-67.

40. Di Lillo, L., et al., *Quasi-static electric properties of insulating polymers at a high voltage for electro-bonded laminates.* Smart Materials and Structures, 2011. **20**(5): p. 057002.

41. Di Lillo, L., et al., *Frequency-dependent dielectric response model for polyimide-poly(vinilydenefluoride) multilayered dielectrics.* Applied Physics Letters, 2012. **101**(1).

42. Raither, W., et al., *Adaptive bending-twist coupling in laminated composite plates by controllable shear stress transfer.* Composites Part a-Applied Science and Manufacturing, 2012. **43**(10): p. 1709-1716.

43. Dickinson, M.H., F.O. Lehmann, and S.P. Sane, *Wing rotation and the aerodynamic basis of insect flight.* Science, 1999. **284**(5422): p. 1954-1960.

44. Sane, S.P. and M.H. Dickinson, *The control of flight force by a flapping wing: Lift and drag production.* Journal of Experimental Biology, 2001. **204**(15): p. 2607-2626.

45. Wood, R.J., *Design, fabrication, and analysis of a 3DOF, 3cm flapping-wing MAV*. 2007 Ieee/Rsj International Conference on Intelligent Robots and Systems, Vols 1-9, 2007: p. 1582-1587.

46. Fukushima, Y., et al., *Development of Flapping Robots using Piezoelectric Fiber Composites - Development of Driving Module Inspired by Insects with Indirect Flight Muscle -.* IEEE/ International Conference on Mechatronics and Automation, 2010: p. 77-82.

47. Tobalske, B.W., et al., *Three-dimensional kinematics of hummingbird flight.* Journal of Experimental Biology, 2007. **210**(13): p. 2368-2382.

48. Crespi, A., et al., *Controlling swimming and crawling in a fish robot using a central pattern generator.* Autonomous Robots, 2008. **25**(1-2): p. 3-13.

49. Zhou, C.L. and K.H. Low, *Design and Locomotion Control of a Biomimetic Underwater Vehicle With Fin Propulsion.* Ieee-Asme Transactions on Mechatronics, 2012. **17**(1): p. 25-35.

50. Aureli, M., V. Kopman, and M. Porfiri, *Free-Locomotion of Underwater Vehicles Actuated by Ionic Polymer Metal Composites.* Ieee-Asme Transactions on Mechatronics, 2010. **15**(4): p. 603-614.

51. Chen, Z., S. Shatara, and X. Tan, *Modeling of biomimetic robotic fish propelled by an ionic polymer–metal composite caudal fin.* Mechatronics, IEEE/ASME Transactions on, 2010. **15**(3): p. 448-459.

52. Mbemmo, E., et al., *Modeling of biomimetic robotic fish propelled by an ionic polymer-metal composite actuator.* 2008 Ieee International Conference on Robotics and Automation, Vols 1-9, 2008: p. 689-694.

53. Takagi, K., et al., *Development of a rajiform swimming robot using ionic polymer artificial muscles.* 2006 IEEE/RSJ International Conference on Intelligent Robots and Systems, Vols 1-12, 2006: p. 1861-1866.

54. Yeom, S.W. and I.K. Oh, *A biomimetic jellyfish robot based on ionic polymer metal composite actuators.* Smart Materials & Structures, 2009. **18**(8).

55. Wang, Z.L., et al., *Embedded SMA wire actuated biomimetic fin: a module for biomimetic underwater propulsion.* Smart Materials & Structures, 2008. **17**(2).

56. Rossi, C., et al., *Bending continuous structures with SMAs: a novel robotic fish design.* . Bioinspiration & Biomimetics, 2011. **6**: p. 045005.

57. Ming, A.G., et al., *Development of Underwater Robots using Piezoelectric Fiber Composite.* Icra: 2009 Ieee International Conference on Robotics and Automation, Vols 1-7, 2009: p. 3435-3440.

58. Nagata, Y., et al., *Development of Underwater Robot using Macro Fiber Composite.* 2008 Ieee/Asme International Conference on Advanced Intelligent Mechatronics, Vols 1-3, 2008: p. 955-960.

59. Shintake, J., A.G. Ming, and M. Shimojo, *Development of Flexible Underwater Robots with Caudal Fin Propulsion.* Ieee/Rsj 2010 International Conference on Intelligent Robots and Systems (Iros 2010), 2010.

60. Cen, L. and A. Erturk, *Bio-inspired aquatic robotics by untethered piezohydroelastic actuation.* Bioinspiration & Biomimetics, 2013. **8**(1): p. 016006.

61. Reddy, J.N., *Mechanics of laminated composite plates : theory and analysis*1997, Boca Raton: CRC Press. 782 p.

62. Jones, R.M., *Mechanics of composite materials*. 2nd ed1999, Philadelphia, PA: Taylor & Francis. xvi, 519 p.

63. Wolf, K. and O. Gottlieb, *Nonlinear dynamics of a noncontacting atomic force microscope cantilever actuated by a piezoelectric layer.* Journal of Applied Physics, 2002. **91**(7): p. 4701-4709.

64. Usher, T. and A. Sim, *Nonlinear dynamics of piezoelectric high displacement actuators in cantilever mode.* Journal of Applied Physics, 2005. **98**(6).

65. Stanton, S.C., et al., *Nonlinear nonconservative behavior and modeling of piezoelectric energy harvesters including proof mass effects.* Journal of Intelligent Material Systems and Structures, 2012. **23**(2): p. 183-199.

66. Nayfeh, A.H. and P.F. Pai, *Linear and nonlinear structural mechanics*. Wiley series in nonlinear science2004, Hoboken, N.J.: Wiley-Interscience. xvii, 746 p.

67. Nayfeh, A.H. and D.T. Mook, *Nonlinear oscillations*. Pure and applied mathematics1979, New York: Wiley. xiv, 704 p.

68. De Marqui, C., A. Erturk, and D.J. Inman, *Piezoaeroelastic Modeling and Analysis of a Generator Wing with Continuous and Segmented Electrodes.* Journal of Intelligent Material Systems and Structures, 2010. **21**(10): p. 983-993.

69. Anton, S.R., A. Erturk, and D.J. Inman, *Multifunctional self-charging structures using piezoceramics and thin-film batteries.* Smart Materials and Structures, 2010. **19**(11).

70. Gambier, P., et al., *Piezoelectric, solar and thermal energy harvesting for hybrid low-power generator systems with thin-film batteries.* Measurement Science & Technology, 2012. **23**(1).

71. Lauder, G.V. and E.G. Drucker, *Forces, fishes, and fluids: hydrodynamic mechanisms of aquatic locomotion.* News Physiol Sci, 2002. **17**: p. 235-40.